

2D AND 3D FINITE ELEMENT ANALYSES OF DYNAMIC DELAMINATION
IN CURVED CFRP LAMINATES

A THESIS SUBMITTED TO
THE GRADUATE SCHOOL OF NATURAL AND APPLIED SCIENCES
OF
MIDDLE EAST TECHNICAL UNIVERSITY

BY

TAMER TAHİR ATA

IN PARTIAL FULFILLMENT OF THE REQUIREMENTS
FOR
THE DEGREE OF MASTER OF SCIENCE
IN
AEROSPACE ENGINEERING

SEPTEMBER 2019

Approval of the thesis:

**2D AND 3D FINITE ELEMENT ANALYSES OF DYNAMIC
DELAMINATION IN CURVED CFRP LAMINATES**

submitted by **TAMER TAHİR ATA** in partial fulfillment of the requirements for the degree of **Master of Science in Aerospace Engineering Department, Middle East Technical University** by,

Prof. Dr. Halil Kalıpçılar
Dean, Graduate School of **Natural and Applied Sciences**

Prof. Dr. İsmail Hakkı Tuncer
Head of Department, **Aerospace Engineering**

Assoc. Prof. Dr. Demirkan Çöker
Supervisor, **Aerospace Engineering, METU**

Examining Committee Members:

Prof. Dr. Altan Kayran
Aerospace Engineering Dept., METU

Assoc. Prof. Dr. Demirkan Çöker
Aerospace Engineering, METU

Prof. Dr. Fevzi Suat Kadioğlu
Mechanical Engineering Dept., METU

Assoc. Prof. Dr. Ercan Gürses
Aerospace Engineering Dept., METU

Assist. Prof. Dr. Touraj Farsadi
Aerospace Engineering Dept., Adana Alparslan Türkeş STU

Date: 10.09.2019

I hereby declare that all information in this document has been obtained and presented in accordance with academic rules and ethical conduct. I also declare that, as required by these rules and conduct, I have fully cited and referenced all material and results that are not original to this work.

Name, Surname: TAMER TAHİR ATA

Signature:

ABSTRACT

2D AND 3D FINITE ELEMENT ANALYSES OF DYNAMIC DELAMINATION IN CURVED CFRP LAMINATES

ATA, TAMER TAHİR
Master of Science, Aerospace Engineering
Supervisor: Assoc. Prof. Dr. Demirkan Çöker

September 2019, 94 pages

Most of the aerospace structures such as spars and ribs contain curved regions in which presence of curved region induces significant tensile stresses in the radial direction in these complex parts. Since composite materials inherently have low mechanical properties in the transverse direction, transverse tensile stresses developed in curved region cause delamination which reduces load carrying capacity of the component and even leads to collapse of the part. In this study, progressive interlaminar damage in curved CFRP composite laminates with two different ply architectures (unidirectional and fabric) are investigated by using ABAQUS/Explicit in conjunction with cohesive zone elements. The simulations are based on the experiments conducted by Tasdemir [1]. 2D and 3D finite element analyses of the considered two specimens (UD and fabric) are performed under moment/axial combined loading. In both 2D and 3D analyses, delamination is found to induce at the center of the curved region which is exactly the maximum radial stress location. 2D and 3D finite element analyses of dynamic delamination in curved composite laminates revealed that the crack propagation speeds inside the laminate varies as edge crack travels faster than center crack. For UD laminate, delamination initiates at the center of the width of the laminate and as the crack passes to arm region it travels in Mode-II dominance at intersonic speeds. For fabric laminate, delamination initiates at the center of the width

of the laminate. It is interesting to observe the delamination onset at center of the width instead of free-edge where the material mismatch exists between different layer orientations. 3D analysis is found to capture effects that are not seen in the 2D analysis. The analysis agrees well with the experimental results in terms of damage initiation location through the thickness direction and load-displacement trend. To the author's knowledge, this is the first study to model the dynamic delamination in curved CFRP laminates using 3D simulations.

Keywords: Delamination, Cohesive Zone Method, Dynamic Fracture, Curved Composites

ÖZ

BÜKÜMLÜ KARBON FİBER TAKVİYELİ PLASTİK LAMİNATLARDAKİ DİNAMİK DELAMİNASYONUN 2B VE 3B SONLU ELEMANLAR ANALİZİ

ATA, TAMER TAHİR

Yüksek Lisans, Havacılık ve Uzay Mühendisliği

Tez Danışmanı: Doç. Dr. Demirkan Çöker

Eylül 2019, 94 sayfa

Spar ve ribler gibi havacılık yapılarının birçoğu bükümlü bölgeler içermektedir. Bu bükümlü bölgelerin varlığından dolayı radyal yönde ciddi gerilmeler ortaya çıkmaktadır. Kompozit malzemeler genetikleri gereği fiber yönüne dik yönde düşük mekanik özellikler gösterdiğinden bükümlü bölgede meydana gelen bu gerilmeler yük taşıma kapasitesini düşürecek delaminasyona ve hatta yapının tamamen parçalanmasına sebep olabilir. Bu çalışmada, bükümlü kompozit yapılarıdaki tabakalar arası ilerleyen hasar, iki farklı serim mimarisi (UD ve kumaş) için yapışkan alan elemanları ile birlikte ABAQUS/Explicit kullanarak incelenmiştir. Yapılan simülasyonlar daha önce Tasdemir [1] tarafından yapılan deneylere dayanmaktadır. Söz konusu iki numune için iki ve üç boyutlu sonlu elemanlar analizi moment/eksenel kombine yüklemesi altında gerçekleştirilmiştir. Hem 2B hem 3B analizlerde, delaminasyonun maksimum radyal gerilmenin maksimum bükümlü bölge merkezinde meydana geldiği gözlemlenmiştir. Bükümlü kompozitlerdeki dinamik delaminasyonun 2B ve 3B sonlu elemanlar analizi, çatlak ilerleme hızının numune içerisinde değiştiğini ve serbest kenardaki çatlağın merkez çatlaktan daha hızlı ilerlediğini göstermiştir. UD laminat için, delaminasyon numune genişliğinin tam ortasında meydana geldikten sonra numunenin kol bölgesine ulaştığı anda Mode-II yükleme

altında intersonik olarak ilerlemiştir. Kumaş laminat için, delaminasyon numune genişliğinin tam ortasında meydana gelir. Delaminasyon başlangıcının, malzeme uyumsuzluğunun farklı katman oryantasyonları arasında maksimum olduğu serbest kenar yerine numune genişliğinin tam ortasında gözlemlenmesi ilgi çekicidir. Üç boyutlu analizlerde iki boyutlu analizlerde gözlemlenemeyen etkiler açık bir şekilde gözlemlenmiştir.Yapılan analizler kalınlık yönündeki hasar başlangıç yeri ve yük-deplasman eğri trendleri açısından deneyler ile uyumlu sonuç göstermektedir.Yazarın bilgisine göre, bu çalışma CFRP laminatlardaki dinamik delaminasyonun 3B simulasyon kullanılarak modellenmesinde ilktir.

Anahtar Kelimeler: Delaminasyon, Yapışkan Alan Metodu, Dinamik Kırılma, Bükümlü Kompozitler

To my family and grandfather Feridun Erdem

ACKNOWLEDGEMENTS

In the first place, I would like to express my sincere appreciation to my supervisor Assoc. Prof. Dr. Demirkan Çöker for his inspiring motivation during this study.

I also would like to thank Prof. Dr. Altan Kayran, Prof. Dr. Fevzi Suat Kadiođlu, Assoc. Prof. Dr. Ercan Gürses and Assist. Prof. Dr. Touraj Farsadi for their precious comments and suggestions in my thesis committee.

I dedicate this thesis to my deceased grandfather Feridun Erdem whom I would like to spent more time. He has brought wonderful fun and bright inspiration into my life during my childhood. I am grateful to my father Hikmet Ata, my mother Işık Ata and my sister Ayça Ata for their endless love, great motivation, patience and vulnerable support throughout my life.

I would like to thank my friends Onur Bozkurt, Ahmet Çevik, Burçin Özen, Can Muyan, Aydın Amireghbali, and Ogün Yavuz from RUZGEM for their friendship and fruitful research partnership. I am especially thankful to my tiny, Burcu Taşdemir, for her infallible love and encouragement to complete this study.

I am thankful to all my other colleagues at Turkish Aerospace Industries (TAI), especially Kerem Üsü, Ebru Sema Koşarođlu Dede, Zühal Gökbulut Adıgüzel and Günhan Bayar for their moral support and understanding over the course of this study. I would like to thank my chief engineer Faruk Nefes and my manager Bekir Ünlüođlu for their understanding and support.

I also would like to thank Turkish Aerospace Industries (TAI) for supporting my academic studies and RUZGEM for giving me the opportunity to use the computational and testing capabilities.

TABLE OF CONTENTS

ABSTRACT	v
ÖZ	vii
ACKNOWLEDGEMENTS	x
TABLE OF CONTENTS	xi
LIST OF TABLES	xiv
LIST OF FIGURES	xv
LIST OF ABBREVIATIONS	xx
LIST OF SYMBOLS	xxi
CHAPTERS	
1. INTRODUCTION	1
2. METHOD	7
2.1. Explicit Dynamics Algorithm.....	7
2.1.1. Quasi-Static Analysis Using Explicit Dynamics	11
2.1.2. Element Selection for Explicit Analyses	11
2.2. Cohesive Zone Method (CZM)	14
2.2.1. Single-Mode Delamination.....	15
2.2.2. Mixed-Mode Delamination	17
2.3. Virtual Crack Closure Method (VCCT).....	19
3. UD LAMINATE.....	21
3.1. Material	21
3.2. Material Tests for Interlaminar Strengths	25

3.2.1. Curved Beam Strength (CBS) Test	26
3.2.2. Short Beam Strength (SBS) Test.....	29
3.3. Geometry and Boundary Conditions.....	32
3.4. Finite Element Modelling	36
3.4.1. 2D FEM.....	36
3.4.2. 3D FEM.....	38
3.5. Results.....	39
3.5.1. 2D FEA Results.....	39
3.5.2. 3D FEA Results.....	47
3.6. Discussion	60
3.7. Conclusions.....	63
4. FABRIC LAMINATE.....	65
4.1. Material	65
4.2. Geometry and Boundary Conditions.....	66
4.3. Finite Element Modelling	68
4.3.1. 2D FEM.....	68
4.3.2. 3D FEM.....	70
4.4. Results.....	71
4.4.1. 2D FEA Results.....	71
4.4.2. 3D FEA Results.....	77
4.5. Discussion	83
4.6. Conclusions.....	87
REFERENCES	89

LIST OF TABLES

TABLES

Table 3.1. Elastic constants of HexPly AS4/8552 UD prepreg.....	21
Table 3.2. Interface properties of HexPly AS4/8552 UD prepreg.	22
Table 3.3. Material wave speeds for AS4/8552 UD prepreg.....	25
Table 3.4. Results of four CBS experiments.	29
Table 3.5. Results of four SBS experiments.....	31
Table 4.1. Material properties of HexPly AS4/8552 5 HS fabric.....	65
Table 4.2. Interface properties of HexPly AS4/8552 5 HS fabric.	66
Table 4.3. Material wave speeds for HexPly AS4/8552 5 HS fabric.	66

LIST OF FIGURES

FIGURES

Figure 1-1. Curve regions in complex shaped sub-components of various structures [2].	1
Figure 2-1. Central difference method scheme.	9
Figure 2-2. Flowchart for ABAQUS / Explicit.	10
Figure 2-3. Bending behavior for a single fully integrated first-order continuum element.	12
Figure 2-4. Bending behavior for a single first-order reduced-integration element.	12
Figure 2-5. Cohesive zone ahead of the crack tip.	14
Figure 2-6. Bilinear cohesive law for Mode-I delamination.	15
Figure 2-7. Bilinear cohesive law for mixed-mode delamination [23].	18
Figure 2-8. VCCT for Mode-I condition [33].	20
Figure 3-1. (a) Intact specimen positioned on 4-point bending test fixture (b) specimen after the experiment.	26
Figure 3-2. Load-displacement curves of four CBS specimens.	27
Figure 3-3. Geometric dimensions and parameters used in the calculation of the CBS [35].	27
Figure 3-4. (a) 3-point bending test configuration [36], (b) specimen positioned on the three-point bending fixture.	29
Figure 3-5. Load-displacement curves of four SBS specimens.	30
Figure 3-6. Interlaminar shear failure (a) identified in the standard ASTM test procedure (b) in the short beam strength test.	31
Figure 3-7. Specimen geometry for the curved unidirectional laminate.	32
Figure 3-8. Schematic of (a) experimental configuration showing how the specimen is located in the fixture and (b) the load transfer to the specimen through the freely rotating pins.	33

Figure 3-9. Finite element idealization of the boundary conditions for (a) 2D finite element model and (b) 3D finite element model.	34
Figure 3-10. Loading profile of smooth step for quasi-static simulation of UD laminate.....	35
Figure 3-11. Top and bottom faces of (a) 2D cohesive element and (b) 3D cohesive element with the defined thickness direction.....	36
Figure 3-12. Magnified view of the mesh at the center-line of the 2D FEM of UD laminate and details of interface modelling.	37
Figure 3-13. 3D FE model details in terms of interface modelling and mesh density.	39
Figure 3-14. Strain and fracture energy history of 2D FEA of curved UD CFRP laminate.....	40
Figure 3-15. Internal and kinetic energy history of 2D FEA of curved UD CFRP laminate.....	41
Figure 3-16. Load-displacement curves for 2D FEA of curved UD CFRP laminate under quasi-static loading and crack locations on load-displacement curve for critical points.....	42
Figure 3-17. Evolution of the opening stress contours in the curved region of UD CFRP laminate before and after delamination onset.	43
Figure 3-18. Normal stresses at the upper arm and shear Mach wave fronts pointed out with red lines.....	43
Figure 3-19. Crack extension and crack tip speed versus time curves for delamination propagating through upper arm of curved UD CFRP laminate.	44
Figure 3-20. Strain energy release rates for Mode-I and Mode-II as a function of crack length along curved UD CFRP laminate.	45
Figure 3-21. The mode-mixity defined by phase angle as a function of crack length.	46
Figure 3-22. Strain and fracture energy history for 3D FEA of curved UD CFRP laminate.....	47

Figure 3-23. Internal and kinetic energy history for 3D FEA of curved UD CFRP laminate.	48
Figure 3-24. Load - displacement curves for 3D FEA of curved UD CFRP laminate under quasi-static loading and crack locations on load-displacement curve for critical points.	49
Figure 3-25. Delamination initiation and propagation path inside the curved UD CFRP laminate.	50
Figure 3-26. Contours of radial stresses at the center and edge sections of the curved UD CFRP laminate before and after center crack initiation.	51
Figure 3-27. Crack propagation in the center section of upper arm region after the initiation of center crack with normal stress lines forming the shear Mach wave front.	52
Figure 3-28. Crack propagation in the edge section of upper arm region after edge crack initiation with normal stress lines forming the shear Mach wave front.	52
Figure 3-29. Center crack extension and tip speeds for the curved UD CFRP laminate.	53
Figure 3-30. Edge crack extension and crack tip speeds for the curved UD CFRP laminate.	54
Figure 3-31. Strain energy release rates (SERR) and phase angles as a function of width at $\Delta t=2 \mu s$	56
Figure 3-32. Strain energy release rates (SERR) and phase angles as a function of width at $\Delta t=7 \mu s$	57
Figure 3-33. Strain energy release rates (SERR) and phase angles as a function of width at $\Delta t=11 \mu s$	58
Figure 3-34. Strain energy release rates (SERR) and phase angles as a function of width at $\Delta t=13 \mu s$	59
Figure 3-35. Load-displacement curves for curved UD CFRP laminate under quasi-static moment-axial combined loading from experiments [1] compared with 2D and 3D FEA simulations.	60

Figure 3-36. Radial stress distribution and stiffness degradation scalar (SDEG) of cohesive elements in the interfaces..... 61

Figure 3-37. Qualitative comparison of experimental and finite element analyses results..... 62

Figure 3-38. Crack tip speed as a function of the crack tip location from the center of the curved region for 2D crack tip, 3D crack tip at the center and at the edge. 62

Figure 4-1. Specimen geometry for the curved fabric CFRP laminate. 67

Figure 4-2. Stacking sequence of the curved fabric laminate..... 67

Figure 4-3. Loading profile of smooth step for quasi-static simulation of curved fabric laminate..... 68

Figure 4-4. Magnified view of the mesh at the center line of the 2D FEM of fabric laminate and details of interface modelling. 69

Figure 4-5. 3D FEM details of fabric laminate in terms of interface modelling and mesh density. 71

Figure 4-6. Strain and fracture energy history for 2D plane strain analysis of curved fabric CFRP laminate. 72

Figure 4-7. Internal and kinetic energy history for 2D plane strain analysis of curved fabric CFRP laminate. 73

Figure 4-8. Load – displacement curve for 2D FEA of curved fabric CFRP laminate. 74

Figure 4-9. Evolution of the opening stress contours in the curved region of fabric CFRP laminate before and after delamination onset. 75

Figure 4-10. Shear Mach waves radiated from the crack tip and reflecting waves behind the crack tip for four time instances for curved fabric CFRP laminate. 76

Figure 4-11. Crack tip speed as a function of time and crack extension for 2D FEA of curved fabric CFRP laminate..... 77

Figure 4-12. Strain and fracture energy history for 3D FEA of curved fabric CFRP laminate..... 78

Figure 4-13. Internal and kinetic energy history for 3D FEA of curved fabric CFRP laminate..... 78

Figure 4-14. Load – displacement curve for 3D FEA of curved fabric CFRP laminate.	79
Figure 4-15. Delamination initiation and propagation path inside the curved fabric CFRP laminate.	80
Figure 4-16. Center crack tip speed as a function of time and crack extension for 3D FEA of curved fabric CFRP laminate.	81
Figure 4-17. Edge crack tip speed as a function of time and crack extension for 3D FEA of curved fabric CFRP laminate.	82
Figure 4-18. Load-displacement curves for curved fabric laminate under quasi-static moment-axial combined loading from experiments [1] compared with 2D and 3D FEA simulations.....	83
Figure 4-19. Crack tip speeds as a function of crack extensions for center, edge and 2D cracks.....	84
Figure 4-20. Radial stresses at the mid-line of center plane and free edge plane compared with the analytical solution.	85
Figure 4-21. Damage variable (SDEG) of the interface elements at mid-line of center plane and free edge plane for 3D FEA of fabric laminate.	86

LIST OF ABBREVIATIONS

ABBREVIATIONS

2D	Two Dimensional
3D	Three Dimensional
5-HS	Five Harness Satin
ALLAE	Artificial Strain Energy
ALLIE	Internal Energy
ALLKE	Kinetic Energy
ALLSE	Stored Strain Energy
ASTM	American Society for Testing and Materials
BL	Bilinear (Cohesive Zone Model)
CFRP	Carbon Fiber Reinforced Plastics
CPU	Central Processing Unit
CPT	Cured Ply Thickness
CZM	Cohesive Zone Method/Model
CBS	Curved Beam Strength
EOCR	End of Curve Region
EOCRC	End of Curve Region for Center Crack
EOCRE	End of Curve Region for Edge Crack
FE	Finite Element
FEA	Finite Element Analyses
FEM	Finite Element Method
FPF	First-Ply Failure
RAM	Random Access Memory
SBS	Short Beam Strength
SDEG	Damage Variable of Cohesive Elements
ILSS	Interlaminar Shear Strength
ILTS	Interlaminar Tensile Strength
UD	Unidirectional Ply
VCCT	Virtual Crack Closure Technique

LIST OF SYMBOLS

SYMBOLS

C_d	Dilatational wave speed
C_R	Rayleigh wave speed
C_S	Shear wave speed
E_{11}, E_{22}, E_{33}	Elastic modulus in material axis
E_r	Modulus of elasticity in radial direction
E_θ	Modulus of elasticity in tangential (hoop) direction
E_{xx}, E_{yy}, E_{zz}	Elastic modulus in problem axis
F	Airy Stress Function
G_{12}, G_{13}, G_{23}	Shear modulus in material axis
$G_{r\theta}$	Radial shear modulus
G_I, G_{II}, G_{III}	Strain Energy Release Rates
K	Penalty Stiffness of Cohesive Elements
l	Arm Length
r_i	Inner Radius
w	Width of the specimen
U_x, U_y, U_z	Translational Degree of Freedoms
R_x, R_y, R_z	Rotational Degree of Freedoms
S_{11}	Tangential Stress
S_{22}	Transverse Stress
S_{33}	Radial Stress
t	Thickness
w	Width
V_c	Critical speed
ρ	Density
$\sigma_{xx}, \sigma_{xy}, \sigma_{xz}$	Normal stress in x-axis, shear stress in y-axis, shear stress in z axis on yz-plane, respectively
$\sigma_{yy}, \sigma_{yx}, \sigma_{yz}$	Normal stress in y-axis, shear stress in x-axis, shear stress in z axis on xz-plane, respectively
$\sigma_{zz}, \sigma_{zx}, \sigma_{zy}$	Normal stress in z-axis, shear stress in y-axis, shear stress in x axis on xy-plane, respectively

CHAPTER 1

INTRODUCTION

Composites are replacing traditional materials in almost all engineering applications by providing design flexibilities in tailoring structures to meet load requirements with less material. Other advantages fostering the usage of composites other than metals and alloys are: high stiffness-to-weight and strength-to-weight ratios, damage tolerance, resistance to corrosion, non-conductivity and low thermal conductivity. With the recent advances in the manufacturing technologies, many complex shaped sub-components of structures are manufactured from composite materials which include curve regions as shown in Figure 1-1.

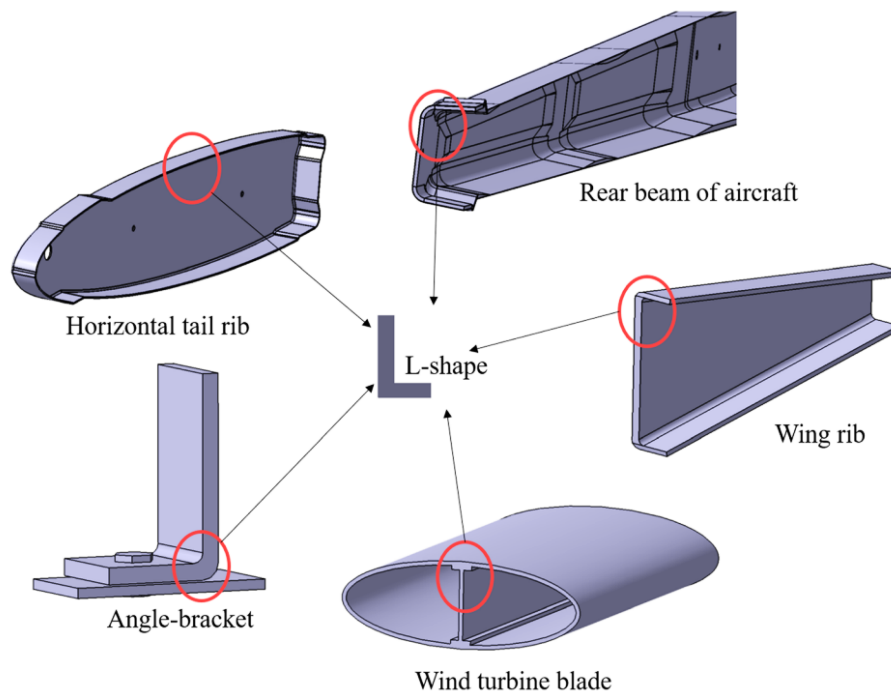


Figure 1-1. Curve regions in complex shaped sub-components of various structures [2].

Presence of curved region induces significant tensile stresses in the radial direction in these complex parts [3]. Since composite materials inherently have low mechanical properties in the transverse direction, transverse tensile stresses developed in curved region cause delamination which reduces load carrying capacity of the component and even leads to collapse of the part. Delamination phenomenon of the highly-curved composite laminates is commonly called unfolding failure, since the bending moment tries to unfold the curved region. The unfolding failure is separated into two kinds considering the initiation mechanism of delamination. The unfolding failure resulting from the tensile radial stresses at the curved region is called traditional unfolding, while the delamination triggered by a matrix crack is called induced unfolding in the literature [4]. While the main reason of the former is the high tensile radial stresses created from the bending of the curved laminate, the latter is emanated from a matrix crack that induces and propagates as a delamination.

In the late 1960s, Lekhnitskii [5] derived the classical elasticity equations to calculate radial (σ_r), tangential (σ_θ) and shear ($\tau_{r\theta}$) stresses in a curvilinear-anisotropic homogeneous beam. The equations are based on the plane stress and small strain assumption. Kedward et al. [3] examined the work done by Lekhnitskii [5] and proposed a rather simplistic formula to calculate maximum radial stress at the curved region. Ko and Jackson [6] developed multilayer theory by considering boundary conditions at each layer interface in Airy stress function to calculate the maximum radial tensile stress and its location for the composite C-coupon. These three studies are the main bases of the analytical calculations performed in our study.

Chang and Springer [7] performed finite element analysis based on plane strain theory to calculate stresses in the curved region of fiber reinforced composite materials. In-plane failure is predicted using the Tsai-Hill criterion whilst out-of-plane failure is predicted by a quadratic stress criterion proposed by the authors.

Sun and Kelly [8] investigated matrix cracking and delamination of composite angle structures through experimentation and finite element analysis. Depending on the

stacking sequence they observed different initial failure modes. Intralaminar failure is predicted by using Tsai-Hill criterion and interlaminar failure is predicted by using maximum radial stress criterion. They concluded that since the out-of-plane stresses are dominant in the curved region, a failure criterion which considers only the two-dimensional stress state is not adequate to predict the critical load. In the light of experimental studies [8], Sun and Kelly [9] incorporated a crack along radial direction into the finite element model and studied the crack branching by employing Virtual Crack Closure Technique (VCCT) introduced by Rybicki and Kanninen [10]. By analyzing the strain energy release rate as a function of crack length, they deduced that the initial delamination growth is unstable.

In the early 1990's, Martin [11] worked experimentally and numerically on unstable delamination of UD curved composite laminates under quasi-static loading. Interlaminar tension failure is predicted by a strength based failure criteria, and VCCT is used to attain all components of strain energy release rate. Examining the calculated strain energy release rates revealed that delamination initiates at the curved region dominantly in Mode-I. The maximum radial stress location is predicted by FEA and elasticity solution. Later, Martin and Jackson [12] carried out experimental, numerical and analytical investigation of the damage prediction in cross-ply curved composite laminates under static and cyclic loading. They used a proper layup, $[0_4/90_3/0_5]_s$, to observe matrix crack induced delamination in the experiments clearly. FEA were performed to determine stress distribution of intact curved region, and VCCT was used to attain strain energy release rate distribution in a model in which matrix crack and delamination present. Comparative study within finite element results (2D Plain strain and 3D model) and closed form solution of Ko and Jackson [6] is performed to obtain radial stress distribution through thickness. The location of maximum radial stress is found at the center-line (center of the width) in 3D analysis which is compared well with the analytical solution. The free edge stresses vary due to the free edge stress singularities. Strain Energy Release Rates (SERRs) at different delamination lengths were compared between 2D and 3D models. The calculated

SERRs at the center line in 3D analysis shows good correlation with the results from 2D model.

In 1996, Wisnom [13] analyzed the anticlastic curvature in pure bending both in 3D model and a 2D model assuming generalised plane strain. He found that as the width increases, the behavior at the center of the 3D model approaches generalised plane strain analysis. Comparison of the results between 3D and 2D models revealed significant variation of stresses along the width of the specimen as a result of the restraint on anticlastic bending due to curvature.

At the beginning of 2000s, initiation and growth of delamination in L-shaped composite laminates are investigated by Wimmer et al. [14]. They used Puck First-Ply Failure criterion in order to predict the interface damage. VCCT is employed for the propagation of the initiated delamination. In load-displacement curve, they observed that the load reduces abruptly due to the change of stiffness when the delamination initiates. Delamination grows in an unstable manner in conjunction with dynamic effects during the load drop. After a significant delamination size, the delamination propagates in a stable manner. Li et al. [15] reported immediate transition to dynamic fracture in static test as the load drops to zero instantaneously.

In a series of recent studies, Gözlüklü et al. [16] - [17] have indicated that delamination of L-shaped composite materials is highly dynamic. They performed explicit FEA in conjunction with cohesive zone elements and experimental simulations under quasi – static loading. The main novelty of their studies was that while the loading is quasi-static, the behavior of the failure is dynamic. An initial crack at the center of the curved region was introduced in their study. In the study conducted in 2012 [16], the considered loading case was P-loading which was parallel to the one of the arms and in the study conducted in 2015 [17] the considered loading case was V-loading which was perpendicular to the one of the arms. Although the initial crack presents in the center of the curve, the mode dominance at the crack tip regions changes with the loading case. For the case of V-loading, the mode dominance at the

curved region on both sides of the crack is uniformly Mode-I. For the case of P-loading, the left crack tip propagates under Mode-I dominance whereas right crack tip propagates under Mode-II dominance. They proposed a “sequential-analysis” method for the computational efficiency in which an explicit analysis followed by an implicit analysis. Moving harmonic radial stress contours (named “radial stress hot spots” in this study) attributed to the elasto-dynamic effects of the crack propagation are observed near the interface. Similar stress contours behind the crack tip were also observed in the studies of Coker et al. [18] - [19]. In another study of Gözlüklü et al. [17], they investigated the dynamic delamination of L-shaped brackets numerically and experimentally. The simulations were performed with using bilinear CZM. The simulations showed that the delamination onset at the curved region is pure Mode-I and the crack tip speeds at that region is sub-Rayleigh. As the crack propagates to the arms, it sustains a speed faster than shear wave speed under pure Mode-II stress field. At the arm regions, shear Mach waves emerging from the crack fronts are observed since the crack tip speed is faster than the material shear wave speed (inter-sonic delamination). Their investigation has provided a significant link between super-shear earthquakes and inter-sonic delamination in L-shaped composite laminates.

In addition to previously mentioned studies on failure of curved composite laminates, a comparison between 2D and 3D modelling of dynamic delamination initiation and propagation is required to gain a better understanding of the failure mechanisms. Modelling of delamination with 3D elements enables to investigate the effects of free-edges in the composite laminates and studying Mode-III fracture effects. In this study, 2D plane strain and full 3D delamination analysis of curved composite laminates are performed and compared in terms of load-displacement response, location of delamination initiation, stress states at the curved region and crack tip speeds. To the author’s knowledge, this study is the first study to model the dynamic delamination in curved CFRP laminates using 3D simulations.

CHAPTER 2

METHOD

Dynamic delamination in curved CFRP laminates is simulated by using explicit dynamics in conjunction with cohesive zone modelling and the virtual crack closure technique. Explicit dynamics algorithm, cohesive zone method, and virtual crack closure technique are elucidated with formulations in this chapter.

2.1. Explicit Dynamics Algorithm

The explicit dynamic integration method, also known as the forward Euler or central difference algorithm [20], calculates the kinematic conditions from the initial kinematic conditions already known from the previous increment at the beginning of each time increment.

The nodal acceleration of each node at the beginning of the current increment (time t) is determined directly as the inverse of the nodal mass matrix times the net nodal force:

$$M\ddot{u}|_{(t)} = (P - I)|_{(t)} \quad (2.1)$$

in which (M) is the lumped mass matrix. (P) and (I) are the external and internal load vectors, respectively.

The governing partial differential equation defined in Eqn. (2.1) is turned into a set of coupled, nonlinear, ordinary differential equations in time by the finite element approximation.

In explicit dynamics, the general form of the equations of motion are defined as follows:

$$\dot{u} = \dot{u}|_{(t=0)} + \int \ddot{u}(t)dt \quad (2.2)$$

$$u = u|_{(t=0)} + \int \dot{u}(t)dt \quad (2.3)$$

ABAQUS/Explicit uses the central difference method to integrate the velocity and displacement field [20], explicitly. Velocity at time $t + \frac{\Delta t}{2}$ can be written in terms of the acceleration at the current time increment and half-step backward velocity:

$$\dot{u}|_{(t_n+\frac{\Delta t}{2})} = \dot{u}|_{(t_n-\frac{\Delta t}{2})} + \ddot{u}|_{(t_n)}\Delta t \quad (2.4)$$

Displacement at time $t + \Delta t$ can be written in terms of the displacement at the current time increment and half-step ahead velocity, since the half-step ahead velocity is already calculated from Eqn. (2.4) and displacement at the current time increment is already known.

$$u|_{(t_n+\Delta t)} = u|_{(t_n)} + \dot{u}|_{(t_n+\frac{\Delta t}{2})}\Delta t \quad (2.5)$$

The displacement-time graph in Figure 2-1 summarizes the central difference integration method. Since velocity is the change of displacement with time, the velocity at time $t_n + \frac{\Delta t}{2}$ can be obtained by dividing the change in displacement between time increments $t_n + \Delta t$ and t_n to the time interval:

$$\dot{u}|_{(t_n+\frac{\Delta t}{2})} = \frac{(u|_{(t_n+\Delta t)} - u|_{(t_n)})}{\Delta t} \quad (2.6)$$

Similarly, acceleration (rate of change of velocity) at time t_n can be calculated from half-step ahead and half-step backward velocities as:

$$\ddot{u}|_{(t_n)} = \frac{\dot{u}|_{(t_n+\frac{\Delta t}{2})} - \dot{u}|_{(t_n-\frac{\Delta t}{2})}}{\Delta t} \quad (2.7)$$

Moreover, the acceleration (rate of change of velocity) at time t_n can be written in terms of displacements at time t_n , $(t_n + \Delta t)$ and $(t_n - \Delta t)$ [22]:

$$\ddot{u}|_{(t_n)} = \frac{1}{\Delta t} \left(\frac{u_{t_n+\Delta t} - u_{t_n}}{\Delta t} - \frac{u_{t_n} - u_{t_n-\Delta t}}{\Delta t} \right) \quad (2.8)$$

Velocity at time $t_n + \frac{\Delta t}{2}$ can be obtained easily from Eqn. (2.7) by the known values of acceleration at time t_n and velocity at time $t_n - \frac{\Delta t}{2}$. Half-step backward velocities are stored through the analysis for such kind of calculations.

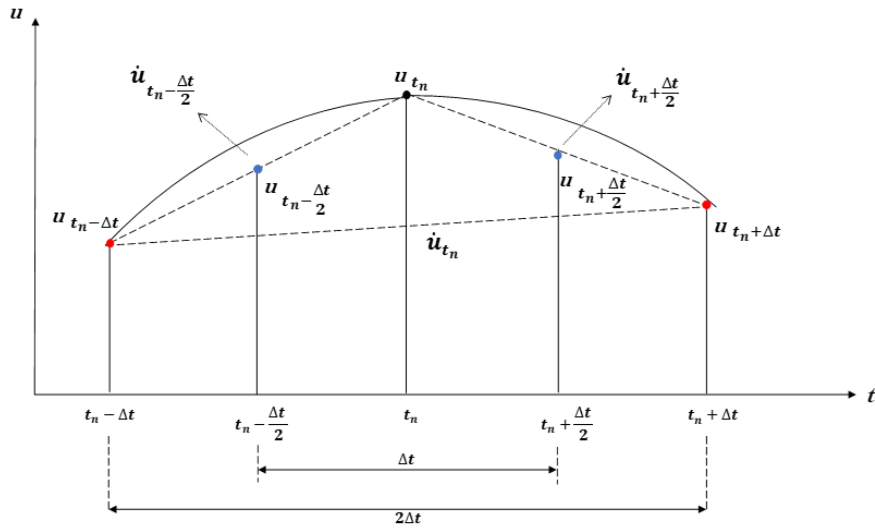


Figure 2-1. Central difference method scheme.

The displacement at time $t_n + \Delta t$ is calculated from Eqn. (2.6) by using the previously calculated half-step ahead velocity and the known displacement value at time t_n . Afterwards, the displacement at time $t_n + \Delta t$ is used to calculate the strain, stress, and internal forces in the element. Then computation of acceleration at time $t_n + \Delta t$ is completed as the inverse of the nodal lumped mass times the net nodal force. Flowchart for explicit time integration is given in Figure 2-2 to summarize the explicit time integration scheme in ABAQUS/Explicit.

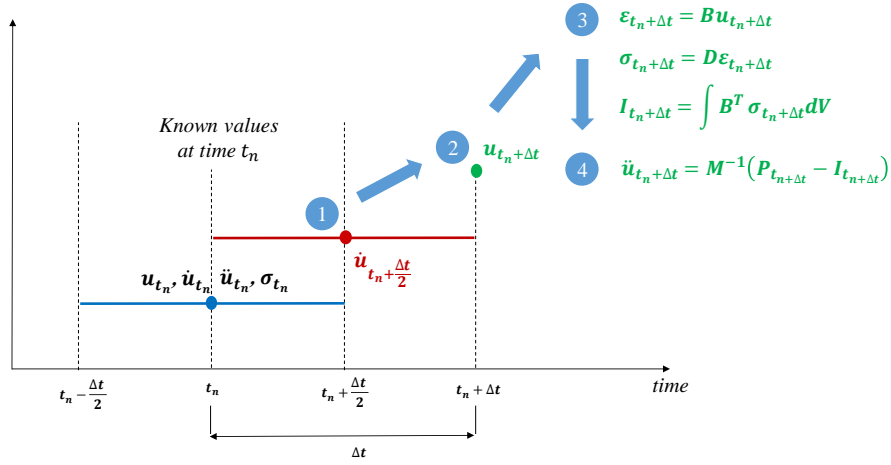


Figure 2-2. Flowchart for ABAQUS / Explicit.

Unlike the total step time, increment size needs not to be specified in ABAQUS/Explicit analyses. The increment size is internally calculated to fulfill the Courant-Friedrichs-Levy (CFL) stability condition and so to obtain accurate results. This condition limits the increment size such that the stress and shock waves in the model cannot travel more than the smallest mesh dimension in a single time step. The limited increment size is called the stable time increment and is calculated by dividing the smallest element length (L_e) in the mesh to the dilatational wave speed of the material (C_d):

$$\Delta t = \frac{L_e}{C_d} \quad (2.9)$$

Stable time increment value (Δt) should be increased to shorten the simulation time. A few ways are listed below for this purpose:

- Increasing element dimensions
- Decreasing material stiffness (will result in a decrease in C_d value)
- Increasing material compressibility (will result in a decrease in C_d value)
- Increasing material density (will result in a decrease in C_d value)

2.1.1. Quasi-Static Analysis Using Explicit Dynamics

Explicit solver is generally preferred for modelling high rate dynamic problems (car crash, explosions, etc.) involving extensive deformations and implicit solver is preferred mostly for static problems. Due to the nature of the implicit solver, it fails to converge in large three-dimensional problems involving contact and material failure. In such simulations, the explicit solver is more efficient and cost-effective compared to the implicit solver. Notwithstanding, modelling the process in its experimental load rate is computationally impractical and would require millions of increments [21].

Mass scaling and increasing the loading rate (which is also used in our study) are the two generally used methods to hasten the analysis when dealing with the quasi-static loading. Since the step time for load introduction should be so large to vanish the inertia effects and so small to obtain reasonable solution time, it is determined by obtaining the first natural frequency of the specimen from eigenvalue analysis. In literature, generally a step time at least ten times the natural frequency of the structure is preferred for quasi-static loading.

Loading is applied by using the below given smooth-step function which provides a gradual increase of load throughout the simulation to minimize the inertial effects;

$$U(t) = U_L \left[10 \left(\frac{t}{t_L} \right)^3 - 15 \left(\frac{t}{t_L} \right)^4 + 6 \left(\frac{t}{t_L} \right)^5 \right] \quad (2.10)$$

in which t_L is the defined step time of explicit simulation and U_L is the maximum prescribed displacement.

2.1.2. Element Selection for Explicit Analyses

Element types defined in ABAQUS/Explicit element library are evaluated for their adequateness to be employed in the analyses considering the numerical problems explained below.

Due to the curved shape and applied load, which tries to unfold the curved region, the dominated behavior around the curve region is bending. Fully integrated first-order

continuum elements (CPS4, CPE4, and C3D8) exhibit unrealistic shear strain when subjected to bending. Hence the energy to bend the element goes into shearing which, results in overly stiff behavior of the element known as shear locking as shown in Figure 2-3.

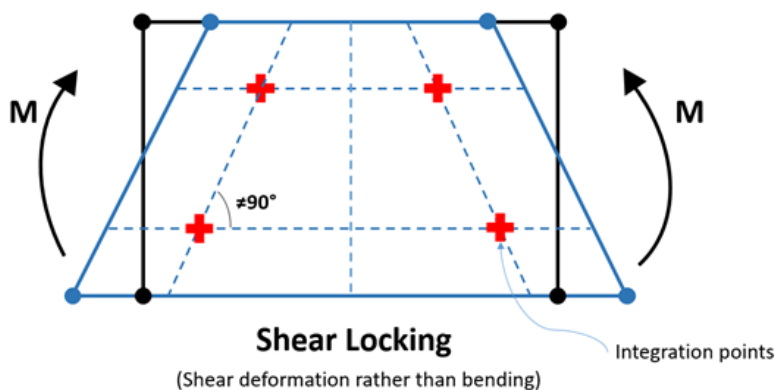


Figure 2-3. Bending behavior for a single fully integrated first-order continuum element.

Using first-order-reduced integration elements (CPS4R, CPE4R, and C3D8R) eliminates shear locking, but these elements suffer from hourglassing. A single element through the thickness does not detect strain in bending which results in zero strain behavior. In this case, element deforms as shown in Figure 2-4 but has no strain values.

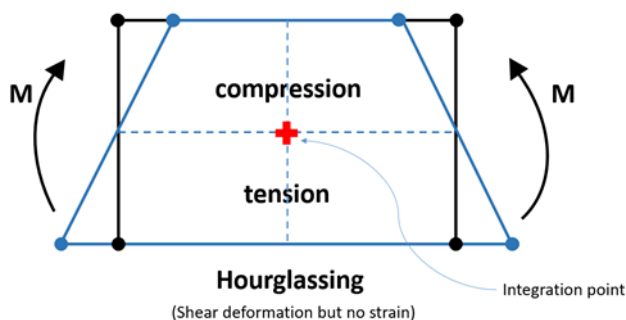


Figure 2-4. Bending behavior for a single first-order reduced-integration element.

In order to prevent unreliable results, multiple reduced integration elements should be used through the thickness (at least four elements). Fully integrated second-order

continuum elements (C3D20) can model bending-dominated problems more accurately [23]. Nevertheless, using second-order elements increases computational cost. Considering the computational efficiency, using reduced integration elements is more preferable. In case of not using multiple elements through the thickness, enhanced hourglass control based on enhanced strain methods should be used in order to prevent hourglassing. However, using enhanced hourglass control adds artificial energy to the system, hence artificial energy should be monitored throughout the analysis. Artificial strain energy (ALLAE) should be 1% of internal energy (ALLIE) which is the recommended threshold for a reliable analysis [21].

Therefore, either reduced-integration or incompatible mode elements should be used. In this study, first-order reduced integration solid elements with enhanced hourglass control are employed in the analysis.

2.2. Cohesive Zone Method (CZM)

Local stress goes to infinity near the crack tip according to the theory of elasticity. The infinite stresses or stress singularities at the crack tip create contradiction in terms of failure mechanisms. Hence in order to avoid stress singularity at the crack tip, there have been many approaches to establish a relationship at the crack tip. One of the most common fracture mechanics approaches is the cohesive zone method (CZM) which is generally used in the simulation of delamination in laminated composite materials.

In the cohesive zone method, a transition zone between elastic and stress-free zones ahead of the crack tip is assumed to exist as shown in Figure 2-5. This transition region is called as cohesive zone, which relates tractions to opening displacements (separations) across the interface.

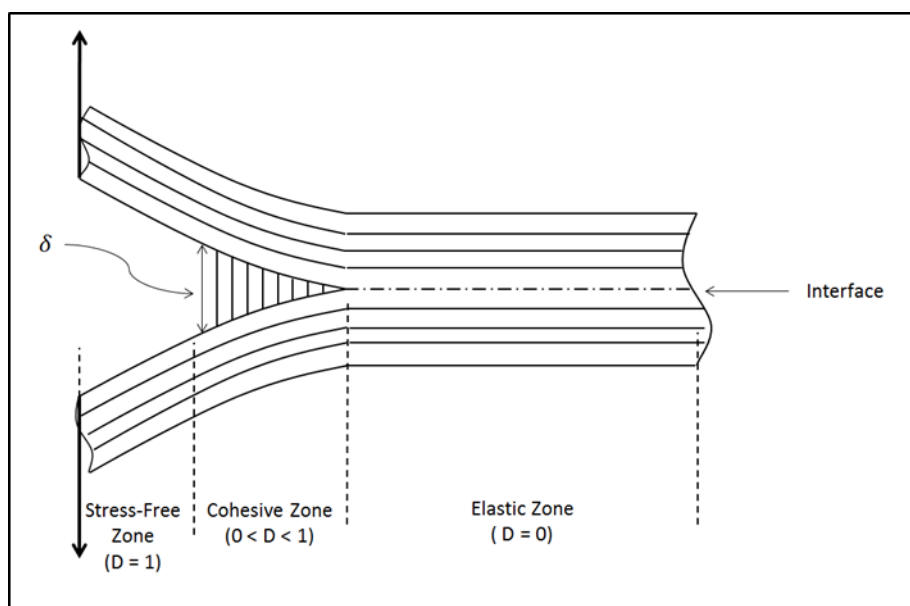


Figure 2-5. Cohesive zone ahead of the crack tip.

The studies of Dugdale [24] and Barrenblatt [25] in the 1960s are the basis of the cohesive zone method. In 1976, Hillerborg et al. [26] came up with a similar model to Barrenblatt's which allows the onset of new cracks and propagation of the current cracks. The concept of CZM was implemented into brittle materials by Needleman [27] in 1999 to simulate intersonic crack growth under shear loading.

In this study, the bilinear cohesive zone model is employed due to its proven success and simplicity in the modelling of delamination. Bilinear cohesive law for single-mode and mixed-mode delamination cases are investigated in detail in the following sub-chapters.

2.2.1. Single-Mode Delamination

Single-mode delamination is investigated by considering only the Mode-I delamination case. Bilinear cohesive law for Mode-I delamination is depicted in Figure 2-6 in terms of tractions (t) and displacements (δ). The required parameters to define bilinear constitutive law for Mode-I fracture are as follows; the elastic modulus or penalty stiffness of the interface (E_0), the interfacial tensile strength (t_I^0), and the Mode-I fracture toughness (G_{IC}).

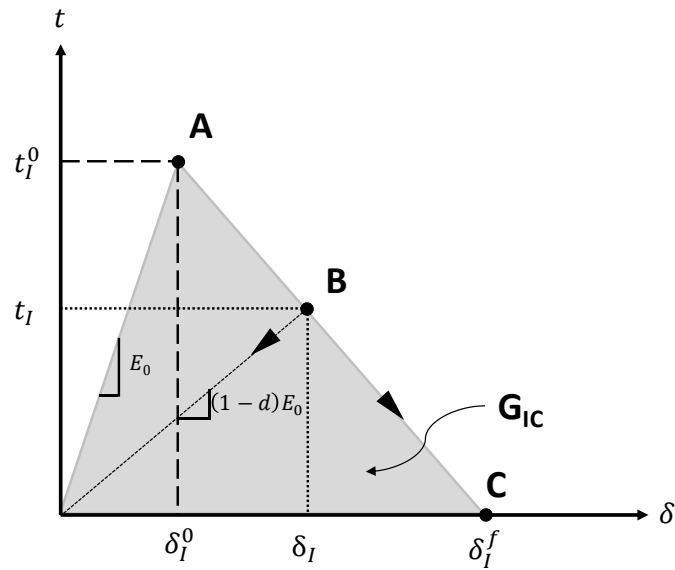


Figure 2-6. Bilinear cohesive law for Mode-I delamination.

The behavior of the material is initially linear elastic until the defined interlaminar tensile strength value (t_I^0) at Point A. The slope of the linearly increasing traction up to the Point A is defined by the elastic modulus or penalty stiffness of the interface (E_0). This penalty stiffness of the interface is determined by using the below-given closed-form expression derived by Turon et al. [28];

$$K = \frac{\alpha E_{33}}{t} \quad (2.11)$$

in which α is a parameter much greater than 1, E_{33} is the elastic modulus of the material in the out-of-plane direction and t is the thickness of an adjacent layer. The parameter α value is selected as 50 since it provides sufficient stiffness for the interface while avoiding convergence problems caused by an excessively stiff interface [28].

When the interlaminar tensile stress reaches the value of t_l^0 , the material degrades progressively by following a linear softening response. A damage variable (D) as a function of displacement at initial failure (δ_l^0), displacement at final failure (δ_l^f), and displacement at an arbitrary point (δ_l) is defined in Eqn. (2.12).

$$D = \frac{\delta_l^f (\delta_l - \delta_l^0)}{\delta_l (\delta_l^f - \delta_l^0)} \quad (2.12)$$

The damage variable (D) is evolved from 0 at the damage initiation point (Point A) to 1 at the final failure point (Point C). The stiffness reduction scheme by using the calculated damage variable (D) is as follows [29];

$$\left. \begin{array}{ll} E_0 \delta & \delta_l < \delta_l^0 \\ (1 - D)E_0 \delta & \delta_l^0 < \delta_l < \delta_l^f \\ 0 & \delta_l \geq \delta_l^f \end{array} \right\} = t_l \quad (2.13)$$

Since the interlaminar tensile strength (t_l^0) and penalty stiffness (E_0) are known, the displacement value at initial failure (δ_l^0) is calculated from Eqn. (2.14).

$$\delta_l^0 = \frac{t_l^0}{E_0} \quad (2.14)$$

The displacement value at the final failure (δ_l^f) is obtained from Eqn. (2.15) by knowing that the area under the traction-separation curve exactly equals the Mode-I fracture toughness of the material.

$$\delta_I^f = \frac{2G_{IC}}{t_I^0} \quad (2.15)$$

For any arbitrary point (such as Point B) on the line A-C, the determination of the damage variable (D) is straightforward by knowing the calculated values of δ_I^f and δ_I^0 .

2.2.2. Mixed-Mode Delamination

In the case of mixed-mode delamination, the interactions between different fracture modes should be considered for both the initiation and propagation of delamination. Therefore, a quadratic stress criterion involving the nominal stress ratios is used in mixed-mode conditions for delamination initiation as defined in Eqn (2.16). Damage initiates when this equation equals to one.

$$f = \left\{ \frac{\langle t_n \rangle}{t_n^0} \right\}^2 + \left\{ \frac{t_s}{t_s^0} \right\}^2 + \left\{ \frac{t_t}{t_t^0} \right\}^2 \quad (2.16)$$

The subscripts n, s, and t are used for each fracture mode as normal, shear, and tearing, respectively. The symbol ($\langle \rangle$) used in the normal stress component refers to the Macaulay bracket and it is defined as follow:

$$\langle t_n \rangle = \frac{(t_n + |t_n|)}{2} \quad (2.17)$$

As can be understood from the Eqn. (2.17), the Macaulay bracket in the first term implies that compressive stresses do not cause damage.

Bilinear cohesive law for mixed-mode delamination is depicted in Figure 2-7. A mixed-mode damage variable (D) as a function of mixed-mode displacement at initial failure (δ_m^0), mixed-mode displacement at final failure (δ_m^f), and mixed-mode displacement at an arbitrary point (δ_m) is defined in Eqn. (2.18).

$$D = \frac{\delta_m^f (\delta_m - \delta_m^0)}{\delta_m (\delta_m^f - \delta_m^0)} \quad (2.18)$$

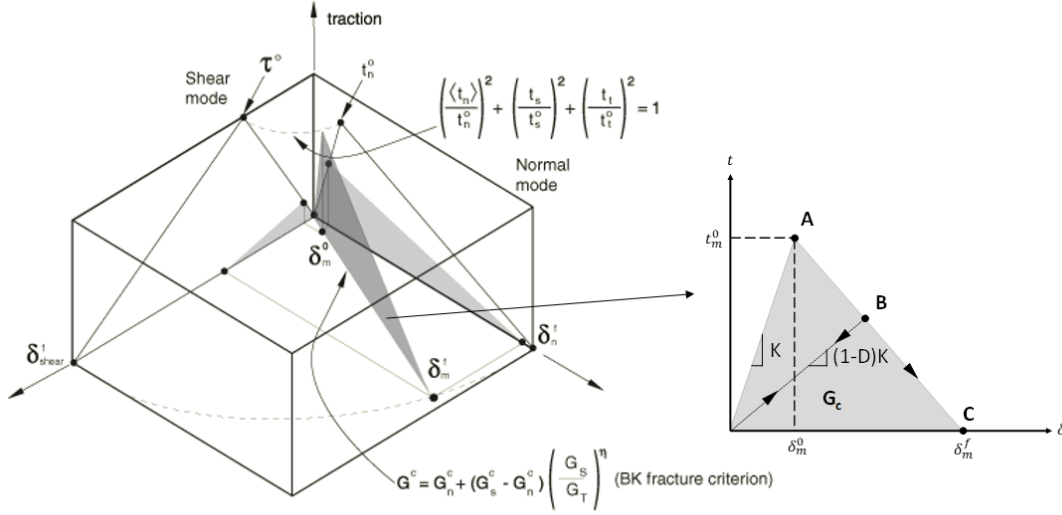


Figure 2-7. Bilinear cohesive law for mixed-mode delamination [23].

The total relative displacement for mixed-mode delamination, δ_m , at an arbitrary point (such as Point B) on line A-C is defined as follows [23], [29];

$$\delta_m = \sqrt{\langle \delta_n \rangle^2 + \delta_s^2 + \delta_t^2} = \sqrt{\langle \delta_n \rangle^2 + \delta_{shear}^2} \quad (2.19)$$

The relative displacement at the damage initiation for mixed-mode delamination, δ_m^0 , is obtained as follows [29];

$$\delta_m^0 = \begin{cases} \delta_n^0 \delta_t^0 \sqrt{\frac{1 + \beta^2}{(\delta_t^0)^2 + (\beta \delta_n^0)^2}}, & \delta_n > 0 \\ \delta_{shear}^0, & \delta_n \leq 0 \end{cases} \quad (2.20)$$

in which, β is the mixed-mode ratio and defined in Eqn. (2.21) for δ_n greater than zero:

$$\beta = \frac{\delta_{shear}}{\delta_n} \quad (2.21)$$

In the calculation of the failure displacement at the decohesion for mixed-mode delamination, δ_m^f , the Benzeggagh and Kenane [30] criterion is considered.

The Benzeggagh and Kenane (B-K) [30] criterion is a mixed-mode damage evolution criteria which takes into account the interaction of different fracture modes by providing a power-law relationship between fracture toughness values. The BK law model for the three-dimensional case is given in Eqn. (2.22):

$$G_{equiv\ c} = G_{IC} + (G_{IIC} - G_{IC}) \left(\frac{G_{II} + G_{III}}{G_I + G_{II} + G_{III}} \right)^\eta \quad (2.22)$$

where η is a parameter obtained from mixed-mode bending (MMB) experiments.

The failure displacement at the decohesion for mixed-mode delamination, δ_m^f , is defined in Eqn. (2.23) for the B-K criterion [30];

$$\delta_m^f = \begin{cases} \frac{2}{K\delta_m^0} \left[G_{IC} + (G_{IIC} - G_{IC}) \left(\frac{\beta^2}{1 + \beta^2} \right)^\eta \right] & \delta_n > 0 \\ \sqrt{(\delta_s^f)^2 + (\delta_t^f)^2}, & \delta_n \leq 0 \end{cases} \quad (2.23)$$

For any arbitrary point, δ_m , (such as Point B) on the line A-C for mixed-mode delamination, the determination of the damage variable (D) is straightforward by knowing the calculated values of δ_m^f and δ_m^0 .

2.3. Virtual Crack Closure Method (VCCT)

The Virtual Crack Closure Technique (VCCT) is predicated on Irwin's concept of crack closure integral and is appropriate for computing energy release rates of each mode [31]. VCCT calculates strain-energy release rates, with the presumption that the energy required to enlarge two separate crack faces by a certain amount is identical to the energy required to close these two separate crack faces by the same amount. In Figure 2-8, the crack will propagate when the Eqn. (2.24) is satisfied for pure opening mode. The figure and following equation are given for pure opening mode and both

can be expressed in two and three dimensions for in-plane and out-of-plane shear modes, respectively [31], [32].

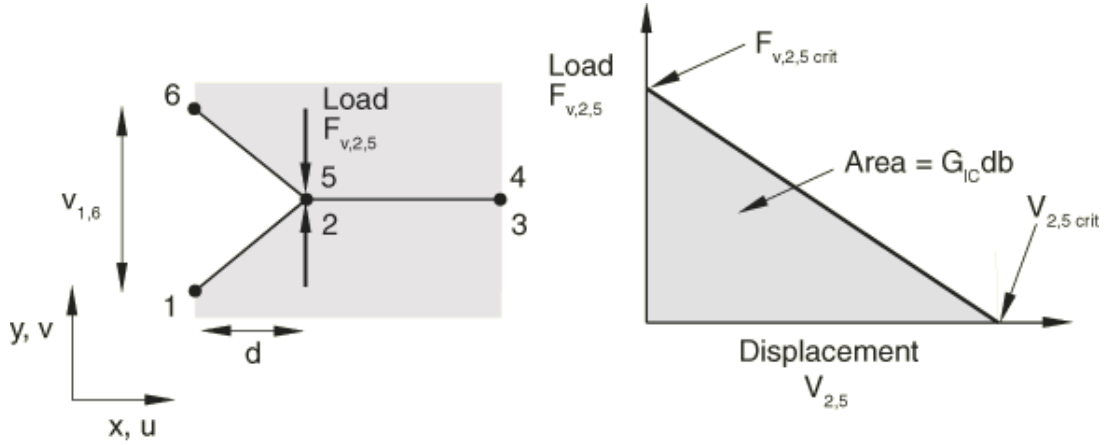


Figure 2-8. VCCT for Mode-I condition [33].

$$f = \frac{G_I}{G_{IC}} = \frac{1}{2} \left(\frac{v_{1,6} F_{v,2,5}}{bd} \right) \frac{1}{G_{IC}} \geq 1.0 \quad (2.24)$$

in which G_I is the strain energy release rate in the opening mode, G_{IC} is the critical strain energy release rate in the opening mode, $v_{1,6}$ is the displacement in y-direction between point 1 and point 6, $F_{v,2,5}$ is the force in y-direction between point 2 and point 5, b is the width of the specimen, and d is the length of the finite elements at the crack tip.

CHAPTER 3

UD LAMINATE

In this chapter, 2D and 3D finite element analyses of dynamic delamination in UD laminate are presented in detail. First, information about the generation of finite element models is given and then results obtained from 2D, and 3D finite element analyses are presented, respectively.

3.1. Material

The material used is AS4/8552 unidirectional prepreg with a density of 1580 kg/m^3 and cured ply thickness (CPT) of 0.188 mm. The elastic properties and strength values which are taken directly from Lopes et al. [34] are given in Table 3.1. Moreover, the interface properties of the used prepreg are given in Table 3.2. All interface values except strengths are taken from Lopes et al. [34]. Interface strengths denoted by t_I^0 and t_{II}^0 in Table 3.2 are obtained from experiments conducted and presented in the next section according to ASTM Standard D6415 [35] and ASTM Standard D2344 [36]. The curve fit factor obtained from mixed-mode bending (MMB) experiments, η , and the initial stiffness of the interface elements, E_0 , for mixed-mode energy release rate calculation are also given in Table 3.2.

Table 3.1. Elastic constants of HexPly AS4/8552 UD prepreg.

Elastic Properties	$E_{11} = 135000 \text{ MPa}; E_{22} = E_{33} = 9600 \text{ MPa}$
	$\nu_{12} = \nu_{13} = 0.32; \nu_{23} = 0.487$
	$G_{12} = G_{13} = 5300 \text{ MPa}; G_{23} = 3400 \text{ MPa}$

Table 3.2. Interface properties of HexPly AS4/8552 UD prepreg.

Interface Strength	$t_I^0 = 79.07 \text{ MPa}$
	$t_{II}^0 = t_{III}^0 = 106.4 \text{ MPa}$
Fracture Toughness	$G_{IC} = 0.28 \text{ N/mm}$
	$G_{IIC} = G_{IIIC} = 0.79 \text{ N/mm}$
B-K Criterion Constant (η)	1.45
Interface Stiffness	$E_0 = 2.6 \times 10^6 \text{ N/mm}^3$

The wave speeds (dilatational, shear, and Rayleigh wave) of the material are calculated using the formulas from Coker et al. [37].

The dilatational wave speed in the fiber direction can be calculated as;

$$c_d^{\parallel} = \sqrt{\left(\frac{c_{11}}{\rho}\right)}. \quad (3.1)$$

The dilatational wave speed perpendicular to the fiber direction can be calculated as;

$$c_d^{\perp} = \sqrt{\left(\frac{c_{22}}{\rho}\right)}. \quad (3.2)$$

The shear wave speed can be expressed in terms of density (ρ) and in-plane shear modulus as;

$$c_s = \sqrt{\left(\frac{c_{66}}{\rho}\right)} = \sqrt{\left(\frac{G_{12}}{\rho}\right)}. \quad (3.3)$$

The Rayleigh wave speed is the smallest of the roots obtained from the solution of Eqn. (3.4) in which stiffness matrix components are given for the plane stress state;

$$\left(\frac{c'_{11}c'_{22} - c'^2_{12}}{c'_{22}c'_{66}} - \frac{\rho v^2}{c'_{66}}\right) \left[\frac{c'_{22}}{c'_{11}} \left(1 - \frac{\rho v^2}{c'_{66}}\right)\right]^{1/2} - \frac{\rho v^2}{c'_{66}} \left(1 - \frac{\rho v^2}{c'_{11}}\right)^{1/2} = 0. \quad (3.4)$$

In their study, Coker et al. [37] observed that the crack accelerates up to a maximum value of critical speed, V_c , under Mode-II condition. Huang et al. [38] derived the critical speed (V_c) for plane stress analytically as follows [39];

$$V_c = \sqrt{\frac{c_{11}c_{22}-c_{12}^2}{c_{66}(c_{12}+c_{22})}} c_s. \quad (3.5)$$

In order to calculate the dilatational, shear, Rayleigh, and critical wave speeds of the considered material by using Equations (3.1) - (3.5), components of the plane stress stiffness matrix should be calculated. Five independent elastic constants characterize a transversely isotropic material. The stress-strain relation of a transversely isotropic material is given below for 3D case:

$$\begin{Bmatrix} \sigma_{11} \\ \sigma_{22} \\ \sigma_{33} \\ \sigma_{23} \\ \sigma_{13} \\ \sigma_{12} \end{Bmatrix} = \begin{bmatrix} c_{11} & c_{12} & c_{13} & 0 & 0 & 0 \\ c_{12} & c_{11} & c_{13} & 0 & 0 & 0 \\ c_{13} & c_{13} & c_{33} & 0 & 0 & 0 \\ 0 & 0 & 0 & c_{44} & 0 & 0 \\ 0 & 0 & 0 & 0 & c_{44} & 0 \\ 0 & 0 & 0 & 0 & 0 & \frac{(c_{11} - c_{12})}{2} \end{bmatrix} \begin{Bmatrix} \varepsilon_{11} \\ \varepsilon_{22} \\ \varepsilon_{33} \\ \gamma_{23} \\ \gamma_{13} \\ \gamma_{12} \end{Bmatrix} \quad (3.6)$$

The nonzero stiffnesses in Eqn. (3.6) are calculated as follows [40];

$$c_{11} = \frac{1 - \nu_{23}\nu_{32}}{E_2 E_3 \Delta} \quad (3.7)$$

$$c_{22} = \frac{1 - \nu_{13}\nu_{31}}{E_1 E_3 \Delta} \quad (3.8)$$

$$c_{12} = \frac{\nu_{21} + \nu_{31}\nu_{23}}{E_2 E_3 \Delta} = \frac{\nu_{12} + \nu_{13}\nu_{32}}{E_1 E_3 \Delta} \quad (3.9)$$

$$c_{23} = \frac{\nu_{32} + \nu_{12}\nu_{31}}{E_1 E_3 \Delta} = \frac{\nu_{23} + \nu_{21}\nu_{13}}{E_1 E_2 \Delta} \quad (3.10)$$

$$c_{13} = \frac{\nu_{31} + \nu_{21}\nu_{32}}{E_2 E_3 \Delta} = \frac{\nu_{13} + \nu_{12}\nu_{23}}{E_1 E_2 \Delta} \quad (3.11)$$

$$c_{33} = \frac{1 - \nu_{12}\nu_{21}}{E_1 E_2 \Delta} \quad (3.12)$$

$$c_{44} = G_{23} \quad (3.13)$$

$$c_{55} = G_{31} \quad (3.14)$$

$$c_{66} = G_{12} \quad (3.15)$$

$$\Delta = \frac{1 - \nu_{12}\nu_{21} - \nu_{23}\nu_{32} - \nu_{31}\nu_{13} - 2\nu_{21}\nu_{32}\nu_{13}}{E_1 E_2 E_3} \quad (3.16)$$

This 3D constitutive relation can be reduced for plane stress state by setting,

$$\sigma_{33} = 0 \quad \tau_{23} = 0 \quad \tau_{31} = 0 \quad (3.17)$$

Plane stress state stress-strain relationship can be found as:

$$\begin{Bmatrix} \sigma_{11} \\ \sigma_{22} \\ \tau_{12} \end{Bmatrix} = \begin{bmatrix} c'_{11} & c'_{12} & 0 \\ c'_{12} & c'_{22} & 0 \\ 0 & 0 & c'_{66} \end{bmatrix} \begin{Bmatrix} \varepsilon_1 \\ \varepsilon_2 \\ \gamma_{12} \end{Bmatrix} \quad (3.18)$$

Then plane stress stiffness matrix components can be calculated as follows:

$$c'_{11} = \frac{E_1}{1 - \nu_{12}\nu_{21}} = c_{11} - \frac{c_{12}^2}{c_{22}} \quad (3.19)$$

$$c'_{22} = \frac{E_2}{1 - \nu_{12}\nu_{21}} = c_{22} - \frac{c_{23}^2}{c_{22}} \quad (3.20)$$

$$c'_{12} = \frac{\nu_{21}E_1}{1 - \nu_{12}\nu_{21}} = c_{12} - \frac{c_{12}c_{23}}{c_{22}} \quad (3.21)$$

$$c'_{66} = G_{12} = c_{66} \quad (3.22)$$

The calculated wave speeds of the unidirectional composite material are provided in Table 3.3 for both the plane stress and plane strain conditions.

Table 3.3. Material wave speeds for AS4/8552 UD prepreg.

	c_d^{\parallel} (m/s)	c_d^{\perp} (m/s)	c_S (m/s)	c_R (m/s)	v_C (m/s)
Plane-stress	9277	2473	1831	1811	8045
Plane-strain	9377	2852	1831	1816	8045

3.2. Material Tests for Interlaminar Strengths

An accurate FEA of the delamination behavior of the curved laminate requires precise material properties. Even though the elastic properties of AS4/8552 UD material are widely available and used in the literature, the interlaminar properties can vary with

particular manufacturing processes. For this reason, experiments are conducted to obtain the interlaminar tensile and shear strengths of the AS4/8552 unidirectional material.

3.2.1. Curved Beam Strength (CBS) Test

Four-point bending experiments are conducted in order to determine interlaminar tensile strength (ILTS) of HexPly AS4/8552 UD Prepreg by following the standard ASTM test procedure [35].

Curved specimens are positioned in the 4-point bending fixture, as shown in Figure 3-1. Experiments are conducted using Shimadzu Autograph AGS-J 10 kN testing machine, and load is applied in the vertical direction at 0.5 mm/sec under displacement control.

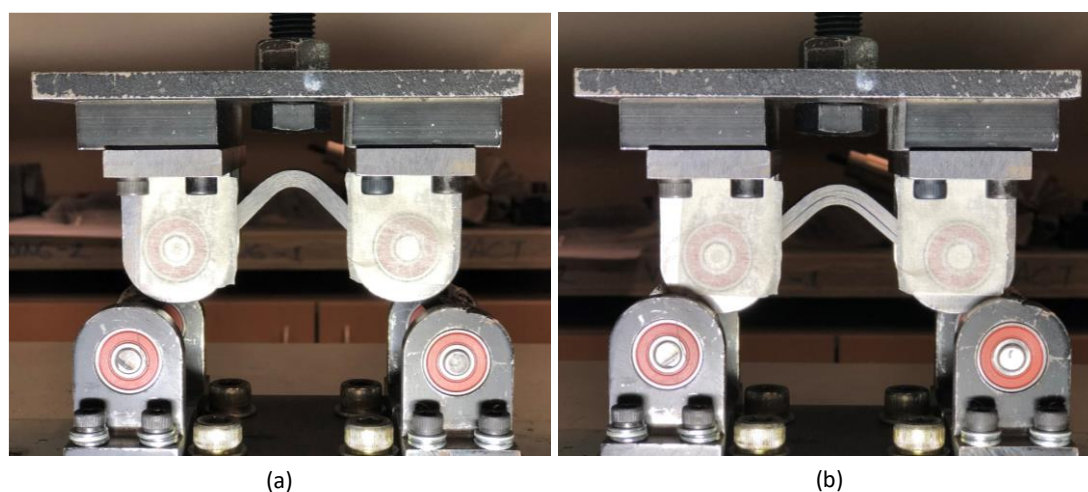


Figure 3-1. (a) Intact specimen positioned on 4-point bending test fixture (b) specimen after the experiment.

The line graph given in Figure 3-2 illustrates the load vs. displacement response of four specimens used in four CBS experiments. As is evident in the graph, the slopes of the curves are almost the same except one of the specimens, which has a slight difference. The maximum failure load or the strength values of the four specimens varies between 3529 N and 4744 N. Moreover, geometric dimensions and parameters used in the calculation of the curved beam strength are defined in Figure 3-3.

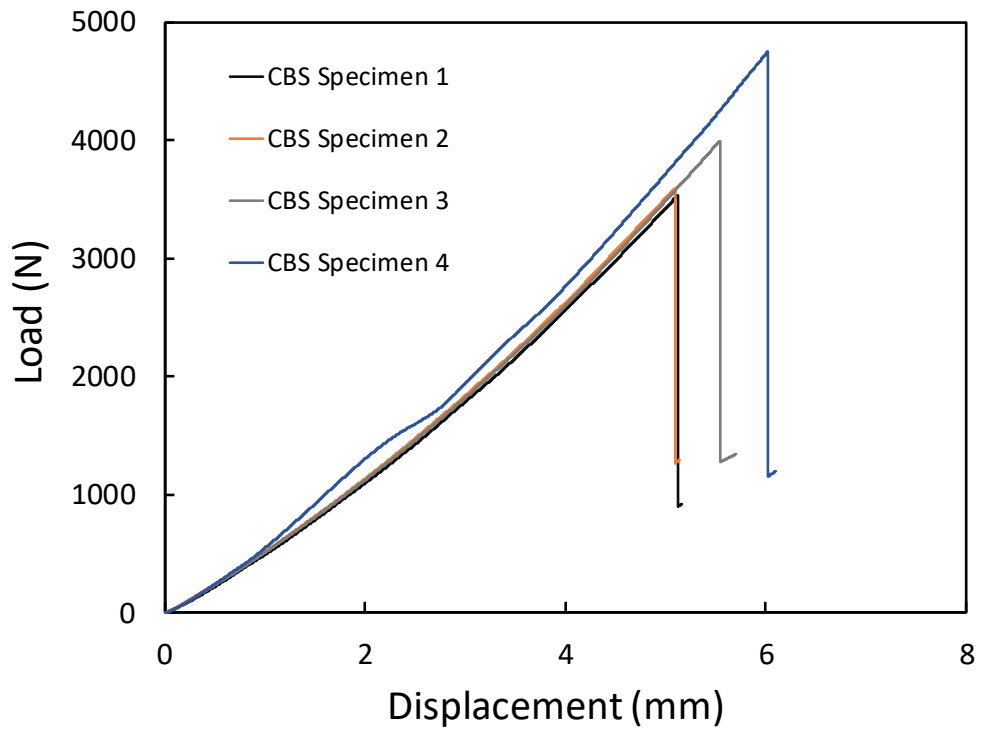


Figure 3-2. Load-displacement curves of four CBS specimens.

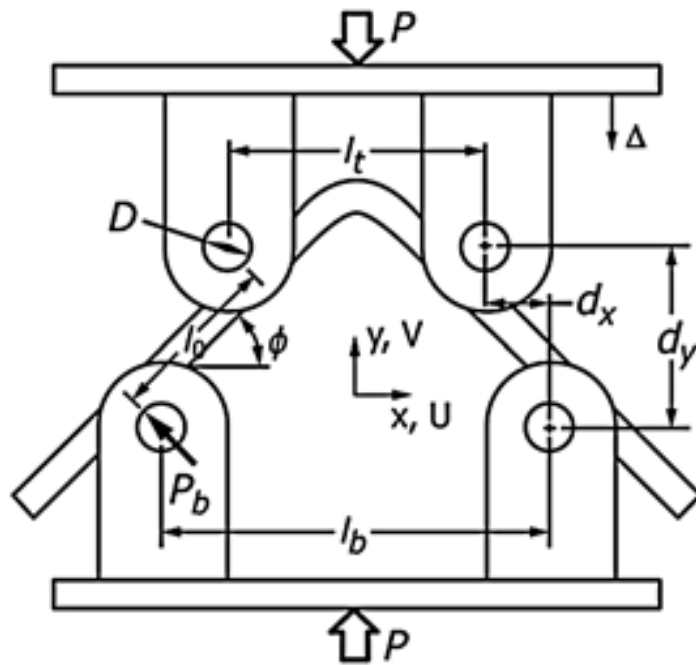


Figure 3-3. Geometric dimensions and parameters used in the calculation of the CBS [35].

The curved beam strength, applied moment per unit width, is calculated by using the below-given equation;

$$CBS = \frac{M}{w} = \frac{Pl_0}{w} = \frac{P}{2w\cos(\varphi)} \left(\frac{d_x}{\cos(\varphi)} + (D + t)\tan(\varphi) \right) \quad (3.23)$$

in which P refers to applied load at initial failure, w is the width of the specimen, and l_0 is the distance between the centerlines of a top and bottom cylindrical loading bars along the leg of the specimen. The angle between the specimen's leg and the horizontal line is defined as φ in Eqn. (3.23) and can be calculated by using the Eqn. (3.24) in terms of the diameter of the loading bars (D), the vertical distance between a top and bottom loading bars (d_y), the horizontal distance between a top and bottom loading bars (d_x) and the thickness of the specimen (t).

$$\varphi = \sin^{-1} \left(\frac{-d_x(D + t) + d_y\sqrt{d_x^2 + d_y^2 - D^2 - 2Dt - t^2}}{d_x^2 + d_y^2} \right) \quad (3.24)$$

The deflected vertical distance between a top and bottom loading bars (d_y) at the ultimate load can be obtained from Eqn. (3.25);

$$d_y = d_x \tan(\varphi) + \frac{D + t}{\cos(\varphi_i)} - \Delta \quad (3.25)$$

Since the interlaminar tensile strength is defined as the maximum radial stress at the failure, the maximum radial stress calculation results in interlaminar tensile strength. This value is calculated by a simple strength approach proposed by Kedward [3]:

$$\sigma_r^{max} = \frac{3CBS}{2t\sqrt{r_i r_o}} \quad (3.26)$$

The calculated curved beam strength of four different test specimens are presented in Table 3.4. The average of these four calculated curved beam strength values are used in the finite element analysis.

Table 3.4. Results of four CBS experiments.

Specimen	P_{\max} (N)	w(mm)	Δ	d_y	φ	t(mm)	CBS(N)	σ_r (MPa)
CBS Specimen 1	3529.5	24.90	5.117	29.33	0.668	5.52	2727.38	71.26
CBS Specimen 2	3591.0	24.75	5.091	29.30	0.668	5.48	2791.80	73.59
CBS Specimen 3	3994.0	24.75	5.540	28.82	0.657	5.46	3030.28	80.23
CBS Specimen 4	4744.5	24.76	6.013	28.49	0.644	5.56	3520.64	91.19
Average								79.07

3.2.2. Short Beam Strength (SBS) Test

Three-point bending experiments are conducted to measure interlaminar shear strength (ILSS) of HexPly AS4/8552 UD Prepreg by following the standard ASTM test procedure [36].

Figure 3-4 (a) and Figure 3-4 (b) show the test configuration for the short-flat laminate and the specimen positioned in the three-point bending fixture, respectively. Experiments are conducted using Shimadzu Autograph AGS-J 10 kN testing machine, and load is applied in the vertical direction at 0.5 mm/sec under displacement control.

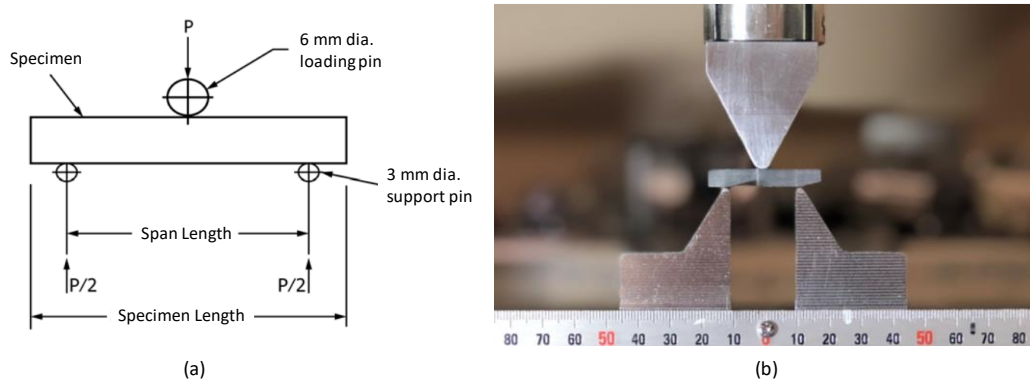


Figure 3-4. (a) 3-point bending test configuration [36], (b) specimen positioned on the three-point bending fixture.

The line graph given in Figure 3-5 illustrates the load vs. displacement response of four different specimens used in the short-beam strength experiments. As is evident in the graph, the behavior of the all specimens are almost the same until the failure load except SBS Specimen-1. The peak load recorded during the experiments is 10052 N which corresponds to 2.19 mm displacement for SBS Specimen-4.

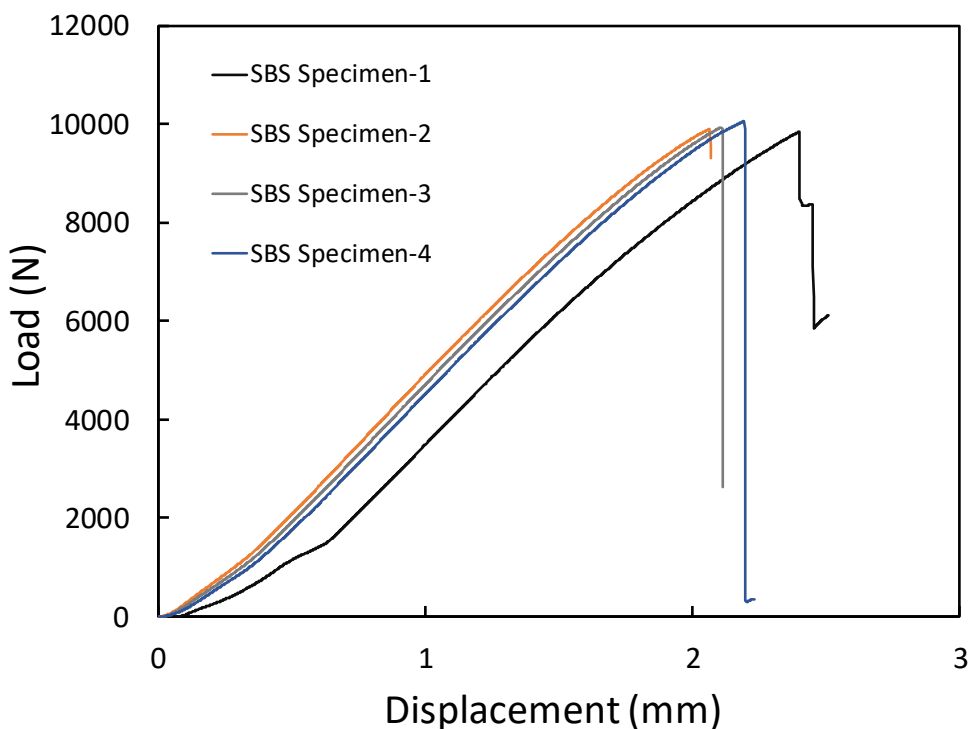


Figure 3-5. Load-displacement curves of four SBS specimens.

ASTM standard test method for short-beam strength [36] specifies that unless mid-plane interlaminar failure has been clearly observed in the experiments, the calculated short-beam strength cannot be attributed to the interlaminar shear strength. The expected failure mode to obtain interlaminar shear strength (ILSS) is identified in Figure 3-6 (a), and the observed failure mode in the experiments is presented in Figure 3-6 (b).

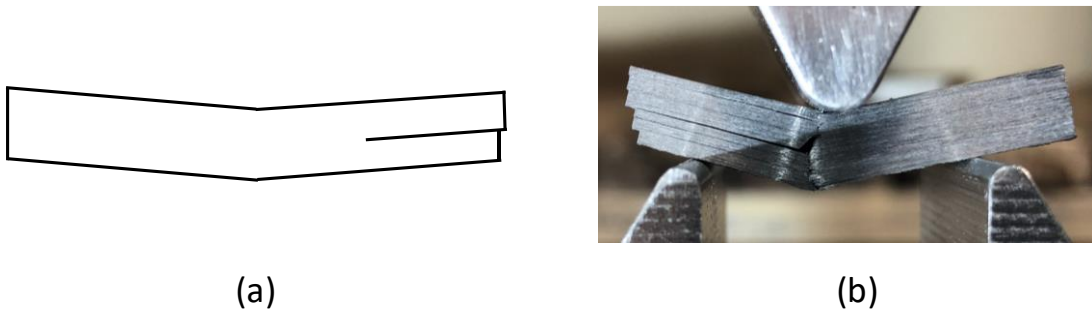


Figure 3-6. Interlaminar shear failure (a) identified in the standard ASTM test procedure (b) in the short beam strength test.

The short-beam strength is calculated by using the Eqn. (3.27) in terms of the peak load observed during the experiment (P_m), width of the specimen (b) and the measured thickness of the specimen (h).

$$F^{sbs} = 0.75 \times \frac{P_m}{b \times h} \quad (3.27)$$

The summary of the calculations for four different specimens are presented in Table 3.5 and the average of the four calculated short-beam strength values is taken and used in the analysis as interlaminar shear strength.

Table 3.5. Results of four SBS experiments.

Specimen	P_{max} (N)	b (mm)	h (mm)	SBS (MPa)
SBS Specimen-1	9833.0	11.96	5.86	105.22
SBS Specimen-2	9896.5	12.02	5.83	105.92
SBS Specimen-3	9922.0	11.93	5.87	106.26
SBS Specimen-4	10051.50	11.93	5.84	108.20
Average				106.40

3.3. Geometry and Boundary Conditions

Both 2D and 3D finite element models corresponding to the experimental configuration of the curved unidirectional CFRP composite laminate are developed. The geometrical properties of the considered specimen are illustrated in Figure 3-7. The upper and lower arm length (l) of the considered specimen is 76.36 mm. Inner radius (r_i) and width (w) of the specimen are 8.0 mm and 25 mm, respectively. The laminate is composed of 30 UD plies of CFRP with a ply thickness of 0.188 mm which corresponds to 5.64 mm total thickness.

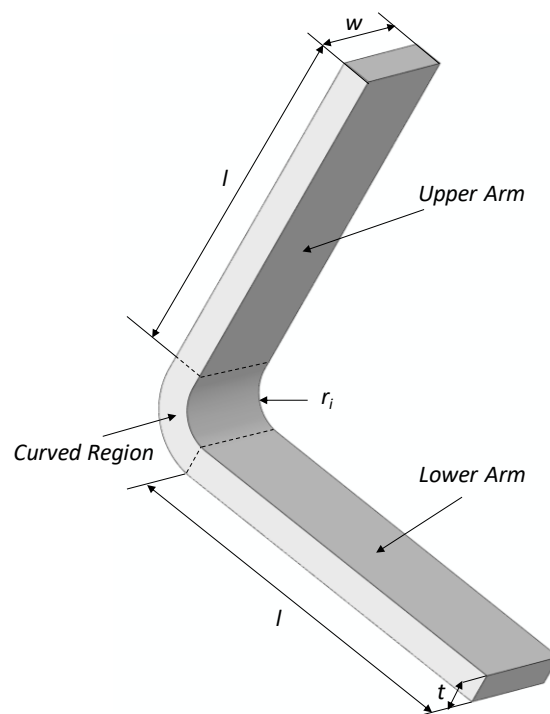


Figure 3-7. Specimen geometry for the curved unidirectional laminate.

In the experiments, displacement is prescribed to the specimen at the ends of the arms. The design of the experimental test fixture and installation of the specimen create combined loading at the curved region. The schematic of the experimental configuration is shown in Figure 3-8. The specimen ends are bolted to the freely rotating pins through which the axial load is applied in y-direction as shown in Figure 3-8 (a). The magnified view in Figure 3-8 (b) shows the applied loading through the

bolts at the ends of the specimen without constraining the rotation through freely rotating pins.

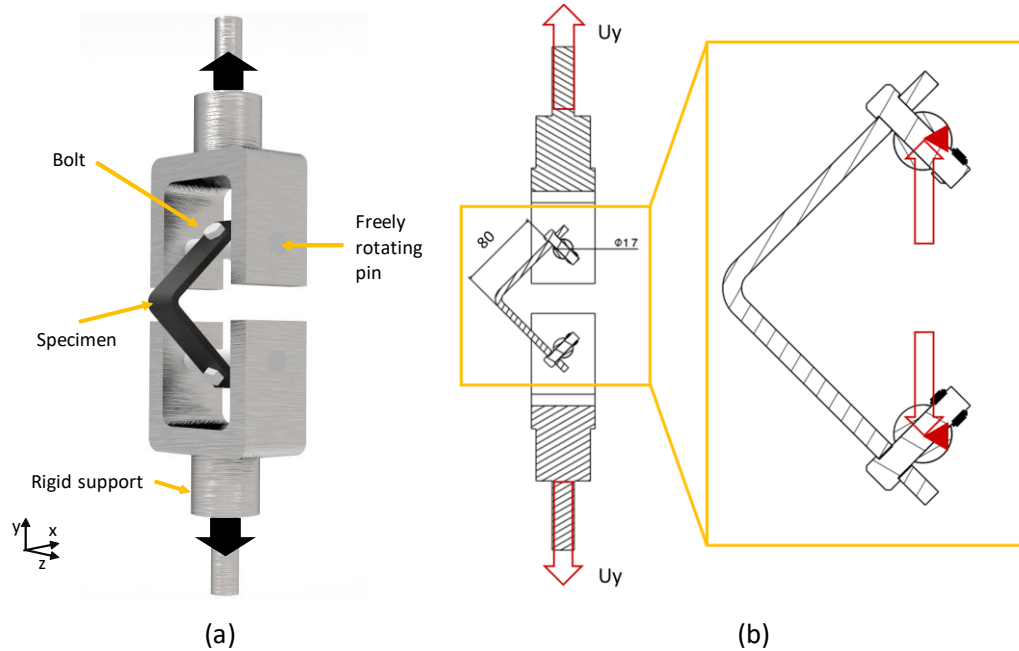


Figure 3-8. Schematic of (a) experimental configuration showing how the specimen is located in the fixture and (b) the load transfer to the specimen through the freely rotating pins.

The finite element idealization of the load and boundary conditions for 2D and 3D finite element models are shown in Figure 3-9 (a) and (b), respectively. In order to simulate the experimental configurations correctly, load and boundary conditions are imposed on the specimen using kinematic couplings which link the load introduction points to the specimen edge in all degrees of freedom. The finite element model of the specimen is allowed to move in the y-direction at the upper load introduction point and rotation around the z-axis is allowed at both upper and lower load introduction points. Allowing rotation around the z-axis accommodates a freely rotating pin clearly. All other degrees of freedom are fixed at both load introduction points. The maximum applied displacement at the upper load introduction point is set to 7 mm in both 2D and 3D models.

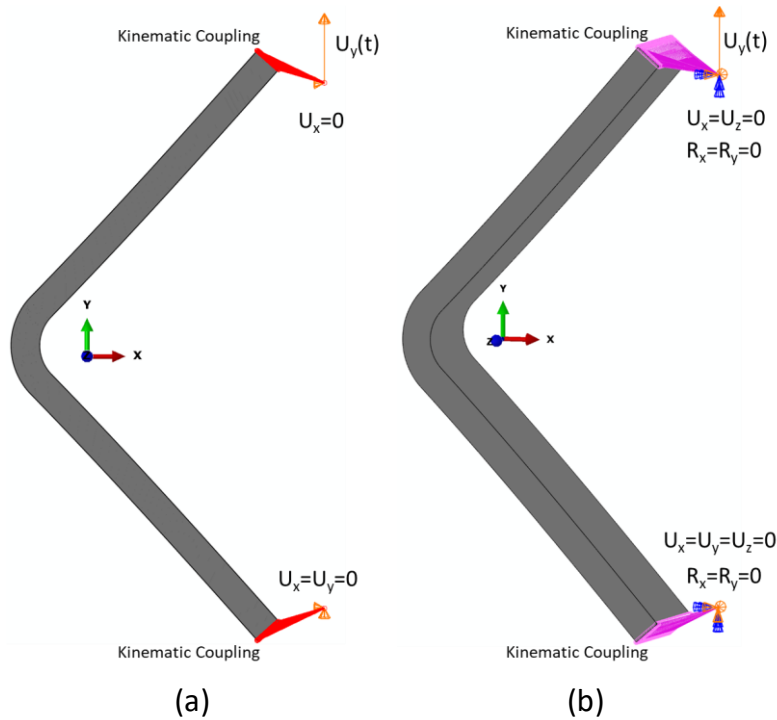


Figure 3-9. Finite element idealization of the boundary conditions for (a) 2D finite element model and (b) 3D finite element model.

Using explicit dynamics to solve quasi-static problems in their real-time is prohibitively expensive in terms of computation time, which is directly proportional to analysis step time. Thus, simulating the real physical process at an artificially high speed is usually desirable. In general, inertia forces will not play a dominant role in quasi-static loading with an appropriate step time. Since the considered composite material is not rate-dependent, in this study artificially increasing the loading rate is preferred rather than mass-scaling technique.

The loading rate is determined with modal analysis since the dominant mode will be the first mode shape in quasi-static simulations. The first natural frequency is attained as 649 Hz, which corresponds to 0.0015 s as a result of the modal analysis. This result reveals that the shortest step time for the quasi-static analysis should be 0.0015 s. The step time is selected as 0.007 s conservatively, which ends in a loading rate of 1 m/s in the quasi-static simulations presented here. Prescribed displacement is applied as a smooth-step function, which is formulated in Eqn. (3.28):

$$U(t) = U_L \left[10 \left(\frac{t}{t_L} \right)^3 - 15 \left(\frac{t}{t_L} \right)^4 + 6 \left(\frac{t}{t_L} \right)^5 \right] \quad (3.28)$$

where, U_L is the maximum prescribed displacement value and t_L is the determined total step time. Moreover, the loading profile is depicted in Figure 3-10.

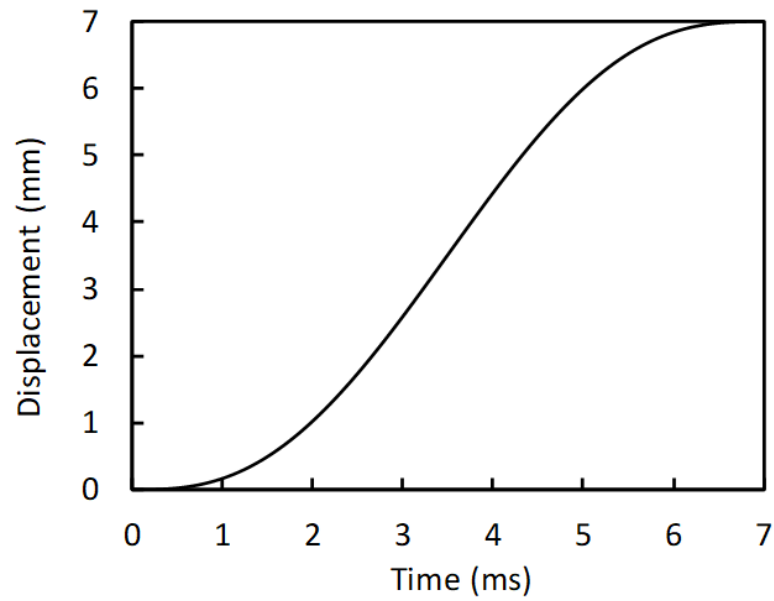


Figure 3-10. Loading profile of smooth step for quasi-static simulation of UD laminate.

3.4. Finite Element Modelling

3.4.1. 2D FEM

In the two-dimensional finite element model of the UD laminate, each layer is discretized with two 4-node bilinear reduced integration elements (CPE4R) through the thickness. Two-dimensional cohesive elements (COH2D4) available in ABAQUS/Explicit element library are employed to model all of the twenty-nine interfaces. The thickness of the cohesive elements at each interface are taken to be $t=0.001$ mm. The enhanced hourglass control approach is considered for bulk material representation to prevent hourglassing. The penalty stiffness of the interface elements (E_0) is calculated as 2.6×10^6 N/mm³ by using Eqn. (2.11), and the exponent of the B-K law is specified as 1.45. The sweep mesh technique is used to align the cohesive elements with thickness direction, as shown below in Figure 3-11 from the bottom to the top face. The correct definition of thickness direction is crucial in cohesive element modelling since the element elongation will represent the separation of the laminas.

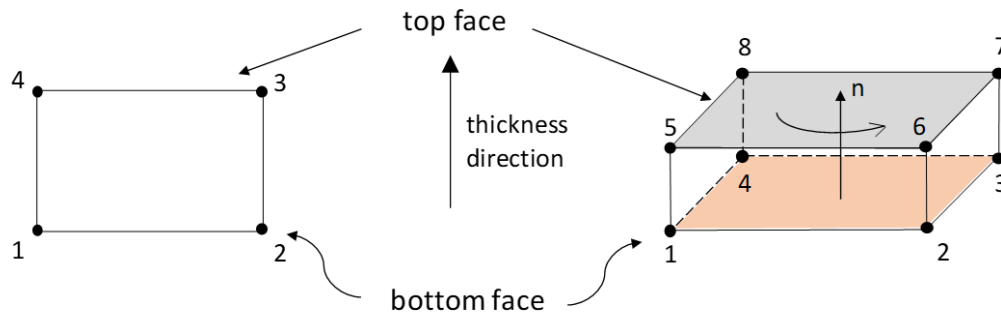


Figure 3-11. Top and bottom faces of (a) 2D cohesive element and (b) 3D cohesive element with the defined thickness direction.

The mesh density of the finite element model is determined after a detailed mesh study that considers load-displacement behavior and stress distributions at different sections. The magnified view of the mesh at the mid-line is shown, and element dimensions in this region are summarized in Figure 3-12. In the graphic, the parameters measured along the ordinate are the element height which changes from 84 μ m to 143 μ m due

to the curved region and element width $w_e=94 \mu\text{m}$ which is constant through the thickness direction.

The two-dimensional finite element model of the UD laminate includes 52200 first-order quad elements of type CPE4R and 25230 first-order quad elements of type COH2D4. The total number of elements is 77430. Moreover, the total number of nodes is 78392 which corresponds to 156966 number of degrees of freedom. ABAQUS calculates the stable time increment as 1.472×10^{-10} s. The analysis was performed on a high-performance cluster consisting of 72 CPU cores. A single simulation takes more than 33 hrs.

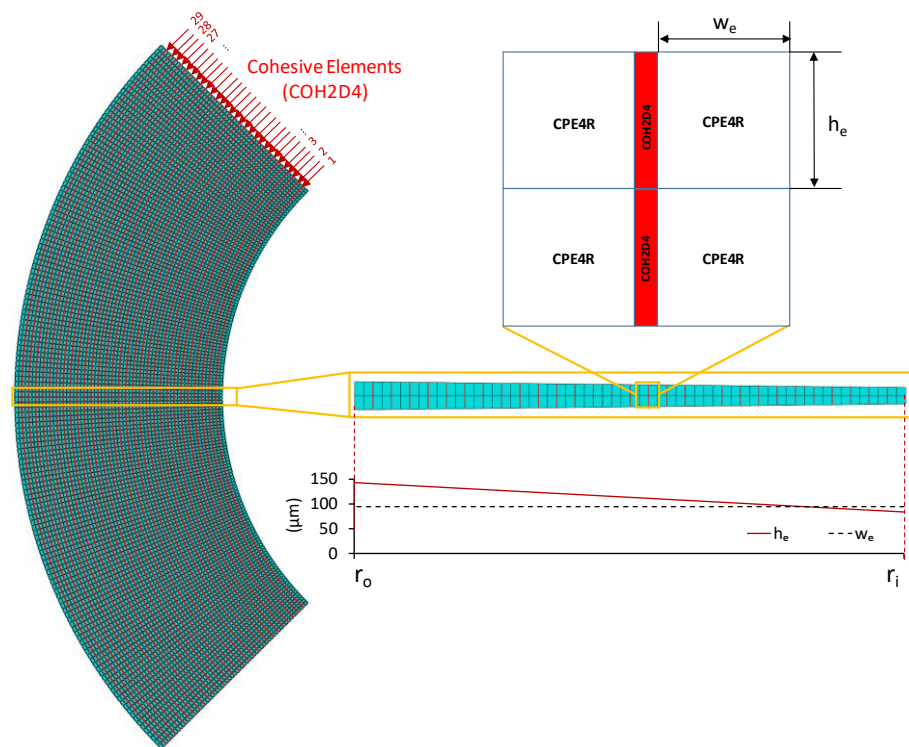


Figure 3-12. Magnified view of the mesh at the center-line of the 2D FEM of UD laminate and details of interface modelling.

The interpenetration of adjacent layers behind the crack tip in the arm region may occur after separation due to large applied displacements. Thus, contact interactions in normal and tangential directions are considered between the adjacent layers with the General Contact Algorithm of ABAQUS to prevent the layer interpenetration.

3.4.2. 3D FEM

In the three-dimensional FE model of the UD laminate, the bulk region is discretized by reduced integration continuum solid elements, which are denoted as C3D8R in ABAQUS/Explicit element library. Unlike the two-dimensional FE model, the three-dimensional FE model includes only one interface, which is located between the 12th and 13th layers from the inner radius as shown below in Figure 3-13. This location is determined from the results of two-dimensional analysis. The main reason for modelling only one interface in the 3D FE model is to reduce computational time. The mesh density of the 3D model differs from the 2D model again due to computational efficiency. Using the same mesh density of the two-dimensional finite element model and modelling all twenty-nine interfaces would result in more than 10 million elements, which requires excessive CPU time.

Since all layers of the UD laminate have the same orientation, the first twelve layers (defined as inner region in Figure 3-13) are considered as a single layer with a thickness of 12×0.188 mm. Then, this single layer is discretized with eight elements through the thickness to generate a reduced 3D FE model. The remaining eighteen layers (defined as outer region in Figure 3-13) are considered as another single layer with a thickness of 18×0.188 mm and discretized with twelve elements through the thickness. Around the curve region, there are two elements per three degrees sweep and in the width direction there are 88 elements. The three-dimensional FE model includes 936320 first-order hexahedral elements of type C3D8R and 46816 first-order hexahedral elements of type COH3D8. The total number of elements is 983136, and the total number of nodes is 1043616 with 3142602 numbers of degrees of freedom. ABAQUS calculates the stable time increment as 1.651×10^{-8} s. The analysis was performed on a high-performance cluster consisting of 72 CPU cores. A single simulation takes around more than 32 hrs. As mentioned in the section on 2D finite element modelling, contact interactions in normal and tangential directions are also considered for 3D FE models between the adjacent layers with the General Contact Algorithm of ABAQUS to prevent the layer interpenetration.

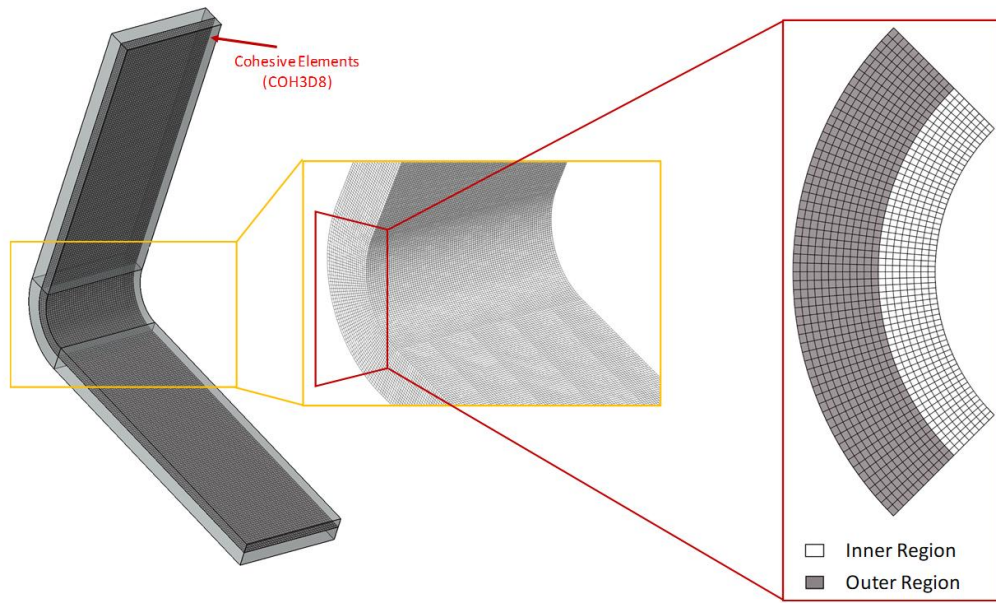


Figure 3-13. 3D FE model details in terms of interface modelling and mesh density.

3.5. Results

3.5.1. 2D FEA Results

Excessive oscillations on the load-displacement curve due to failure of cohesive elements are ubiquitous in simulations when the explicit solver is employed. In literature, several studies mentioned severe oscillations and their solutions for these oscillations [43]. Although larger analysis duration would result in a load-displacement curve with less severe oscillations, it increases the computational cost of the analysis. An approach to lessen the computational cost of the analysis is to follow the sequential analysis (with larger analysis duration for explicit solver) proposed by Gozluklu and Coker [16] in which the implicit analysis is used for the linear behavior before failure, and explicit analyses is used after the peak (failure) load. However, this sequential method requires the re-run of the model. Without re-running another simulation, we decided to evaluate the energy history during the analysis to attain the filtered load-displacement curve which is believed to be the most accurate behavior.

Strain and fracture energies as a function of time for the 2D Plane strain FEA of the curved UD CFRP laminate are shown in Figure 3-14. Fracture energy remains zero until the sudden increase at $t= 5.7000$ ms. The sudden increase in the fracture energy and sudden decrease in the strain energy is attributed to the instantaneous load drop (intersonic delamination) observed in the experiments [1]. As shown in the magnified view, the sudden increase in the fracture energy almost stops at $t= 5.7112$ ms which is actually the endpoint of the sudden load-drop in the load-displacement curve. The high-frequency oscillations on the load-displacement curve after $t= 5.7112$ ms are filtered by adding a linear trend line in MS Excel, and the load values between 5.7000 and 5.7112 ms are attained by considering a linear decrease between the corresponding load values of these two time instants.

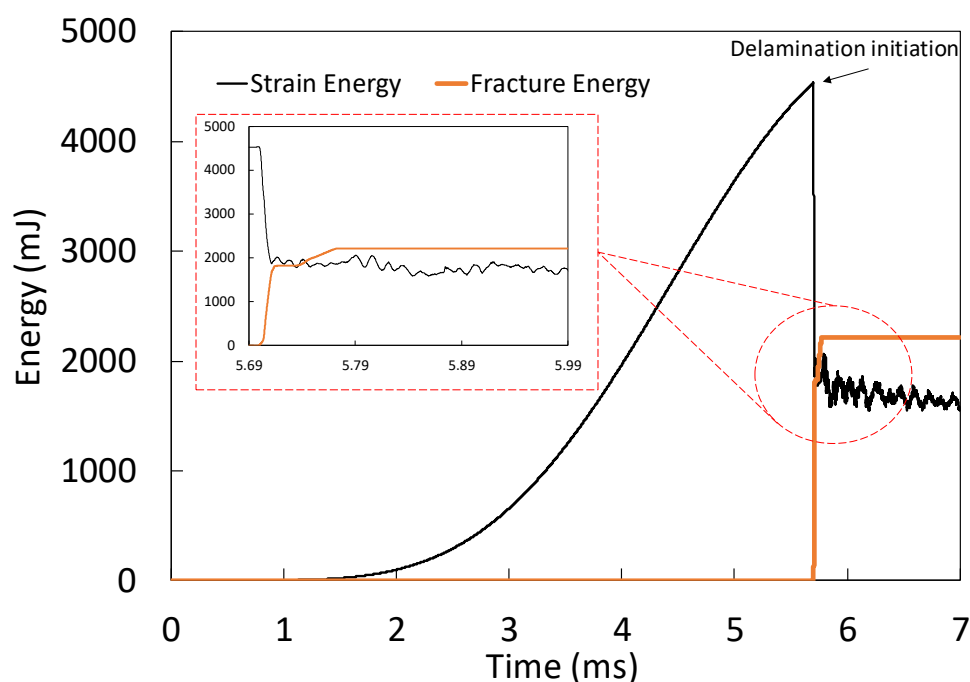


Figure 3-14. Strain and fracture energy history of 2D FEA of curved UD CFRP laminate.

The same approach used in the evaluation of fracture and strain energies can also be used for internal and kinetic energies since the sudden increase in the kinetic energy and sudden decrease in the internal energy is attributed to the instantaneous load drop (intersonic delamination) observed in the experiments [1]. The kinetic and total strain

(internal) energy history is presented in Figure 3-15. The comparison of kinetic and internal energy shows that the applied quasi-static approach is appropriate, since the kinetic energy is small relative to internal energy throughout the analysis.

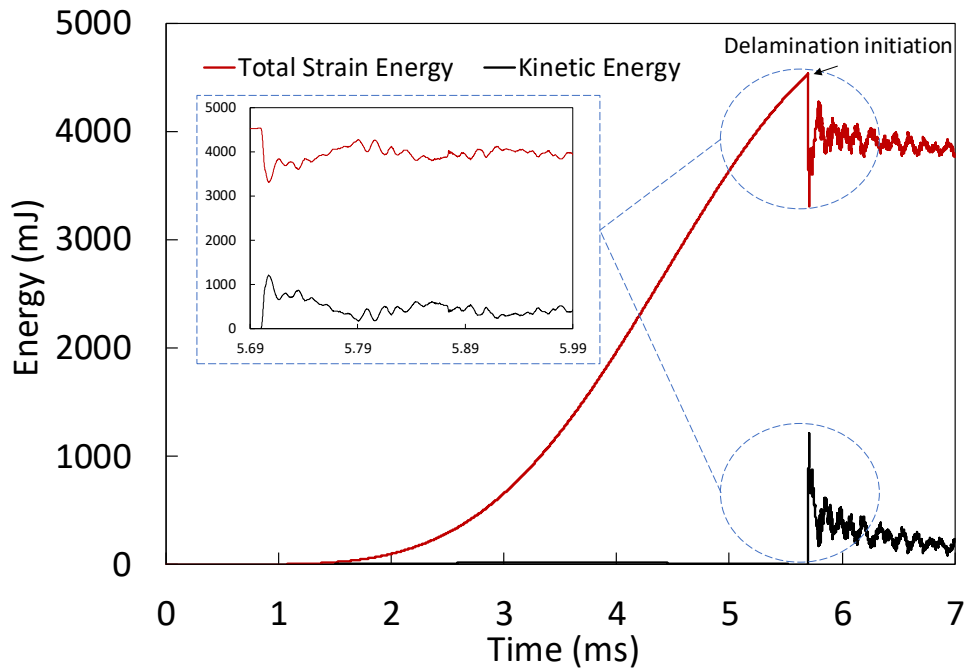


Figure 3-15. Internal and kinetic energy history of 2D FEA of curved UD CFRP laminate.

The load-displacement response of the curved UD CFRP laminate from the 2D FEA is shown on the left-hand side of Figure 3-16 with grey color. The load-displacement data (grey) is filtered in order to eliminate high-frequency noise, which occurs mainly due to the reflection of stress waves at the material boundaries after the failure of the interface elements. Both filtered and unfiltered curves show linear elastic behavior until the failure load of 1379 N. After the peak load (Point a), a sudden dynamic failure occurs which extends to both arms from the curved region. The stiffness of the UD laminate before failure is 206.91 N/mm, which shows good agreement with the experimental results as 218 N/mm [1]. The delamination reaches the arm region in 4 μ s and causes a 346 N reduction in the load-carrying capacity of the intact UD CFRP laminate (Point b). The total load drop occurs in 11.3 μ s when the crack extends for 46.02 mm (Point c). The length of the crack at the arm region at “Point c” corresponds

to 43% of the arm length. Finally, the simulation is completed as the maximum applied displacement value is reached. The final deformed shape of the curved UD CFRP laminate is shown in Figure 3-16 (Point d). The second stiffness is calculated to be 45.03 N/mm.

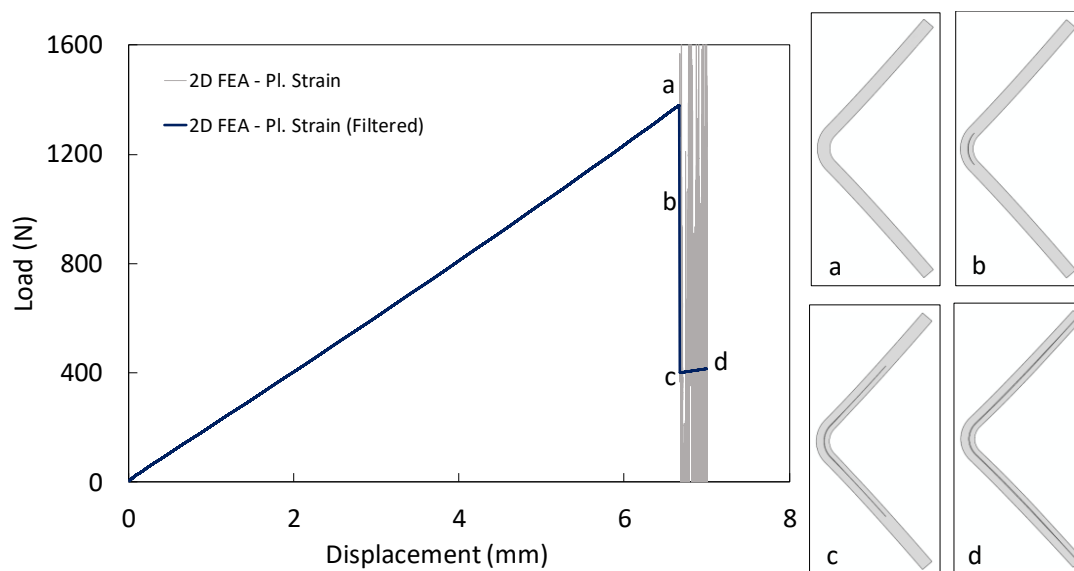


Figure 3-16. Load-displacement curves for 2D FEA of curved UD CFRP laminate under quasi-static loading and crack locations on load-displacement curve for critical points.

Evolution of the opening stress, σ_{33} , contours in the curved region of UD CFRP laminate before and after failure are shown in Figure 3-17. Although the simulations are performed for the whole geometry, only the upper part is plotted here for the visualization since the results are symmetric according to the mid-line. Continuous radial stress distribution at the curved region is disrupted as the damage variable of the interface elements reaches 0.999 at 0.3 μ s before the delamination initiation. Delamination initiates when the applied displacement reaches 6.67 mm (1379 N) at $t=0.0057$ s. This time is considered as t_0 from now on. After delamination initiation, due to high radial stresses shown by red color, it propagates dynamically in the curved region for 3.9 μ s. The speed of the crack tip can be inferred from the concentration of stress distribution at the crack tip. The stress concentration at the crack tip shows that crack travels at very high speeds in the beginning and slows down as it propagates to

the arm. The stress concentration in front of the crack tip also decreases as the crack slows down.

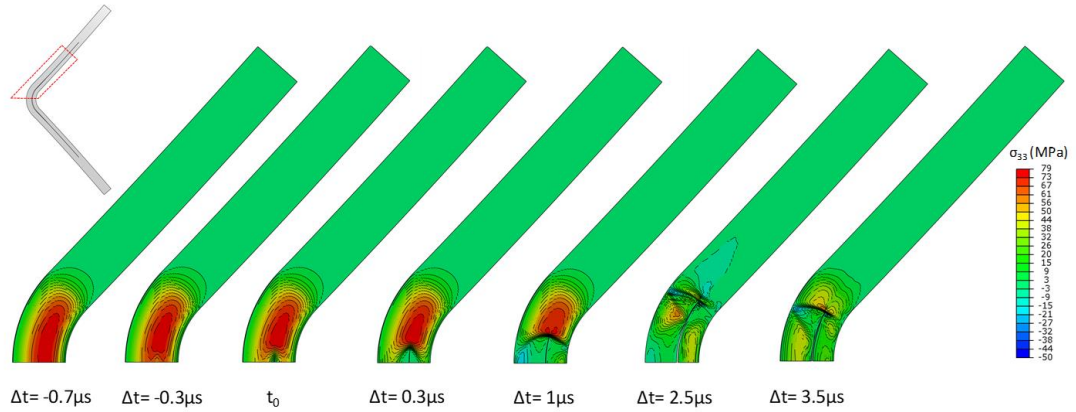


Figure 3-17. Evolution of the opening stress contours in the curved region of UD CFRP laminate before and after delamination onset.

Figure 3-18 shows the normal stress contours, σ_{33} , of four instants as the delamination propagates through the upper arm. Shear Mach waves radiating from the crack tip in the shape of inclined normal stresses are pointed out by red lines. Other inclined stress waves behind the shear Mach wave front can be attributed to the reflections of the waves from the free surfaces of the specimen. Local hot spots of stress concentrations are observed on the sliding crack surfaces due to elastodynamic waves.

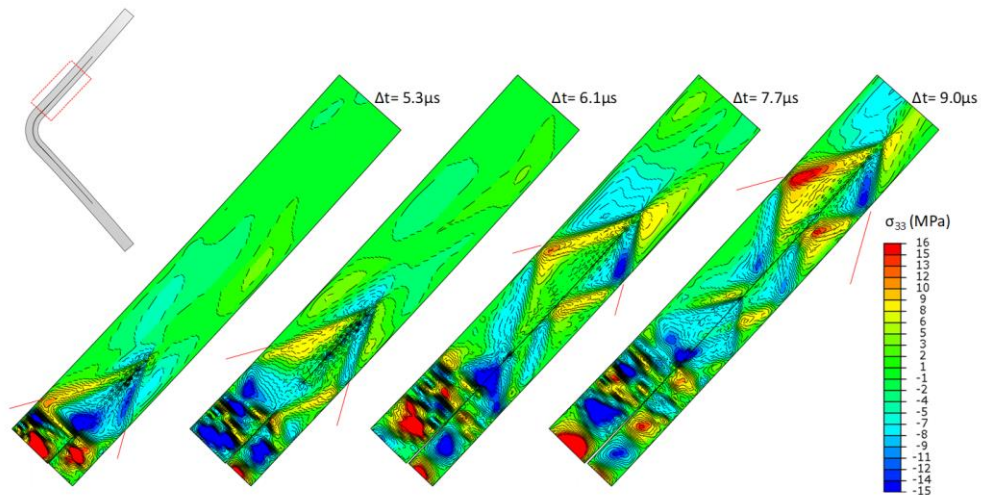


Figure 3-18. Normal stresses at the upper arm and shear Mach wave fronts pointed out with red lines.

The crack length is determined by using these snapshots at different time instants and the crack tip speed is calculated from the derivative of the crack length using moving three-point quadratic line fit. The line graph given in Figure 3-19 shows how the crack extension and crack tip speed changes with time.

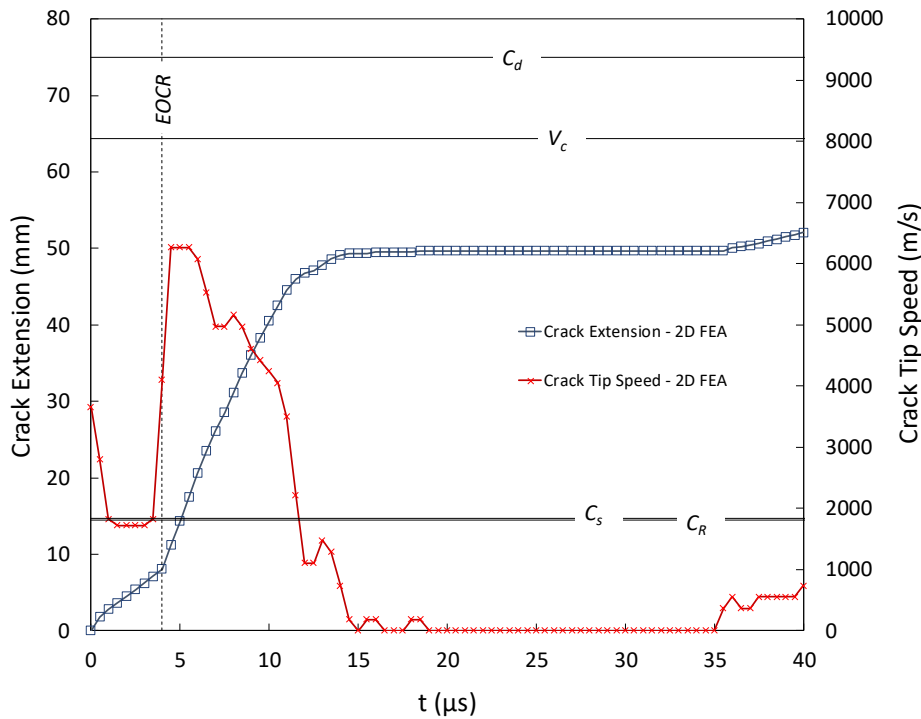


Figure 3-19. Crack extension and crack tip speed versus time curves for delamination propagating through upper arm of curved UD CFRP laminate.

It is clear from the previous radial stress plots that delamination initiation at the curved region is Mode-I dominated. Under Mode-I dominancy, a crack cannot exceed Rayleigh wave speed. Therefore, crack tip speed at the initiation can be neglected. After initiation, delamination grows at sub-Rayleigh speed in the curved region. The crack reaches the upper arm region at $t=3.9 \mu\text{s}$ which corresponds to a crack length of 8.06 mm. Crack tip speed hits a peak value of 6264 m/s which is above the shear wave speed of the material in the arm region. The crack extension reaches 46.76 mm in 12 μs . The sharp rise in the crack extension can be attributed to the intersonic delamination propagation. Although the crack tip speed fluctuates slightly between

shear wave speed and critical wave speed for eight μs , the main trend is downward. Afterwards, crack decelerates to sub-Rayleigh speeds around 1000 m/s at $t=12.5 \mu\text{s}$. The crack tip propagates at sub-Rayleigh speeds for six μs and then remains steady for 16.5 μs having the crack length of 49.70 mm. Detailed inspection of crack extension and tip speeds reveals that the crack passes material shear wave speed and travels in an approximate speed of 6000 m/s, which lies between the shear wave speed and the critical wave speed. Hence, the crack propagation in the arm region under Mode-II domination is intersonic. The shear Mach waves radiating from the crack tip can be observed in Figure 3-18. These waves also indicate that the crack is moving faster than the shear wave speed of the bulk material at the interface [18].

Virtual Crack Closure Technique (VCCT) analysis is performed to attain the strain energy release rates at the crack tip. The line graph given in Figure 3-20 illustrates the strain energy release rates for Mode-I (G_I) and Mode-II (G_{II}) as a function of crack length along curved UD CFRP laminate.

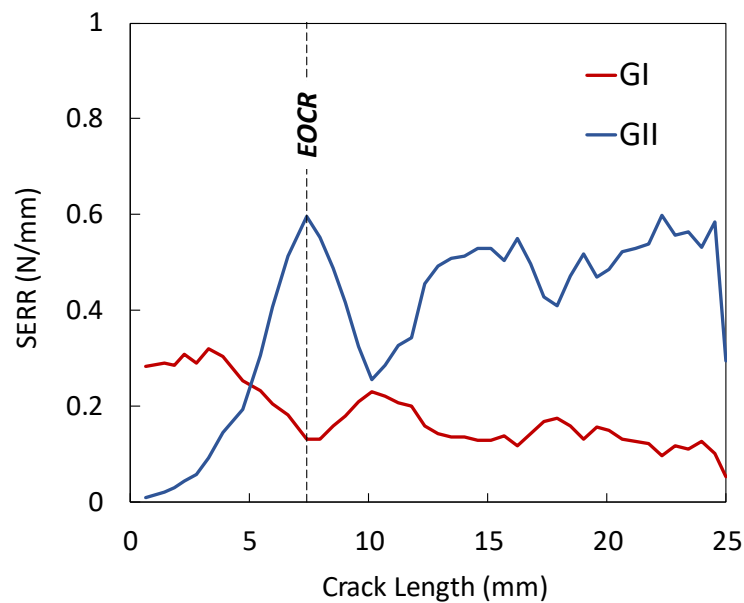


Figure 3-20. Strain energy release rates for Mode-I and Mode-II as a function of crack length along curved UD CFRP laminate.

Crack initiates under pure Mode-I condition where the critical Mode-I SERR is 0.28 N/mm. Delamination grows in the curved region under Mode-I dominance. As it develops both in the curved and arm region, the effect of Mode-II becomes visible and from that time on the delamination propagates under mixed-mode loading until the end of the loading.

The phase angle, Ψ , is calculated with the following formula to see the mixed-mode effect on the delamination propagation:

$$\Psi = \tan^{-1} \left(\sqrt{\frac{G_{II}}{G_I}} \right) \quad (3.29)$$

The mode-mixity defined by phase angle is given as a function of crack length in Figure 3-21 showing that the Mode-I dominant delamination in the center of the curved region ($\Psi = 0^\circ$) transitioning to Mode-II dominant delamination growth in the arm region ($\Psi \approx 80^\circ$).

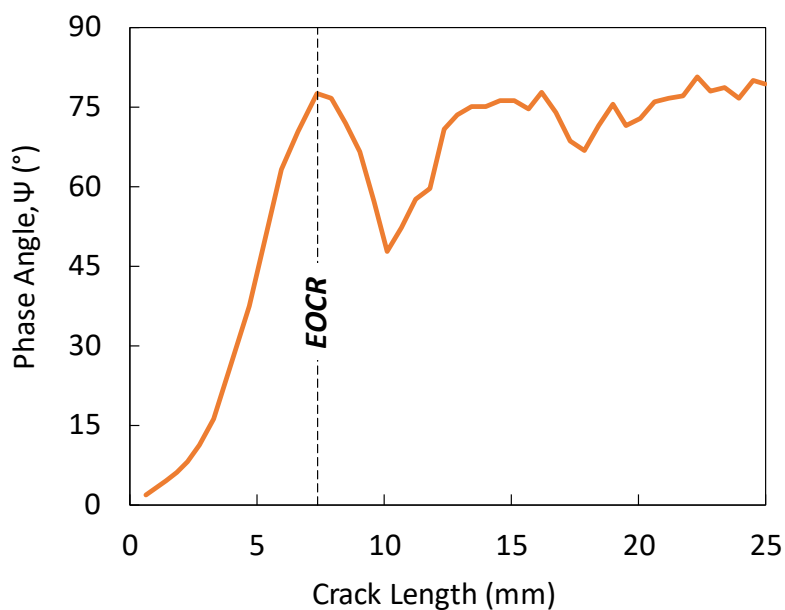


Figure 3-21. The mode-mixity defined by phase angle as a function of crack length.

3.5.2. 3D FEA Results

The excessive oscillations on the load-displacement curve of 3D FEA of the curved UD CFRP laminate are filtered by examining the history of strain and fracture energy extracted during the simulations as done in 2D FEA.

History plots of the strain and fracture energies for the 3D FE model of the curved UD CFRP laminate appears, as shown in Figure 3-22. Fracture energy remains zero until the sudden increase at $t = 5.7070$ ms. As the damage occurs and propagates, the fracture energy dissipated during the failure of interface elements increases instantaneously. As shown in the magnified view, the sudden increase in the fracture energy almost stops at $t = 5.7490$ ms which is actually the endpoint of the sudden load-drop in the load-displacement curve. The high-frequency oscillations on the load-displacement curve after $t = 5.7490$ ms are filtered by adding a linear trend line in MS Excel, and the load values between 5.7070 and 5.7490 ms are attained by considering a linear decrease between the corresponding load values of these two time instants.

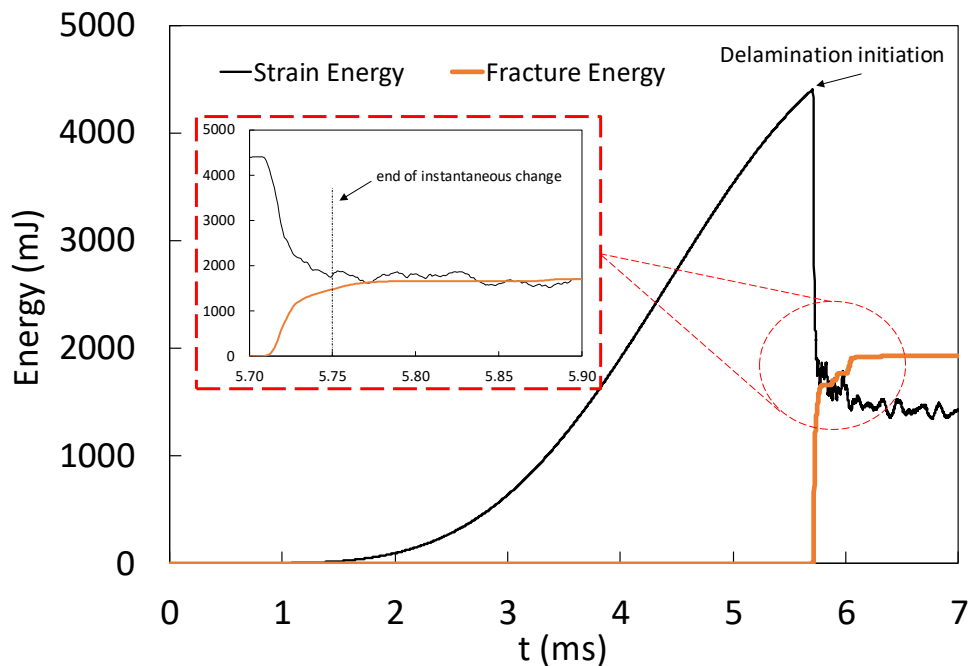


Figure 3-22. Strain and fracture energy history for 3D FEA of curved UD CFRP laminate.

The kinetic and total strain (internal) energy history is presented in Figure 3-23. At $t=5.7070$ ms, total strain energy decreases suddenly and the kinetic energy increases in the same manner. Both kinetic and total strain energy oscillates significantly as the delamination propagates through the arms. Comparison of the kinetic and total strain (internal) energy history shows that the kinetic energy is small relative to internal energy throughout the analysis. The criterion for quasi-static loading that kinetic energy must be small relative to total strain energy has been satisfied, even for the severe increase during the delamination onset.

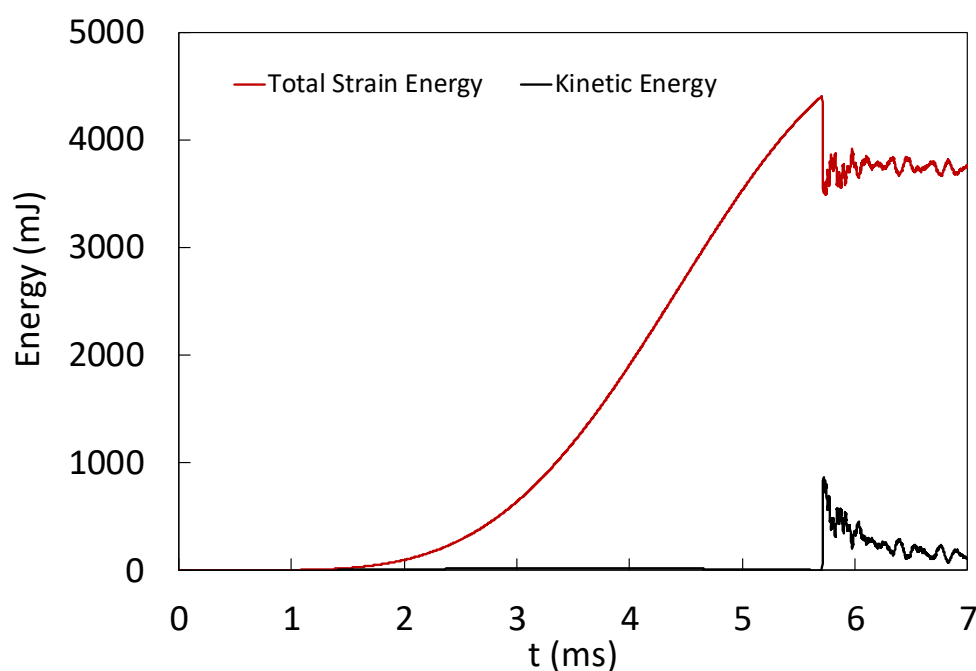


Figure 3-23. Internal and kinetic energy history for 3D FEA of curved UD CFRP laminate.

The load-displacement response of curved UD CFRP laminate from the 3D FEA is shown in the left-hand side of the Figure 3-24 with grey color. The load-displacement data (grey) is filtered in order to eliminate high-frequency noise, which occurs mainly due to the reflection of stress waves at the material boundaries after the failure of the interface elements. Both filtered and unfiltered curves show linear elastic behavior until the failure load of 1338.52 N. After the peak load (Point a), a sudden dynamic failure occurs which extends to both arms from the curved region. The stiffness of the

UD laminate before failure is 200.61 N/mm, which shows good agreement with the experimental results as 218 N/mm [1]. The delamination at the free edge reaches the arm region in 14 μ s and causes a 314 N reduction in load carrying capacity of the intact curved UD CFRP laminate (Point b). The total load drop occurs in 42 μ s when the edge crack extends for 47.55 mm and center crack extends for 41.79 mm (Point c). The length of the crack at the arm region at “Point c” corresponds to 42% of the arm length. Finally, the simulation is completed as the maximum applied displacement value is reached. The final deformed shape of the curved UD CFRP laminate is shown in Figure 3-24 (Point d). The second stiffness is calculated to be 96.41 N/mm.

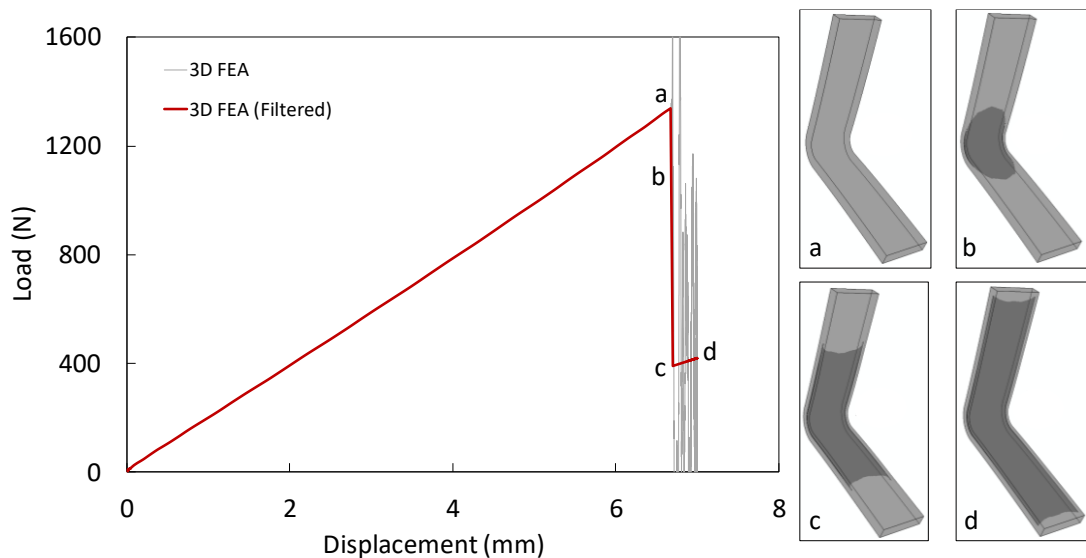


Figure 3-24. Load - displacement curves for 3D FEA of curved UD CFRP laminate under quasi-static loading and crack locations on load-displacement curve for critical points.

Delamination initiation and propagation inside the specimen can be clearly seen in Figure 3-25 where the delamination region for each time frame is colored as dark grey. The delamination initiates exactly at the center of the specimen along the width direction. Then it propagates in two directions; into the arm region and towards the free edge of the specimen. The crack tip propagating through the arm region (parallel to the longitudinal direction) is called center crack, and the crack tip propagating through the width direction and after reaching the free edge continues through the arm region is called edge crack. The crack tip speed in the width direction is calculated to

be sub-Rayleigh and is not inspected in detail. Since the crack front is almost symmetric in both directions that crack propagates, only one half of the delamination front is investigated in detail by considering one crack tip at the center and one crack tip at the free edge. As illustrated in Figure 3-25, center crack is initially faster than the edge crack, but as soon as the edge crack reaches the free-edge it gains a peak speed of 5000 m/s, catching up and passing the center crack. Afterwards, since there is not sufficient energy for intersonic crack propagation, both edge crack tip and center crack tip propagate at sub-Rayleigh wave speeds to the end of the loading.

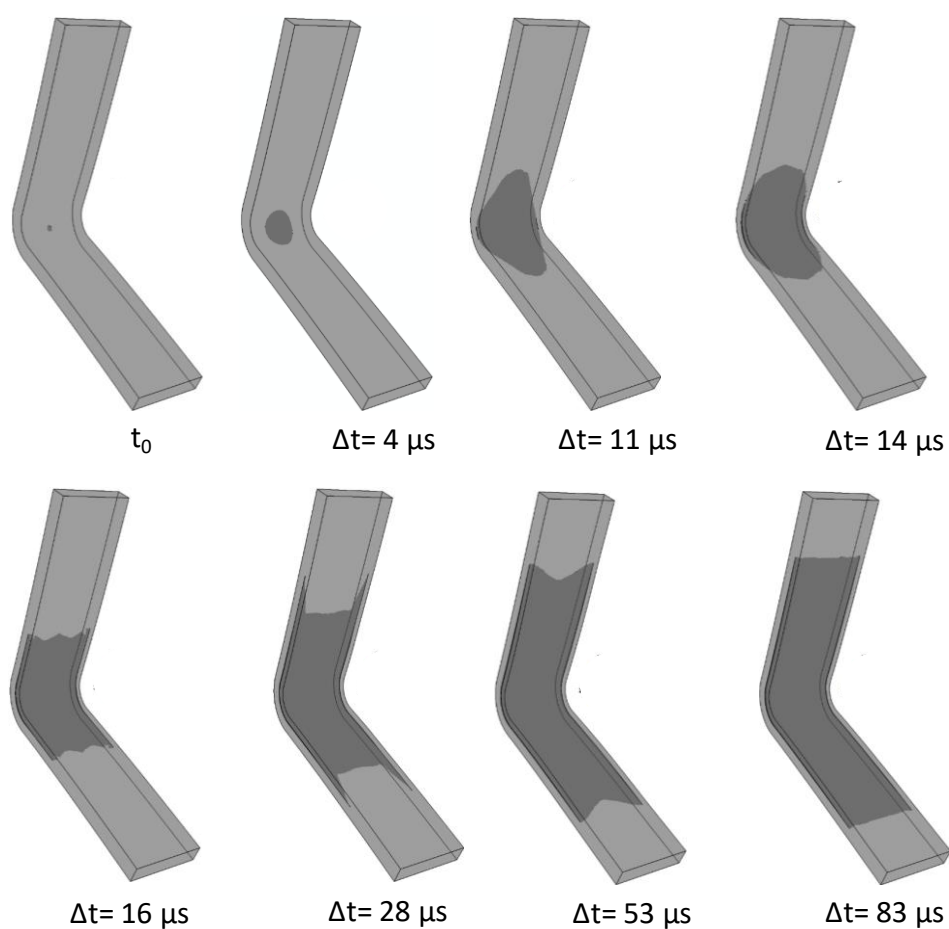


Figure 3-25. Delamination initiation and propagation path inside the curved UD CFRP laminate.

The radial stress fields of center ($W/2$) and edge (W) sections in the upper-half curved region of the 3D FE model before and after failure are presented in Figure 3-26. Although the simulations are performed for the whole geometry, only the upper-half

is plotted here for visualization since the results are symmetric according both to the mid-line and center-line. Continuous radial stress distribution at the curved region is disrupted as the damage variable of the interface elements reaches 0.98 at one μs before delamination initiation. Delamination initiates when the applied displacement reaches 6.67 mm (1339 N). After initiation of the center crack, it propagates to the arm region in 7 μs . During this time, no delamination is observed at the edge section.

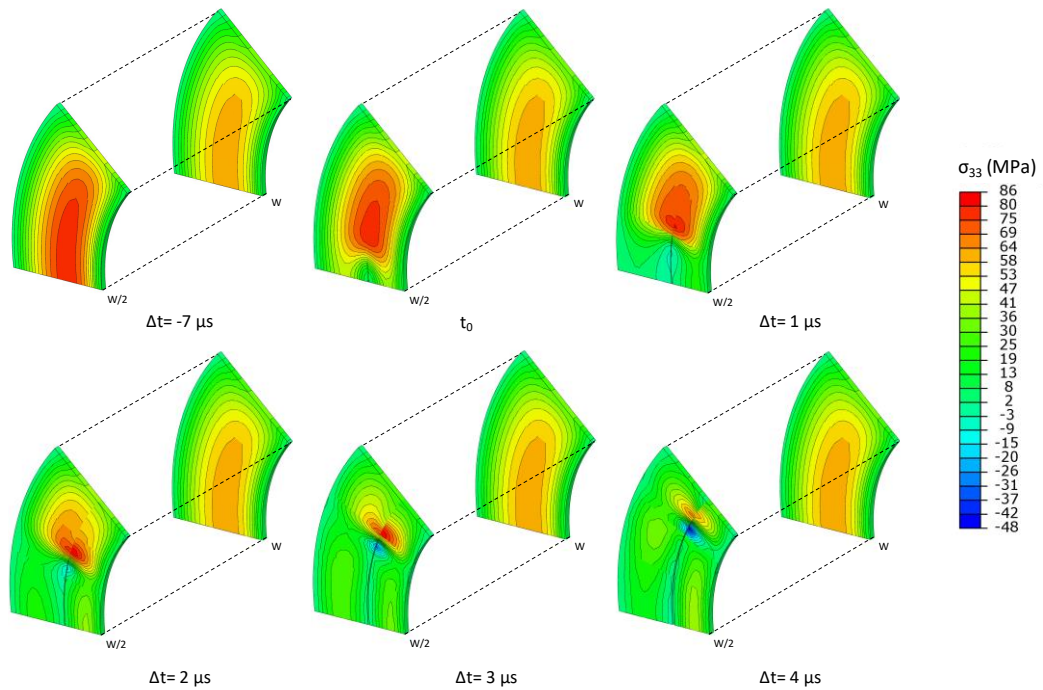


Figure 3-26. Contours of radial stresses at the center and edge sections of the curved UD CFRP laminate before and after center crack initiation.

Contours of normal stresses at the center and edge sections are given in Figure 3-27 for the time instants of $\Delta t = 8 \mu\text{s}$, $\Delta t = 9 \mu\text{s}$ and $\Delta t = 10 \mu\text{s}$. The normal stress lines in front of the crack tip in Figure 3-27 can be attributed to the shear Mach waves, since the center crack propagates faster than the material shear wave speed at the considered time frames and the crack propagation is under Mode-II dominance in this region.

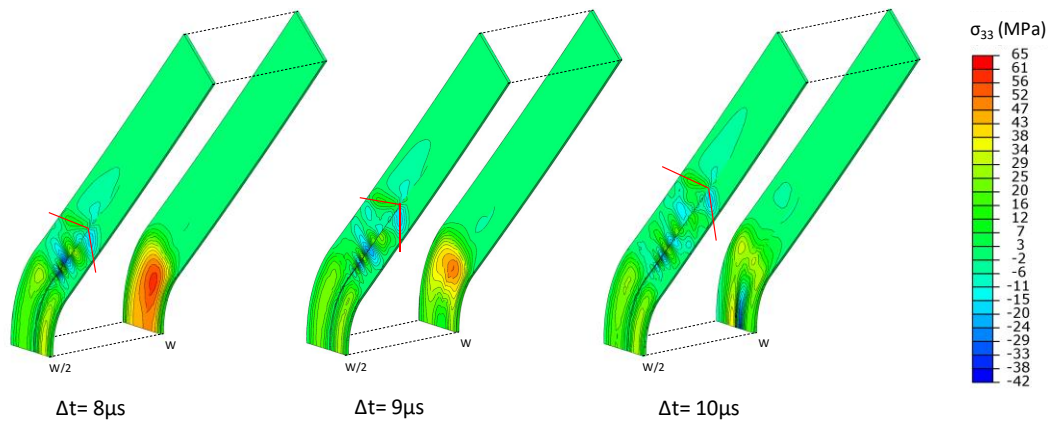


Figure 3-27. Crack propagation in the center section of upper arm region after the initiation of center crack with normal stress lines forming the shear Mach wave front.

Crack propagation in the edge section of the upper arm region after edge crack initiation with normal stress lines forming the shear Mach wave front is illustrated in Figure 3-28. As soon as the edge crack reaches the arm region, it sustains a speed value of 5000 m/s as mentioned earlier. Similar to the center crack, normal stress lines in front of the edge crack tip are attributed as shear Mach waves as shown in Figure 3-28.

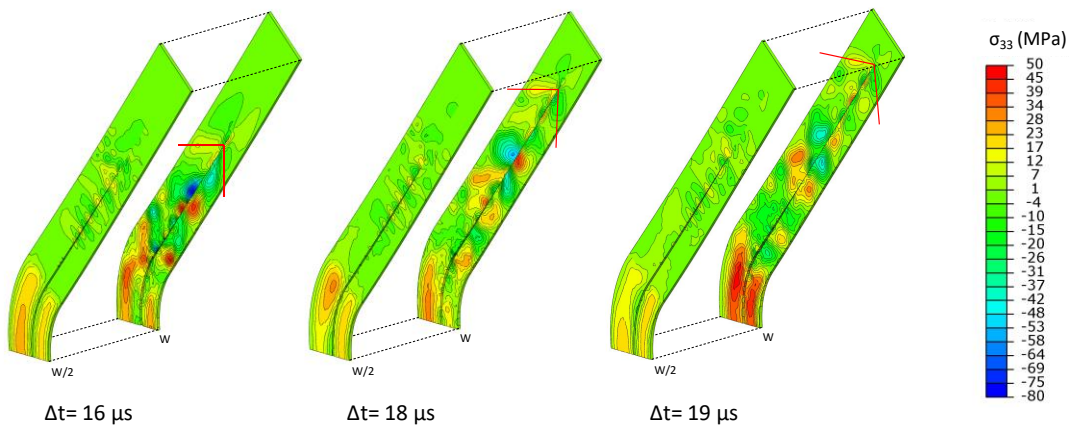


Figure 3-28. Crack propagation in the edge section of upper arm region after edge crack initiation with normal stress lines forming the shear Mach wave front.

Center crack extension is determined by using the snapshots at different time instants, and center crack tip speed is calculated from the derivative of the crack length using moving three-point quadratic line fit. The center crack extension and tip speeds as a

function of time are plotted in Figure 3-29 in which ‘EOCRC’ defines the end of the curve region at the center plane. Center crack tip propagates at sub-Rayleigh speed around 1300 m/s until $\Delta t = 6 \mu\text{s}$. Between $\Delta t = 6 \mu\text{s}$ and $\Delta t = 7 \mu\text{s}$, the center crack reaches the arm of the specimen as it speed-ups. Afterwards, the center crack tip speed reaches its maximum value of $V_m = 3233 \text{ m/s}$ at $\Delta t = 8 \mu\text{s}$. Following the maximum speed, the center crack tip speed gradually slows down to sub-Rayleigh speed as it propagates through the specimen arm.

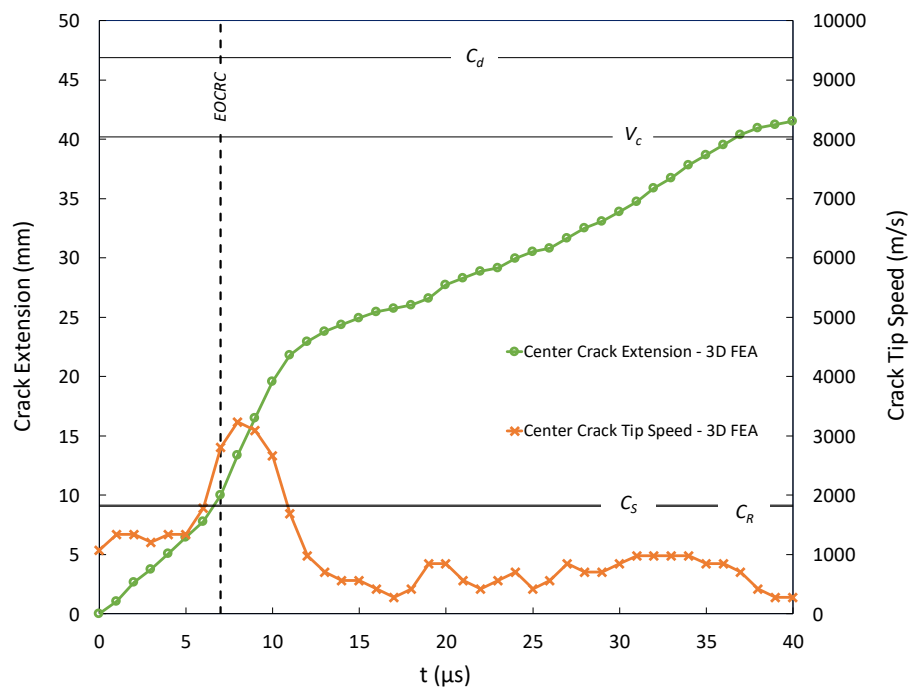


Figure 3-29. Center crack extension and tip speeds for the curved UD CFRP laminate.

Edge crack extension is determined by using the snapshots at different time instants, and edge crack tip speed is calculated from the derivative of the crack length using moving three-point quadratic line fit. The edge crack extension and tip speeds as a function of time are plotted in Figure 3-30 in which ‘EOCRE’ defines the end of the curve region at the free edge. Edge crack occurs when the transverse crack at the curved region reaches the free edge of the specimen at $\Delta t=11 \mu\text{s}$. After four μs from the edge crack onset, it passes to the arm region. In the arm region, it develops to intersonic speeds for approximately ten μs .

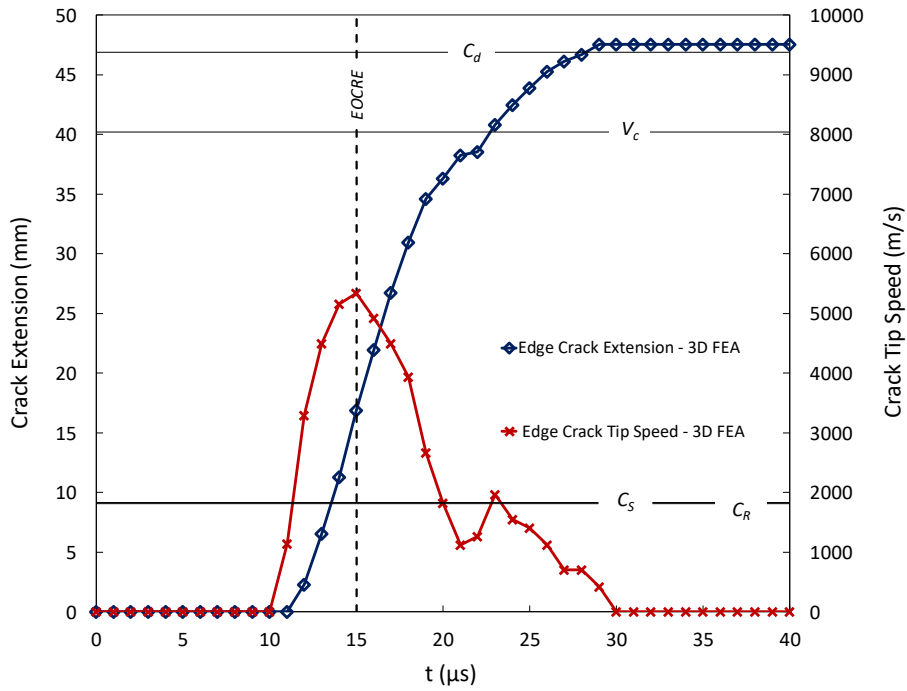


Figure 3-30. Edge crack extension and crack tip speeds for the curved UD CFRP laminate.

Mode-Mixity

The strain energy release rates (SERR) in all the three fracture modes are obtained by using the Virtual Crack Closure Technique (VCCT). A 3D finite element model is generated in conjunction with cohesive surface behaviour between adjacent sub-laminates, as defined earlier in the 3D FEM section. This model is loaded until the initial delamination occurs, since initial delamination or crack is required for a VCCT analysis. Then with this deformed configuration, the loading is continued with the defined VCCT criterion for the bonded region of the critical interface. The strain energy release rates (SERR) in all the three fracture modes are extracted, and two different phase angles are calculated using the below-given formulas to observe the interaction of different fracture modes.

The mode-mixity between Mode-II and Mode-I is defined by $\Psi_{II,I}$:

$$\Psi_{II,I} = \tan^{-1} \left(\sqrt{\frac{G_{II}}{G_I}} \right) \quad (3.30)$$

where G_I and G_{II} are the Mode-I and Mode-II strain energy release rates, respectively.

The mode-mixity between Mode-III and Mode-I is defined by $\Psi_{III,I}$:

$$\Psi_{III,I} = \tan^{-1} \left(\sqrt{\frac{G_{III}}{G_I}} \right) \quad (3.31)$$

where G_I and G_{III} are the Mode-I and Mode-III strain energy release rates, respectively.

Figure 3-31 presents the strain energy release rates in three modes at $\Delta t = 2 \mu s$ after the onset of delamination. The crack front extends approximately 6 mm along the width direction. The Mode-I strain energy-release rate is dominant among all the strain energy release rates. The delamination at the center of the specimen propagates under mode-mixity with the minor contribution of Mode-II at time $\Delta t = 2 \mu s$. Moreover, at the edges of the crack front, the propagation is again under mode-mixity with the minor contribution of Mode-III.

Phase angles, $\Psi(w)$, as a function of width at $\Delta t=2 \mu s$ are also given in Figure 3-31 to explain the mode-mixity along the width direction, clearly. $\Psi_{II,I}$ defines the mode-mixity between Mode-II and Mode-I as the phase angle of $\Psi_{II,I} \approx 90^\circ$ yields a pure Mode-II crack propagation. $\Psi_{III,I}$ defines the mode-mixity between Mode-III and Mode-I as the phase angle of $\Psi_{III,I} \approx 90^\circ$ yields a pure Mode-III crack propagation.

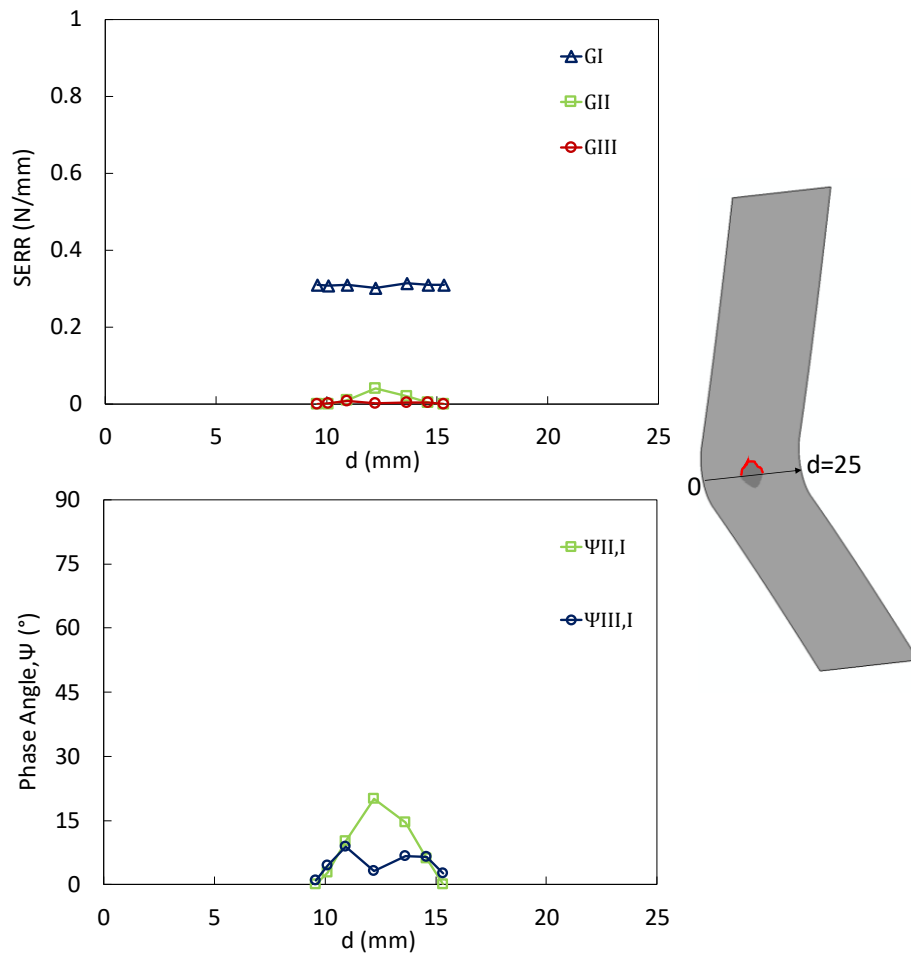


Figure 3-31. Strain energy release rates (SERR) and phase angles as a function of width at $\Delta t=2 \mu s$.

Strain energy release rate components at $\Delta t=7 \mu s$ are given in Figure 3-32. At this time instant, the length of the crack front is approximately 18 mm along the width direction. The Mode-II energy-release rate increases significantly at the center as the Mode-I energy-release rate decreases. The presence of the Mode-III energy-release rate becomes visible as shoulders approximately 3 mm away from the center. Phase angles, $\Psi(w)$, as a function of width at $\Delta t=7 \mu s$ are also given in Figure 3-32. The delamination at the center of the specimen propagates under mode-mixity with the major contribution of Mode-II and minor contribution of Mode-I at time $\Delta t = 7 \mu s$. Moreover, at the edges of the crack front, the propagation is again under mode-mixity with the minor contribution of Mode-III and the major contribution of Mode-I.

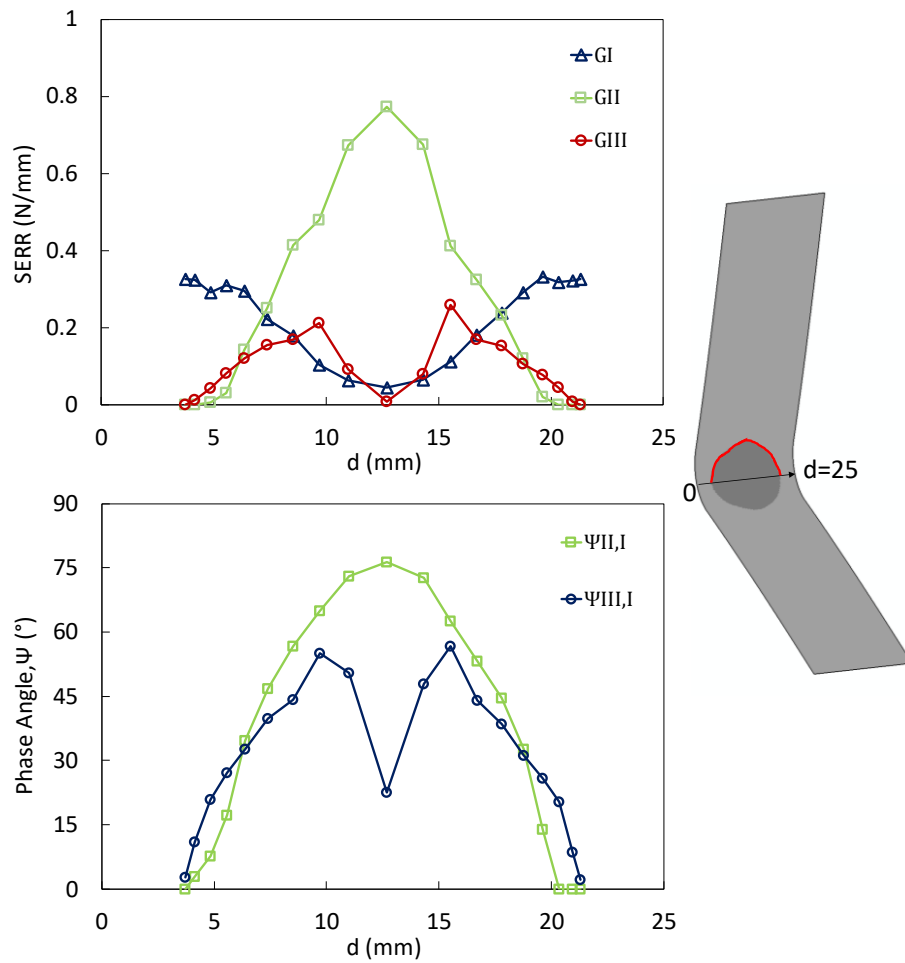


Figure 3-32. Strain energy release rates (SERR) and phase angles as a function of width at $\Delta t=7 \mu s$.

Figure 3-33 depicts the change of strain energy release rates across the width when the edge crack occurs at $\Delta t=11 \mu s$. At the center of the width, again Mode-II is dominant with a peak value of 0.562 N/mm. At the free edges, the Mode-III strain energy release rate increases significantly compared to previous time instants. Phase angles as a function of width at $\Delta t=11 \mu s$ are also given in Figure 3-33. All three of the fracture modes contribute to crack propagation along the crack front with different dominances. At the center of the width, again the dominant fracture mode is Mode-II and at the edges of the crack front Mode-I becomes dominant as Mode-II strain energy release rates decrease dramatically. The contribution of Mode-II to propagation at the

free edges is negligible compared to the other two modes, and the contribution of Mode-III to propagation at the center of the width is negligible.

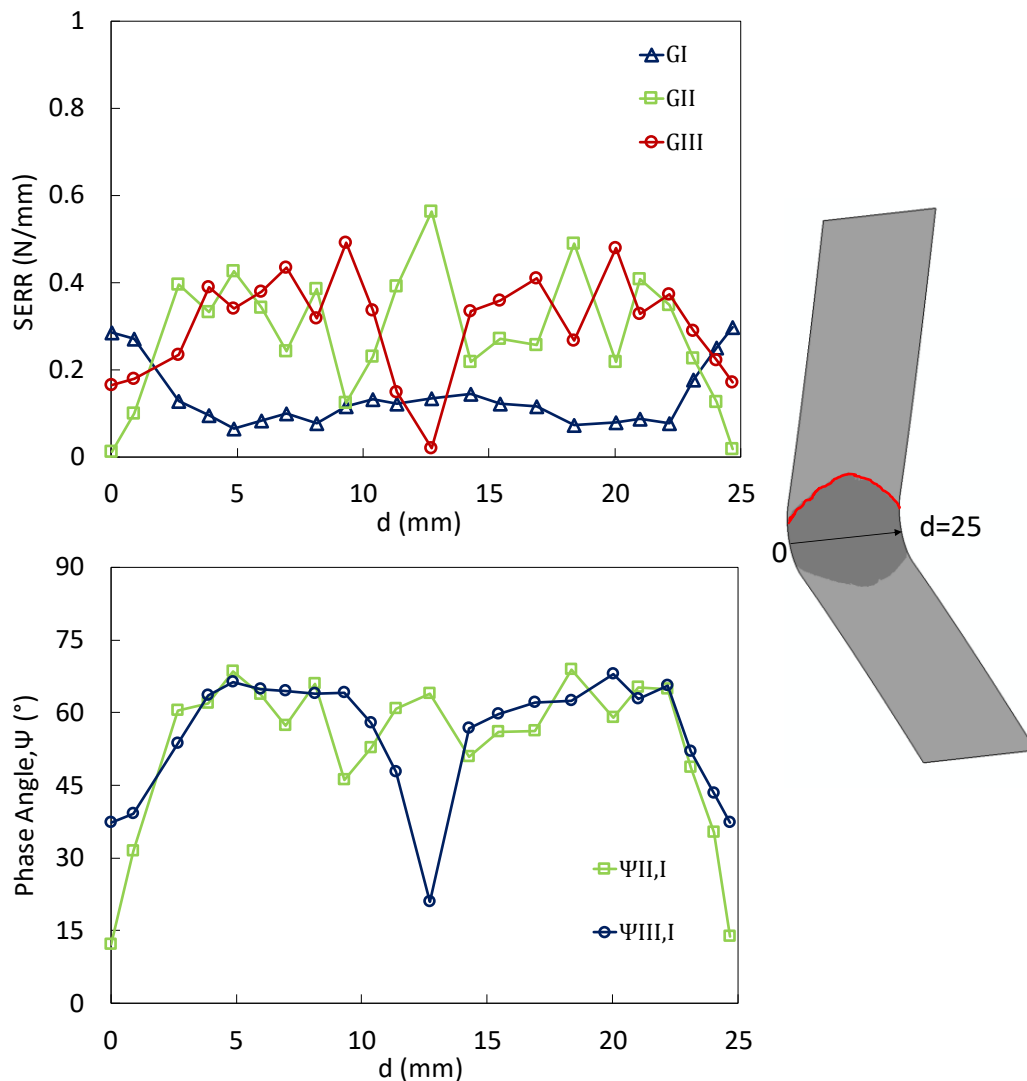


Figure 3-33. Strain energy release rates (SERR) and phase angles as a function of width at $\Delta t=11 \mu s$.

The strain energy release rates as a function of the width of the specimen at $\Delta t=13 \mu s$ are given in Figure 3-34. At this time instant, the edge crack passes to arm region under Mode-III dominance. The contribution of Mode-I to propagation at the free edge is negligible as the values are too small compared to other components. At the center of the width, again the dominance of Mode-II continues. Moreover, mode-mixities at $\Delta t=13 \mu s$ expressed by two phase-angles are given in Figure 3-34. The Mode-II

dominance is observed to drop significantly at the free edge. The change of phase angle, $\Psi_{III,I}$, along the width of the specimen shows that the effect of Mode-III at the free edge is more dominant.

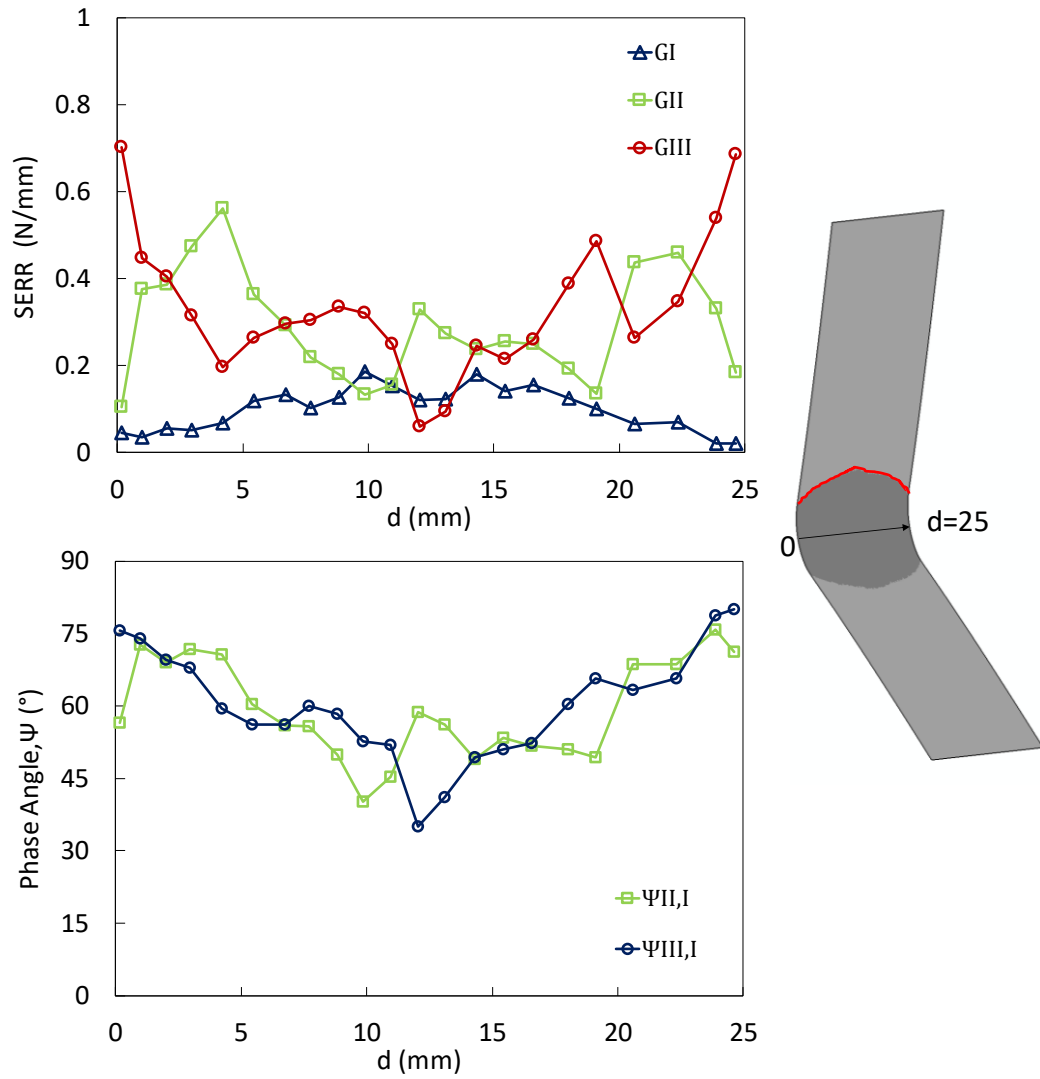


Figure 3-34. Strain energy release rates (SERR) and phase angles as a function of width at $\Delta t=13 \mu s$.

3.6. Discussion

The load-displacement response of curved unidirectional CFRP laminate under quasi-static moment-axial combined loading from the 2D (blue), and 3D (red) simulations are compared with the experimental results (grey) [1] in Figure 3-35. The load-displacement behavior is linear elastic until sudden dynamic failure, which occurs due to a single main delamination that extends to both arms from the curved region. The stiffness before failure in the experiments is captured very well by both 2D and 3D simulations. The peak load before crack initiation is almost identical for 2D and 3D models with 1380 N for 2D Plane strain FEA and 1330 N for the 3D FEA, which is within the scatter of the experiments.

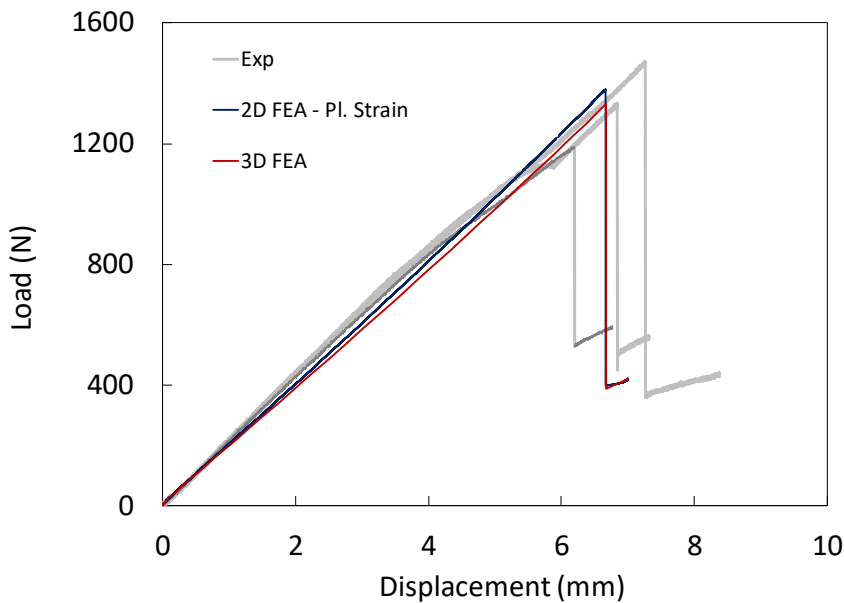


Figure 3-35. Load-displacement curves for curved UD CFRP laminate under quasi-static moment-axial combined loading from experiments [1] compared with 2D and 3D FEA simulations.

Under displacement-control, an almost instantaneous load drop occurs after peak load is attained in the simulations as with the experiments, where the load drops to 400 N. As the displacement is increased afterwards, the load increases with a much smaller slope, corresponding to the reduced stiffness of the curved beam.

In 2D FEA, the cohesive elements at the interface of the 12th and 13th layers are degraded and failed when the maximum radial stress reaches the value of interlaminar tensile strength. The stiffness degradation of the cohesive elements at the center-line in the thickness direction are shown in Figure 3-36. Moreover, radial stresses in thickness direction extracted from 2D FEA and calculated analytical stress values according to Lekhnitskii [5] are compared in Figure 3-36. As it can be seen from the Figure 3-36 the interface elements at the other interfaces are not degraded in the center-line of the curved region. This information is considered when modelling the 3D finite element model with only one interface.

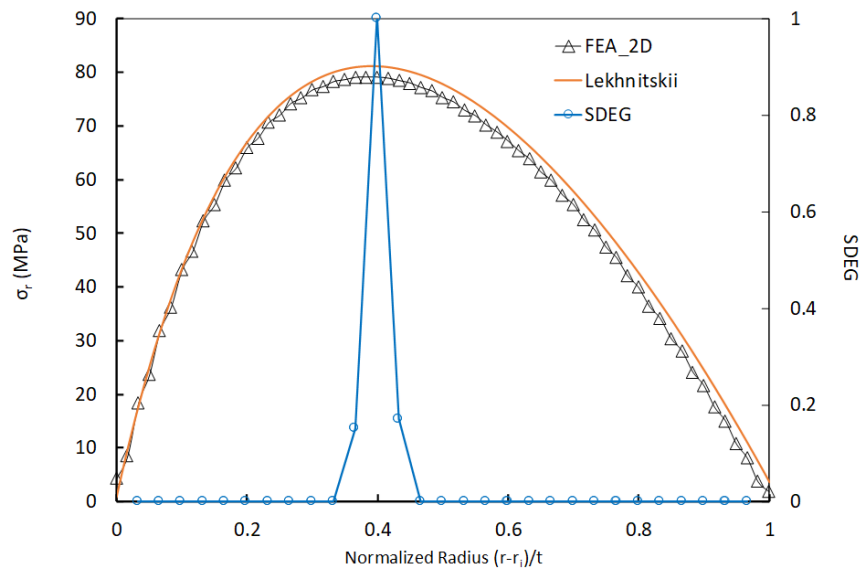


Figure 3-36. Radial stress distribution and stiffness degradation scalar (SDEG) of cohesive elements in the interfaces.

A qualitative comparison between experiments and 2D simulations are shown in Figure 3-37. The Tresca strain field just before failure and a camera picture after failure showing the location of the delamination is shown in Figure 3-37 (a). This is compared to a snapshot of the finite element contours of radial stresses before failure, and the delamination location after failure shown in Figure 3-37 (b) compares qualitatively well with the experiments.

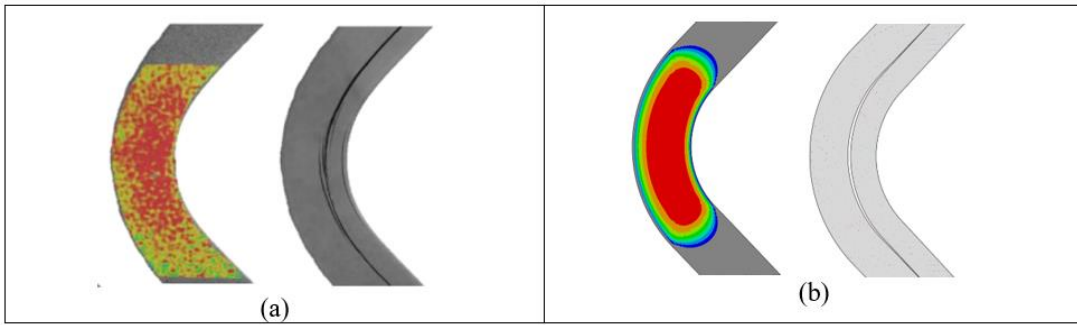


Figure 3-37. Qualitative comparison of experimental and finite element analyses results.

Crack tip speed as a function of the crack tip location from the center of the curved region for 2D crack tip and 3D crack tip at the center and the free edge are shown in Figure 3-38. The calculated crack tip speeds from 2D FEA is higher compare to center and edge crack throughout the analysis. In the arm region; center crack travels at intersonic speeds for 4 μ s, edge crack travels at intersonic speeds for 6 μ s, and 2D crack travels at intersonic speeds for 15 μ s.

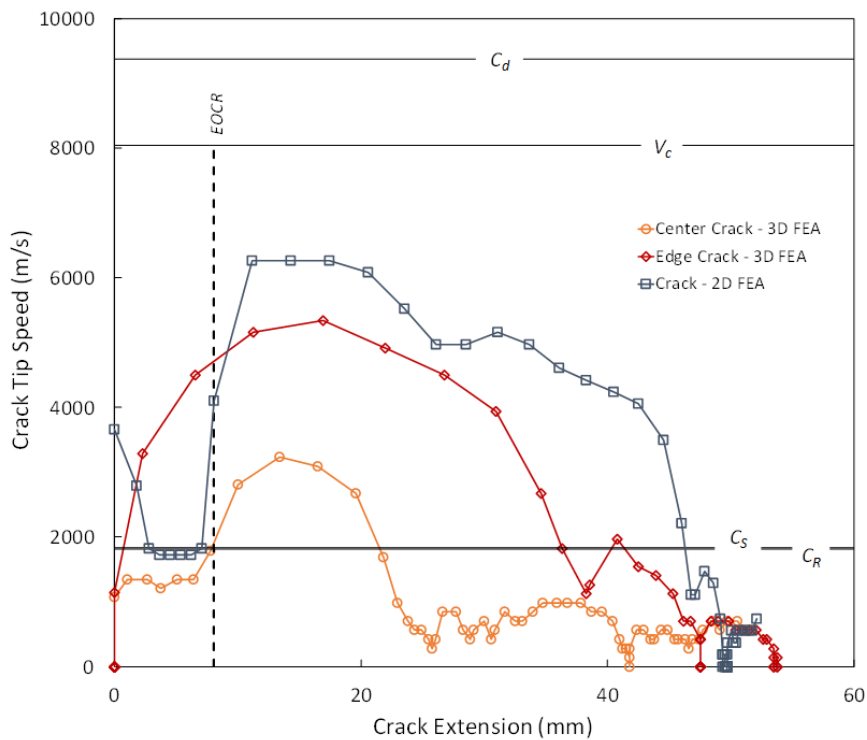


Figure 3-38. Crack tip speed as a function of the crack tip location from the center of the curved region for 2D crack tip, 3D crack tip at the center and at the edge.

In 2D finite element results, it is observed that the crack initiates with a speed value higher than the material shear wave speed which is not reasonable considering that a crack cannot exceed the Rayleigh wave speed of the material under Mode-I loading. In 3D finite element results; while the edge crack exceeds the Rayleigh wave speed of the material but in this case the crack is under mixed mode loading, the center crack travels with a speed less than Rayleigh wave speed in the curved region. In the curved region, center crack is mainly effected by Mode-I loading which is reasonable considering sub-Rayleigh wave speeds. The center crack propagates at intersonic speed for a crack length of 11 mm, and the edge crack propagates at intersonic speed for a crack length of 32 mm while the 2D crack develops at intersonic speed for 35 mm. As a result of these observations, it is clear that 2D crack and 3D edge crack show similar behavior.

3.7. Conclusions

2D and 3D explicit finite element analyses of dynamic delamination in curved UD CFRP laminate, $[0]_{30}$, were carried out under moment/axial combined loading in conjunction with cohesive zone elements. The following conclusions are drawn as a result of the 2D and 3D FE analyses:

- Load-displacement curves show good correlations with experimental results [1] in terms of stiffnesses before failure and major delamination location in thickness.
- 2D and 3D finite element analyses of dynamic delamination in curved CFRP laminates revealed that the crack propagation speeds inside the specimen varies as edge crack travels faster than center crack.
- Although delamination initiates at intersonic speeds under Mode-I condition in 2D FEA, it initiates at subsonic speeds under Mode-I condition in 3D FEA. This result shows that the 3D model predicts initiation speed of delamination more reasonably, since it is known that a crack under Mode-I dominancy cannot exceed the Rayleigh wave speed of the material.

- Stress contour varies inside the specimen and results obtained at the center section of the 3D model are more consistent with 2D plane strain results.
- As the crack passes to arm region, it travels in Mode-II dominance with intersonic speed. Shear Mach waves radiating from the crack tip are observed clearly as a result of both 2D and 3D simulations.
- The 2D crack and the 3D edge crack show similar behavior in terms of crack tip speeds.
- In 3D FE results, the effect of Mode-III on delamination propagation is observed clearly dominantly at the free edges.

CHAPTER 4

FABRIC LAMINATE

In this chapter, 2D and 3D FE analyses of dynamic delamination in fabric laminate are presented in detail. First, information about the generation of finite element models is given and then results are presented for both 2D and 3D finite element analyses, respectively.

4.1. Material

Mechanical and interface properties of AS4/8552 5HS fabric are provided in Table 4.1 and Table 4.2. The mechanical properties are taken from the material specification datasheet [41]. The average of compressive and tensile measured mean values is taken in order to obtain modulus values in warp and weft directions. Interlaminar normal and shear strengths are taken as $t_1^0 = 53$ MPa and $t_1^0 = 79$ MPa by considering the values of [42] and experimental results of curved fabric laminate [1]. Moreover, fracture toughness values for each mode are taken from [38].

Table 4.1. Material properties of HexPly AS4/8552 5 HS fabric.

Density	1570 kg/m ³
Cured Ply Thickness	0.280 mm
Elastic Properties	$E_{11}= E_{22}=64000$ MPa; $E_{33}=8500$ MPa; $\nu_{12}=0.046$; $\nu_{13}= \nu_{23}=0.30$ $G_{12} =4900$ MPa; $G_{13}=G_{23}=3700$ MPa;

Table 4.2. Interface properties of HexPly AS4/8552 5 HS fabric.

Interface Strength	$t_I^0 = 53 \text{ MPa};$
	$t_{II}^0 = t_{III}^0 = 79 \text{ MPa}$
Fracture Toughness	$G_{I,C}=0.3753 \text{ N/mm};$
	$G_{II,C} = G_{III,C} = 1.4671 \text{ N/mm}$
B-K Criterion Constant (η)	2.25
Interface Stiffness	$K=1.0 \times 10^6 \text{ N/mm}^3$

The dilatational, shear, and Rayleigh wave speeds of the fabric material are calculated using the formulas provided in Section 3.1.

Table 4.3. Material wave speeds for HexPly AS4/8552 5 HS fabric.

	$c_I^{\parallel} \text{ (m/s)}$	$c_I^{\perp} \text{ (m/s)}$	$c_S \text{ (m/s)}$	$c_R \text{ (m/s)}$	$v_C \text{ (m/s)}$
Plane-stress	6391	6391	1767	1761	6243
Plane-strain	6434	6434	1767	1761	6243

4.2. Geometry and Boundary Conditions

Both 2D and 3D finite element models corresponding to the experimental configuration [1] of the curved fabric CFRP laminate are developed. The geometrical properties of the considered fabric specimen are illustrated in Figure 4-1. The upper and lower arm length (l) of the considered specimen is 66.94 mm. Inner radius (r_i) and width (w) of the specimen are 8.0 mm and 25 mm, respectively.

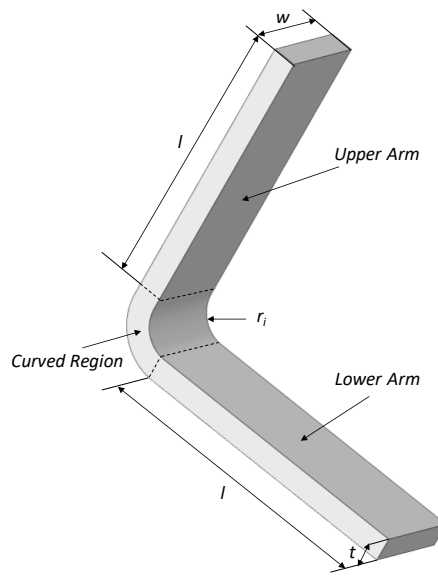


Figure 4-1. Specimen geometry for the curved fabric CFRP laminate.

The fabric laminate is composed of 18 fabric plies of CFRP with a ply thickness of 0.28 mm which corresponds to 5.04 mm total thickness. The stacking sequence of the fabric laminate is $[(45/0)_7, 45/45/0/45]$ as shown below in Figure 4-2.

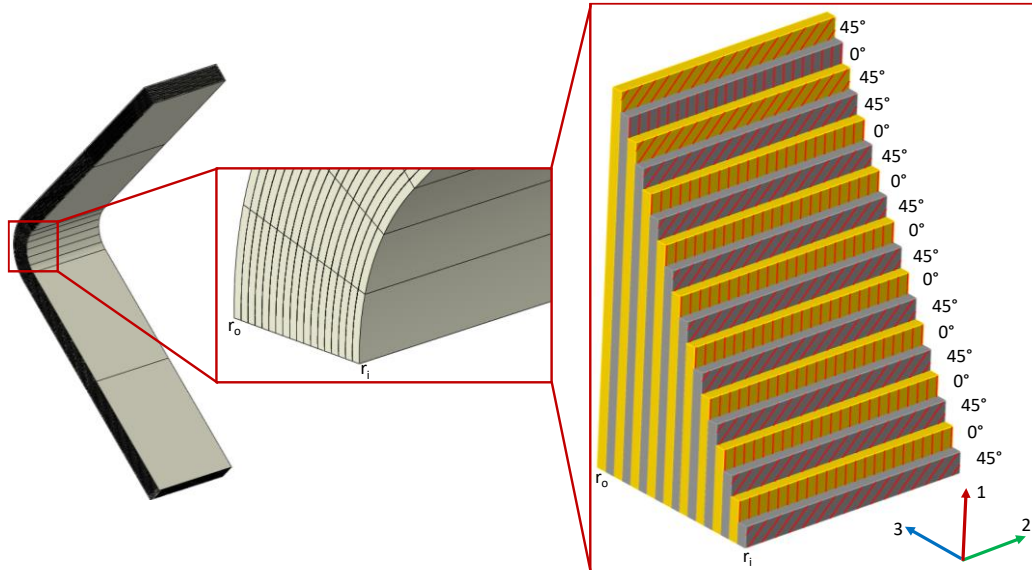


Figure 4-2. Stacking sequence of the curved fabric laminate.

Boundary conditions are the same as defined for the curved UD CFRP laminate in Section 3.3 except for the maximum applied displacement. Prescribed maximum

displacement is set to 16 mm, and it is applied to the specimen by a smooth step amplitude as defined in Eqn. (3.28). The loading profile of the smooth step for quasi-static simulation of curved fabric laminate is depicted in Figure 4-3. A total of 16 mm displacement is applied in 16 ms which corresponds to an average loading rate of 1 m/s.

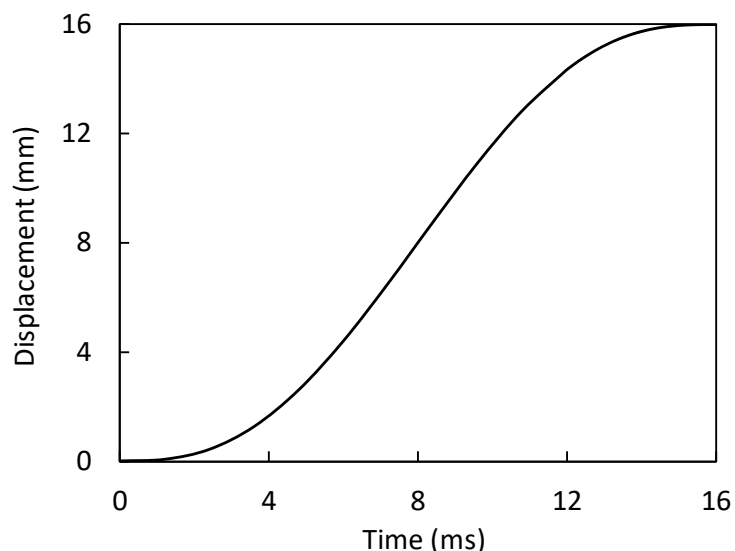


Figure 4-3. Loading profile of smooth step for quasi-static simulation of curved fabric laminate.

4.3. Finite Element Modelling

4.3.1. 2D FEM

In the two-dimensional FE model of the curved fabric CFRP laminate, each layer is discretized with two 4-node bilinear reduced integration elements (CPE4R) through the thickness. Two-dimensional cohesive elements (COH2D4) available in ABAQUS/Explicit element library are employed to model all of the seventeen interfaces. The thickness of the cohesive elements at each interface are taken to be $t=0.001$ mm. The enhanced hourglass control approach is used for bulk material representation to prevent hourglassing of the reduced integration elements. The penalty stiffness (E_0) is calculated as 1.0×10^6 N/mm³ by using Eqn. (2.11), and the exponent of the B-K law is specified as 2.25. The sweep mesh technique is used to

correctly align cohesive elements at the layer interfaces like the FE model of the curved UD CFRP laminate. The mesh density used in the 2D FE model of the curved UD CFRP laminate is also preferred for the 2D FE model of the curved fabric laminate. Magnified view of the mesh at the center-line is shown, and element dimensions in this region are given in Figure 4-4. The element height changes from $84\ \mu\text{m}$ to $137\ \mu\text{m}$ due to the curved region and element width, $w_e=140\ \mu\text{m}$, is constant through the thickness direction.

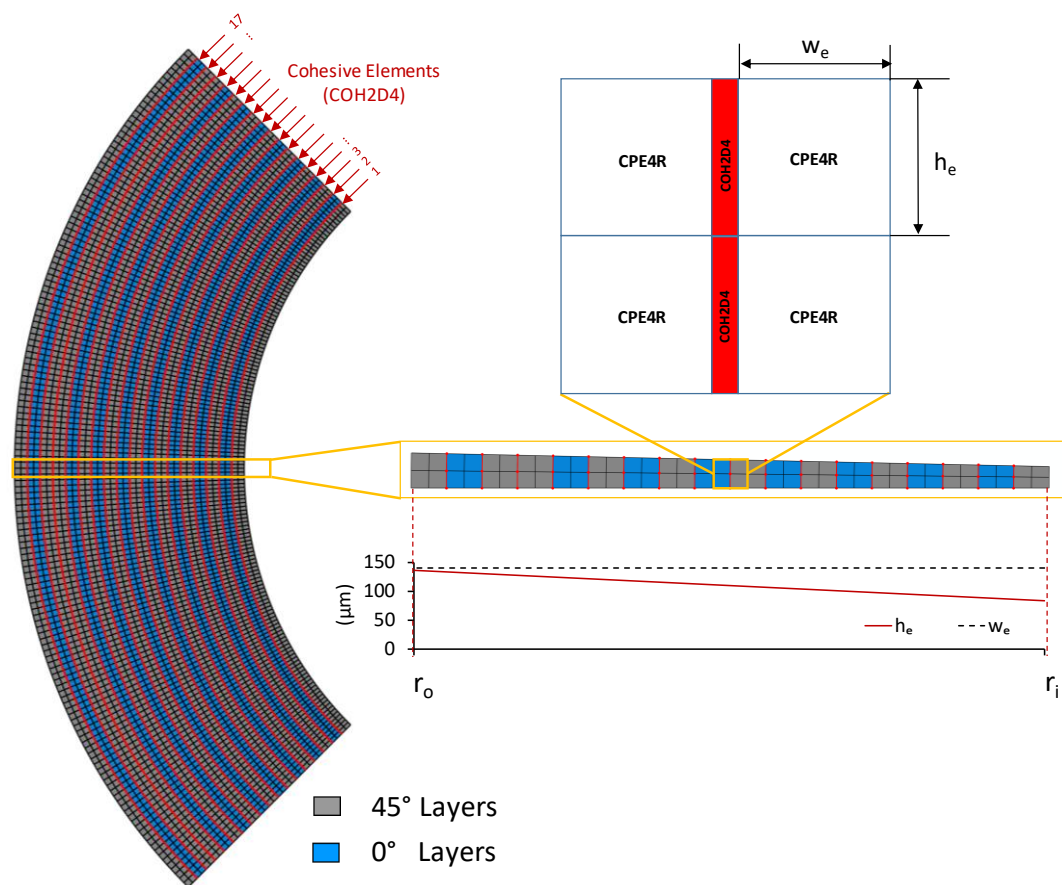


Figure 4-4. Magnified view of the mesh at the center line of the 2D FEM of fabric laminate and details of interface modelling.

The two-dimensional finite element model of the fabric laminate includes 31320 first-order quad elements of type CPE4R and 14790 first-order quad elements of type COH2D4. The total number of elements is 46110. Moreover, the total number of nodes is 47036 which corresponds to 94182 number of degrees of freedom. ABAQUS

calculates the stable time increment as 2.882×10^{-10} s. The analysis was performed on a high-performance cluster consisting of 72 CPU cores. A single simulation takes more than 21 hrs. Contact interactions in normal and tangential directions are defined between the adjacent layers to prevent penetration of layers under large values of prescribed displacements.

4.3.2. 3D FEM

In the three-dimensional FE model of the fabric laminate, the bulk region is discretized by reduced integration continuum solid elements which are denoted as C3D8R in ABAQUS/Explicit element library. Like the two-dimensional FE model, the three-dimensional FE model includes all the interfaces since the stacking sequence is complicated compared to UD laminate. The main reason for modelling all the interfaces in the 3D FE model is the mismatch of the material properties at the free edge where the delamination onset is expected due to stress singularities at the interfaces of differently oriented layers. The mesh density of the 3D FE model differs from the 2D FE model due to computational efficiency. Using the same mesh density of the 2D FE model would result in more than 7 million elements which require excessive CPU time and RAM.

Mesh density and interface modelling details of the 3D FE model of the curved fabric laminate are shown in Figure 4-5. In order to have an appropriate computational time, each solid layer is discretized with only one element in the thickness direction. Around the curve region, there are two elements per three degrees sweep and in the width direction there are 90 elements. The 3D FE model of the curved fabric laminate includes 874800 first-order hexahedral elements of type C3D8R and 826200 first-order hexahedral elements of type COH3D8. The total number of elements is 1701000. Moreover, and the total number of nodes is 1772316 with 5336616 numbers of degrees of freedom. ABAQUS calculates the stable time increment as 2.517×10^{-8} s. The analysis was performed on a high-performance cluster consisting of 72 CPU cores. A single simulation takes around more than 139 hrs. As mentioned in the section

on 2D FE modelling, contact interactions in normal and tangential directions are also considered for 3D FE models between the adjacent layers with the General Contact Algorithm of ABAQUS to prevent layer interpenetration.

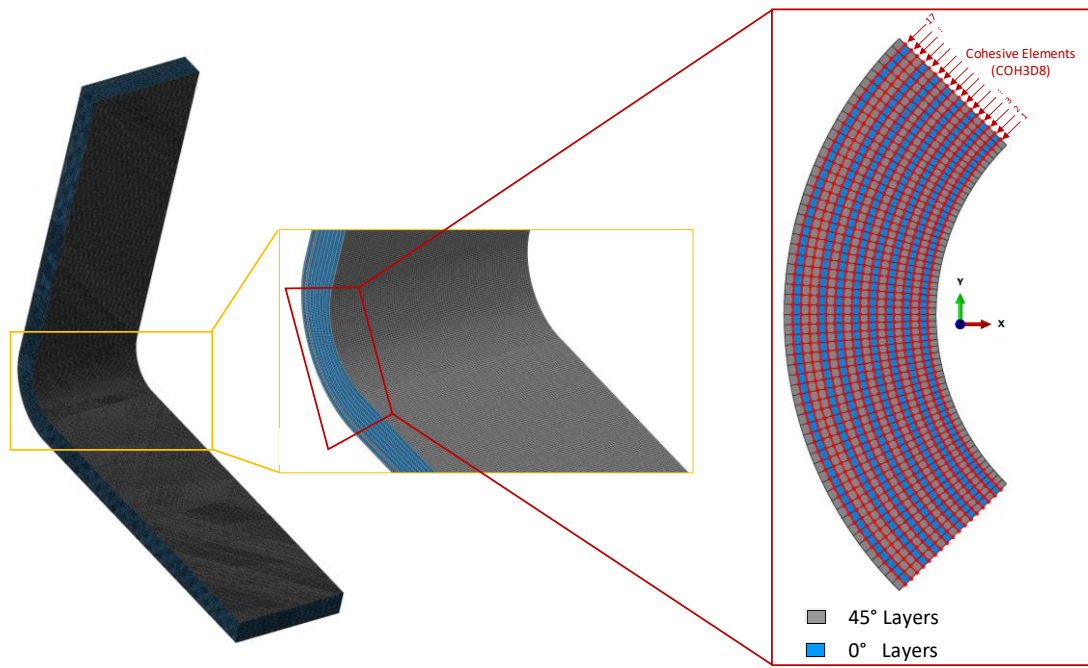


Figure 4-5. 3D FEM details of fabric laminate in terms of interface modelling and mesh density.

4.4. Results

4.4.1. 2D FEA Results

When the defined damage variable of the cohesive element reaches the value of one, which means failure of the considered element at that time instant, excessive oscillations occur on the load-displacement curve due to wave propagations and reflections at specimen boundaries in such a small time increment (stable time increment in explicit analysis in the order of $10^{-8} - 10^{-9}$). In order to eliminate these high-frequency noises in the load-displacement curve, noise filters such as Butterworth or Chebyshev filters can be used, or the step time can be increased. The former approach cannot show the sharp load drop, and the latter needs long computational time which is unreasonable. A sequential analysis proposed by

Gozluklu and Coker [16] can be used which includes the continuation of an implicit analysis by explicit analysis. However, this approach requires a transition from implicit to explicit analysis which requires re-run of the finite element model and post-processing. In this study, another technique is proposed which is to filter the high-frequency noise on the load-displacement curve by examining the history of various energy components extracted during the simulations.

History plots of the strain and fracture energies for the 2D Plane Strain FE model of the curved fabric CFRP laminate appears as shown in Figure 4-6.

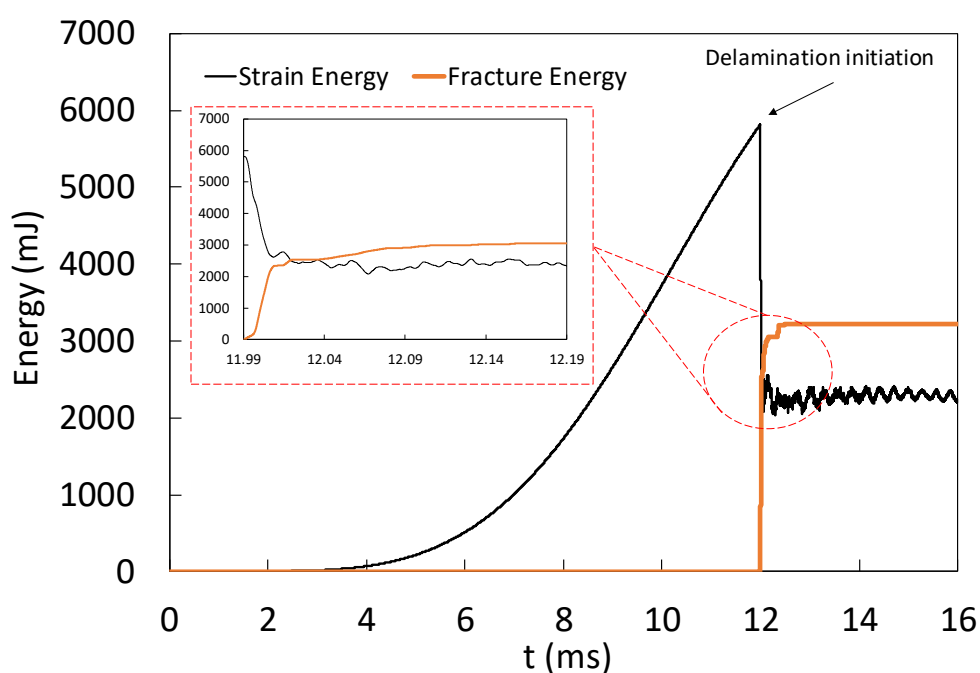


Figure 4-6. Strain and fracture energy history for 2D plane strain analysis of curved fabric CFRP laminate.

Fracture energy remains zero until the damage initiation point, which corresponds to $t = 11.9916$ ms. As the damage occurs and propagates, the energy dissipated during the failure of interface elements increases instantaneously. The same instantaneous change is seen in the strain energy as a decrease. Both the sudden drop in strain energy and sudden increase in fracture energy clearly indicates the time point of the delamination initiation. The end of the instantaneous increase or instantaneous decrease is attributed as the end of the load drop in the load-displacement curve. By

knowing the damage initiation and end of the instantaneous load drop, a line is fitted to high-frequency noise and a filtered load-displacement curve is attained as done for curved UD CFRP laminate.

The kinetic and total strain (internal) energy histories are presented in Figure 4-7. At $t=11.9916$ ms, total strain energy decreases suddenly and the kinetic energy increases in the same manner. Both kinetic and total strain energy oscillate significantly as the delamination propagates through the arms. Comparison of the kinetic and total strain (internal) energy history shows that the kinetic energy is small relative to the internal energy throughout the analysis. The criterion for quasi-static loading that kinetic energy must be small relative to total strain energy has been satisfied, even for the severe increase during the delamination onset.

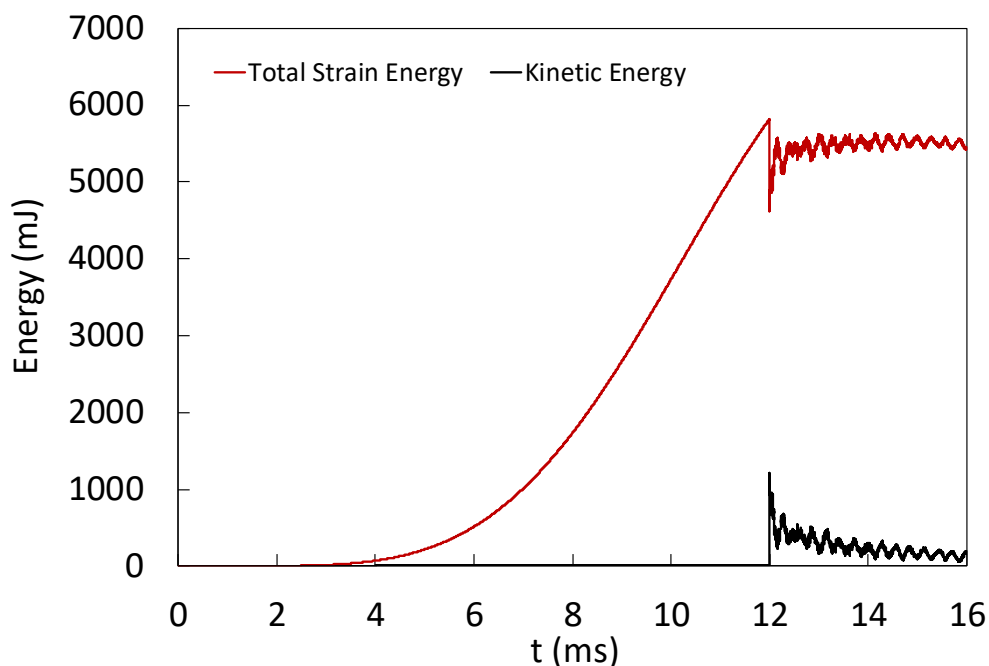


Figure 4-7. Internal and kinetic energy history for 2D plane strain analysis of curved fabric CFRP laminate.

The load-displacement response of curved fabric CFRP laminate from the 2D FEA is shown on the left-hand side of the Figure 4-8 with grey color. The load-displacement data (grey) is filtered in order to eliminate high-frequency noise, which occurs mainly due to the reflection of stress waves at the material boundaries after the failure of the

interface elements. Both filtered and unfiltered curves show linear elastic behavior until the failure load of 850 N. After the peak load (Point a), the interface elements degrade completely and a sudden dynamic failure occurs which extends to both arms from the curved region. The stiffness of the fabric laminate before failure is 59.32 N/mm, which shows good agreement with the experimental results. The delamination reaches the arm region in 4.7 μ s and causes a 170 N reduction in load-carrying capacity of the intact fabric laminate (Point b). The total load drop occurs in 17 μ s when the crack extends for 36.464 mm (Point c). The length of the crack at the arm region at “Point c” corresponds to 42% of the arm length. Finally, the simulation is completed as the maximum applied displacement value is reached. The final deformed shape of the curved fabric CFRP laminate is shown in Figure 4-8 (Point d). The second stiffness is calculated to be 21.1 N/mm which agrees well with the averaged experimental second stiffness (19.5 N/mm).

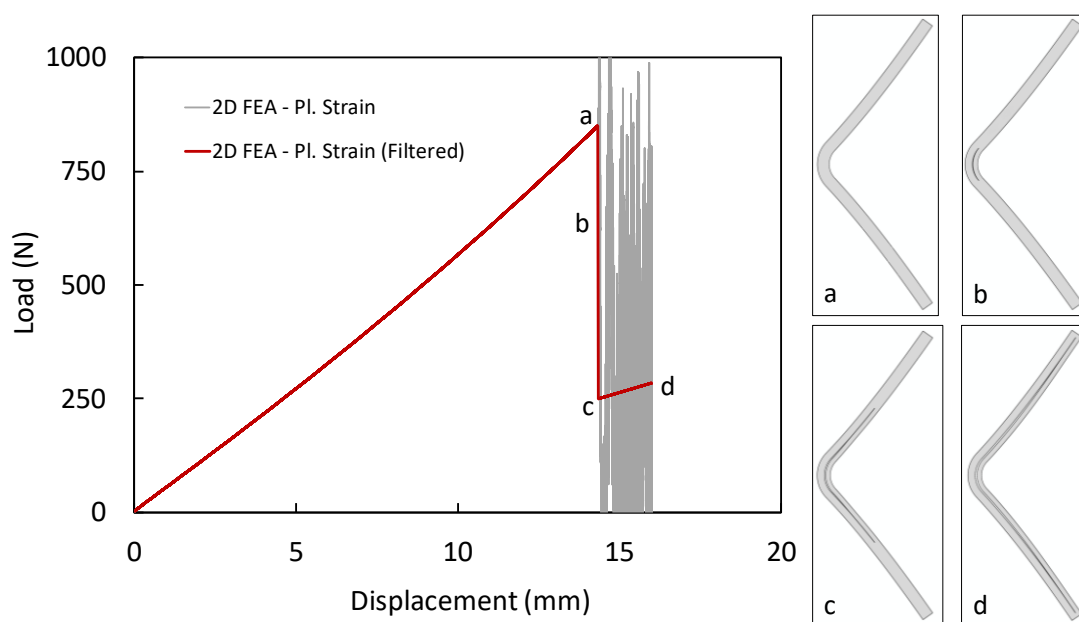


Figure 4-8. Load – displacement curve for 2D FEA of curved fabric CFRP laminate.

Evolution of the opening stress, σ_{33} , contours in the curved region of fabric CFRP laminate before and after failure are shown in Figure 4-9. Although the simulations are performed for the whole geometry, only the upper part is plotted here for

visualization since the results are symmetric according to the mid-line. Continuous radial stress distribution at the curved region is disrupted as the damage variable of the interface elements reaches 0.999 at $0.8 \mu\text{s}$ before delamination initiation. Delamination initiates when the applied displacement reaches 14.34 mm (850 N) at $t=0.0119915 \text{ s}$. This time is considered as t_0 from now on. After delamination initiation, due to high radial stresses shown by red color, it propagates dynamically to the arm region after the last frame at $4.7 \mu\text{s}$. The speed of the crack tip can be inferred from the concentration of stress distribution at the crack tip showing that the crack tip travels at very fast speed in the beginning and slowing down at the arm. The stress concentration in front of the crack tip also decreases as the crack slows down.

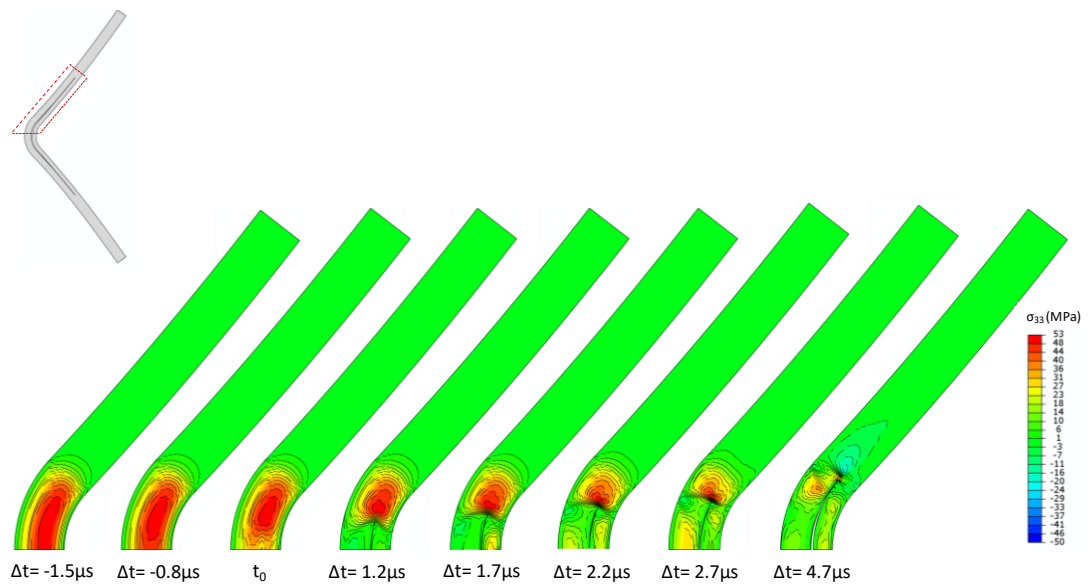


Figure 4-9. Evolution of the opening stress contours in the curved region of fabric CFRP laminate before and after delamination onset.

The contours of normal stress in the upper arm region at four different time instances are shown in Figure 4-10. Shear Mach waves radiating from the crack tip in the shape of inclined normal stresses are pointed out by red lines. Other inclined stress waves behind the shear Mach wave front can be attributed to the reflections of the waves from the free surfaces of the specimen. Local hot spots of stress concentrations are observed on the sliding crack surfaces due to elastodynamic waves.

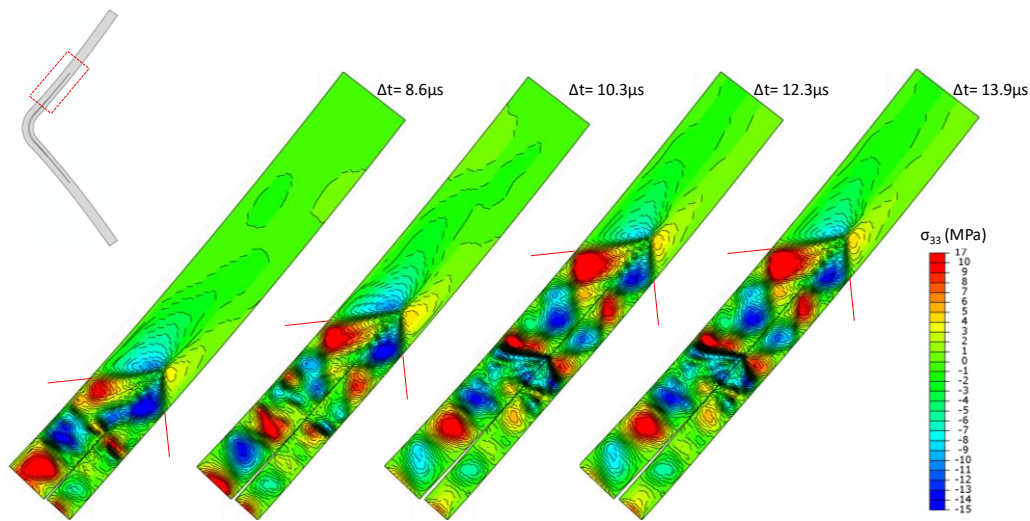


Figure 4-10. Shear Mach waves radiated from the crack tip and reflecting waves behind the crack tip for four time instances for curved fabric CFRP laminate.

The crack length is determined by using snapshots at different time instants, and the crack tip speed is calculated from the derivative of the crack length using moving three-point quadratic line fit for 2D simulations of curved fabric CFRP laminate. Crack extension and crack tip speed as a function of time are plotted in Figure 4-11. Delamination initiates intersonically at the 7th interface of the eighteen-layer curved fabric laminate and decelerates to sub-Rayleigh speeds as it propagates to the arms. At $\Delta t=4.7 \mu\text{s}$, the delamination passes to arm region with an approximate speed of 1100 m/s. After passing to the arm region, the delamination accelerates to a peak speed value of 3533 m/s in 2.8 μs . In the arm region, the delamination travels in intersonic speeds for 7.5 μs which corresponds to 21.94 mm crack length. After $\Delta t=14.5 \mu\text{s}$, crack decelerates to sub-Rayleigh speeds and stops at $\Delta t=20 \mu\text{s}$ for one μs . Although crack tip speed reaches approximately 1000 m/s for several time instants, it arrests after $\Delta t=28 \mu\text{s}$. A total of 41.85 mm crack length is reached during the propagation of the crack, the majority of which attained during intersonic propagation.

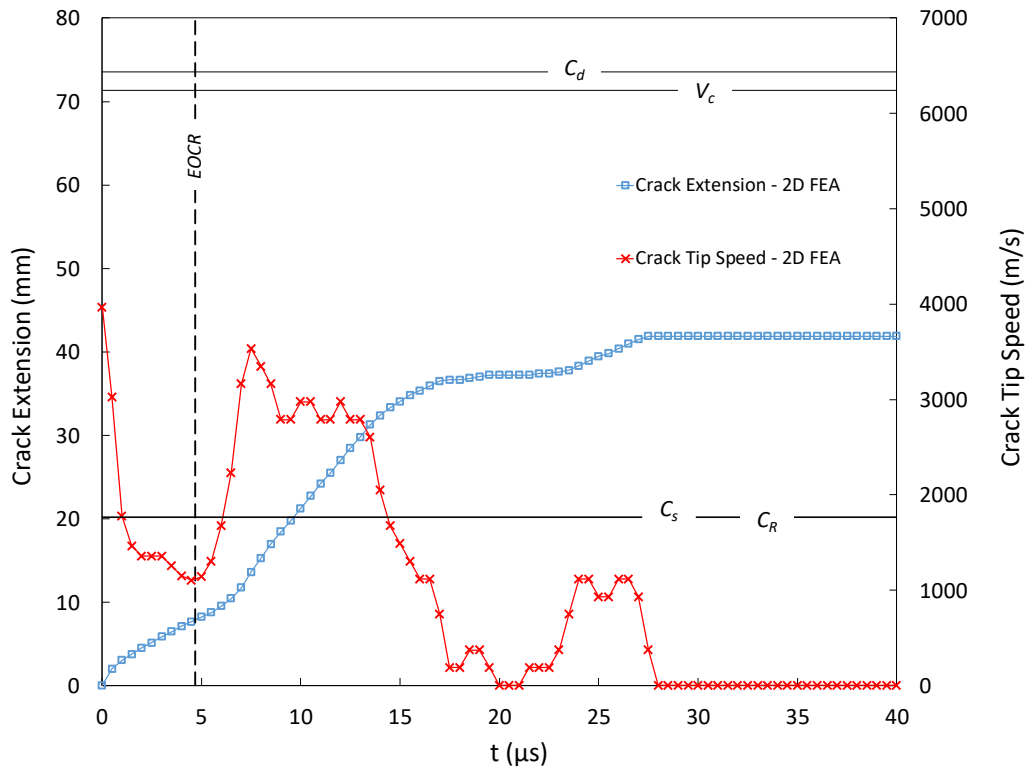


Figure 4-11. Crack tip speed as a function of time and crack extension for 2D FEA of curved fabric CFRP laminate.

4.4.2. 3D FEA Results

The oscillations on the load-displacement curve of 3D FEA of the curved fabric laminate are filtered by examining the history of strain and fracture energy extracted during the simulations as previously done in 2D FEA.

History plots of the strain and fracture energies for the 3D FE model of the curved fabric CFRP laminate appears, as shown in Figure 4-12. Fracture energy remains zero until the sudden increase at $t = 13.069$ ms. As the damage occurs and propagates, the fracture energy dissipated during the failure of interface elements increases instantaneously. The end of the instantaneous increase or instantaneous decrease is attributed as the end of the load drop in the load-displacement curve. By knowing the damage initiation and end of the instantaneous load drop, a line is fitted to high-frequency noise and filtered load-displacement curve is attained.

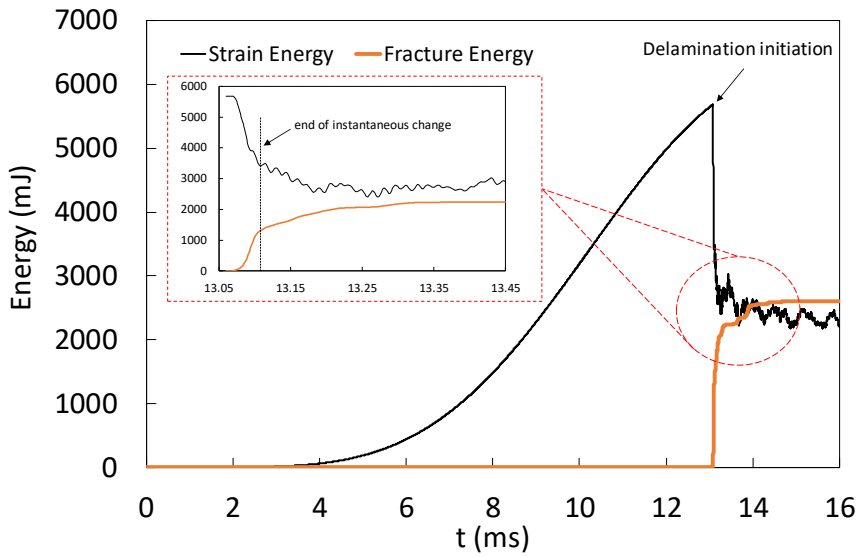


Figure 4-12. Strain and fracture energy history for 3D FEA of curved fabric CFRP laminate.

The kinetic and total strain (internal) energy history are presented in Figure 4-13. At $t = 13.069$ ms, total strain energy decreases suddenly and the kinetic energy increases in the same manner. Both kinetic and total strain energy oscillate significantly as the delamination propagates through the arms.

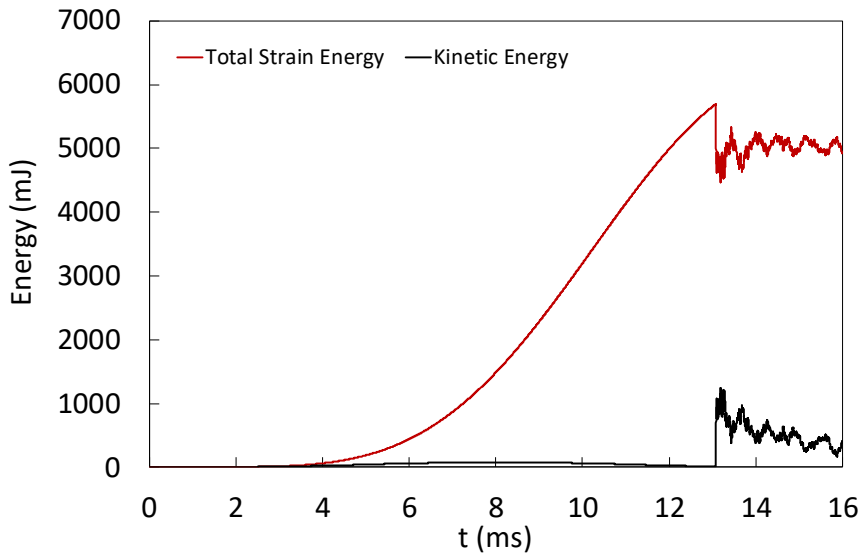


Figure 4-13. Internal and kinetic energy history for 3D FEA of curved fabric CFRP laminate.

Comparison of the kinetic and total strain (internal) energy history shows that the kinetic energy is small relative to the internal energy throughout the analysis. The criterion for quasi-static loading that kinetic energy must be small relative to total strain energy has been satisfied, even for the severe increase during the delamination onset.

The load-displacement response of curved fabric CFRP laminate from the 3D FEA is shown in the left hand side of the Figure 4-14 with grey color.

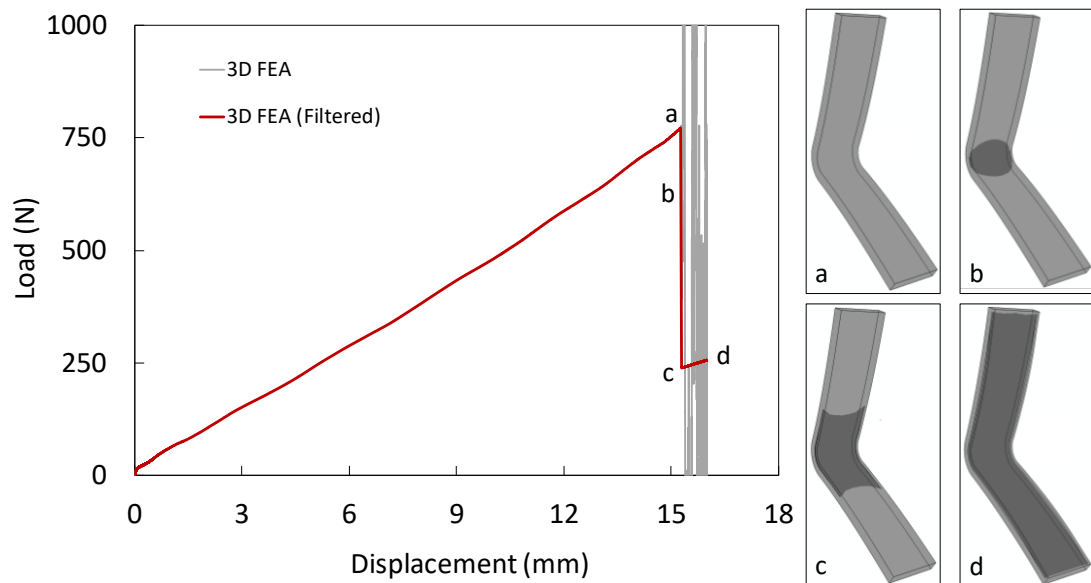


Figure 4-14. Load – displacement curve for 3D FEA of curved fabric CFRP laminate.

The load-displacement data (grey) is filtered in order to eliminate high frequency noise which occurs mainly due to moving stress waves after failure of interface elements. Both filtered and unfiltered curves show linear elastic behavior until the failure load of 772 N. After the peak load (Point a), the interface elements at the 6th interface degrade completely and a sudden dynamic failure occurs which extends to both arms from the curved region. The stiffness of the fabric laminate before failure is 50.56 N/mm. The delamination at the free edge reaches the arm region in 17 μ s and causes a 227 N reduction in load carrying capacity of the intact fabric laminate (Point b). The total load drop occurs in 40 μ s when the edge crack extends for 26.83 mm and center

crack extends for 22.39 mm (Point c). The length of the crack at the arm region at “Point c” corresponds to 28% of the arm length. Finally, the simulation is completed as the maximum applied displacement value is reached. The final deformed shape of the curved fabric CFRP laminate is shown in Figure 4-14 (Point d). The second stiffness is calculated to be 24.84 N/mm.

Delamination onset and growth inside the curved fabric specimen can be clearly seen in Figure 4-15 where the delamination region for each time frame is colored as dark grey.

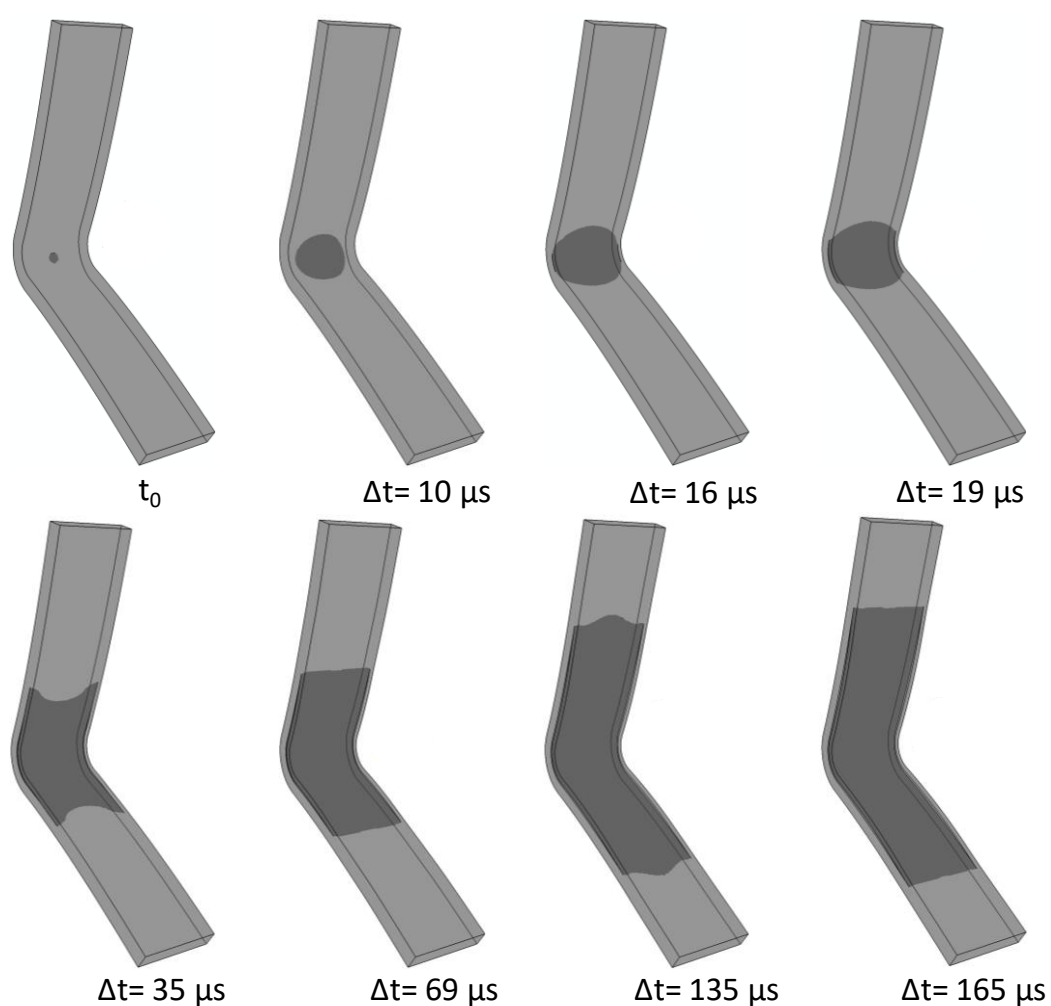


Figure 4-15. Delamination initiation and propagation path inside the curved fabric CFRP laminate.

The delamination initiates exactly at the center of the width of the specimen. Then it propagates in two directions; into the arm region and towards the free edge of the specimen. The crack tip speed in the width direction is calculated to be sub-Rayleigh and is not inspected in detail. Since the crack front is almost symmetric in both directions that crack propagates, only one half of the delamination front is investigated in detail by considering one crack tip at the center and one crack tip at the free edge. As illustrated in Figure 4-15, center crack is initially faster than the edge crack, but as soon as the edge crack reaches to the free-edge it reaches a peak speed of 2637 m/s, catching up and passing the center crack. Afterwards, since there is not sufficient energy for intersonic crack propagation, both edge crack tip and center crack tip propagate at sub-Rayleigh wave speeds to the end of the loading.

The center crack extension and tip speeds as a function of time are plotted in Figure 4-16 for the curved fabric CFRP laminate.

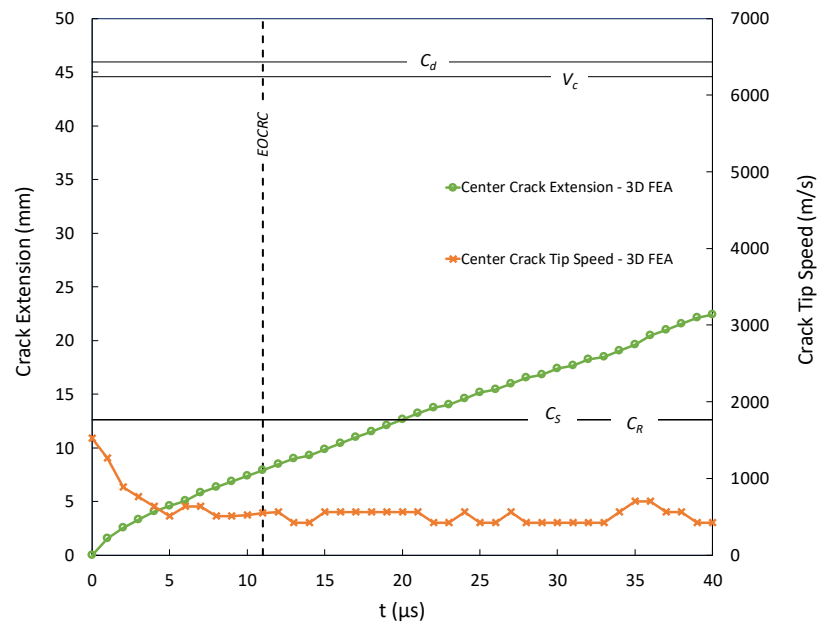


Figure 4-16. Center crack tip speed as a function of time and crack extension for 3D FEA of curved fabric CFRP laminate.

Center crack initiates with a sub-Rayleigh speed of 1700 m/s. As the center crack propagates through arms, it slows down to 550 m/s. After passing to the arm region,

the center crack propagates almost at a constant speed of 500 m/s. During the propagation stage of the center crack, it develops to a crack length of 22 mm in 40 μ s.

Variation of the edge crack tip speed and crack extension with respect to time are presented in Figure 4-17 for 3D FEA of curved fabric CFRP laminate. The initial time is taken to be the time at which the peak load is attained, which also corresponds to the initiation of delamination at the center of the width of the specimen.

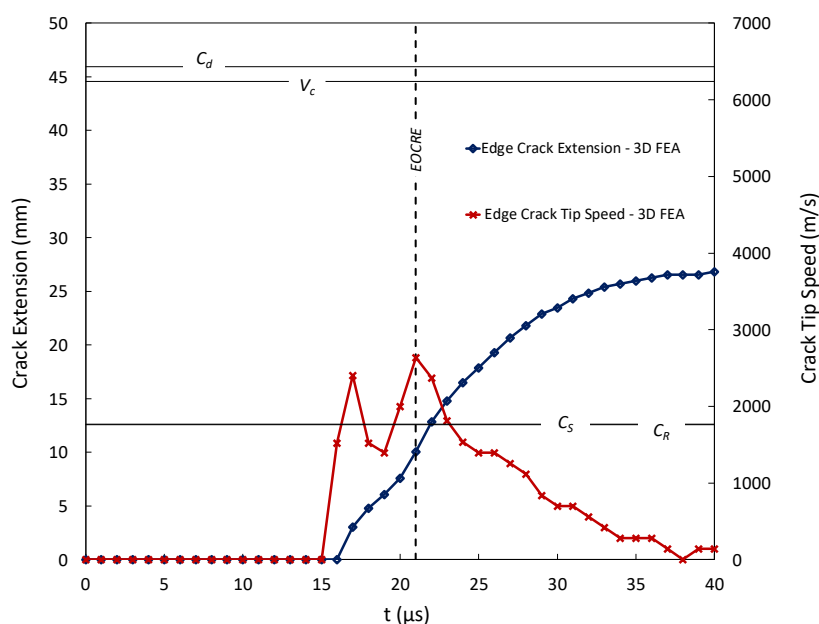


Figure 4-17. Edge crack tip speed as a function of time and crack extension for 3D FEA of curved fabric CFRP laminate.

The edge crack in the fabric laminate initiates 16 μ s after peak load and attains an intersonic speed value of 2407 m/s in 2 μ s. Then it decreases to sub-Rayleigh wave speed of approximately 1700 m/s for 2 μ . However, it immediately increases to a maximum crack tip speed of 2700 m/s at the end of the curved region (EOCR). Afterwards, at the arm region the crack gradually slows down to zero crack tip speed in 13 μ s. During the propagation stage, edge crack gains a crack length of 26 mm in 40 μ s with traveling at intersonic speeds for five μ s through all failure process. Unlike center crack, edge crack sustains speed values above shear wave speed during the propagation stage.

4.5. Discussion

The load-displacement response of curved fabric CFRP laminate under quasi-static moment-axial combined loading from the 2D (blue), and 3D (red and black) simulation is compared with the experimental results (grey) [1] in Figure 4-18. The load-displacement behaviour is linear elastic until sudden dynamic failure, which occurs due to a single main delamination that extends to both arms from the curved region. The stiffness before failure in the experiments is captured very well by 2D simulation but not with 3D (red) simulation. The peak load before crack initiation is 850 N for 2D plane strain and 771 N for 3D FEA, respectively.

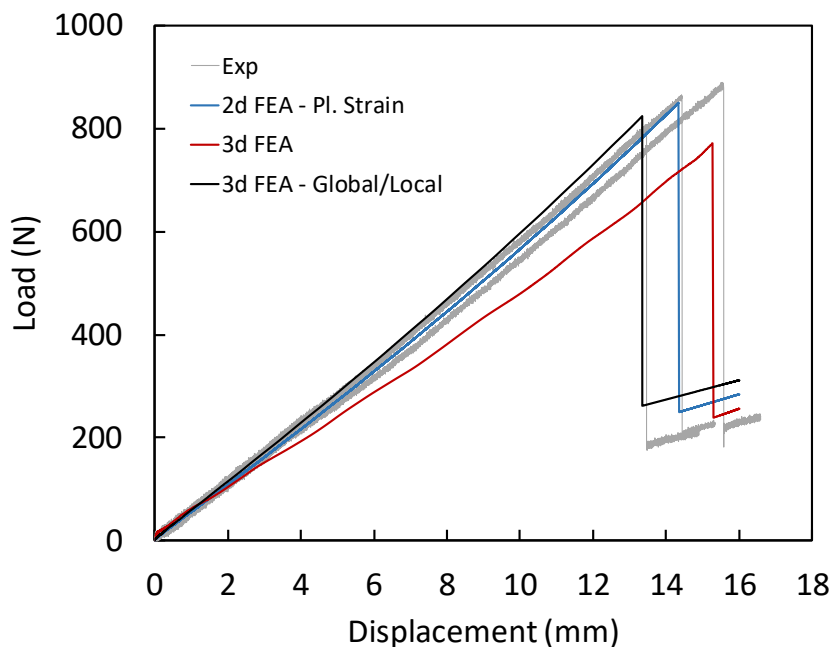


Figure 4-18. Load-displacement curves for curved fabric laminate under quasi-static moment-axial combined loading from experiments [1] compared with 2D and 3D FEA simulations.

The peak load and stiffness before the failure of the 3D FEA is not consistent with the 2D FEA and experimental results. The main reason for this nonconformity can be attributed to the modelling of each layer with a single reduced integration solid element. In order to attain a reasonable computational time, better stiffness results and failure load behavior, a second 3D FE model is generated considering only one interface (6th interface) at which a cohesive law is implemented. In our case, the 6th

interface is used, which is found to be the critical interface from the previous 2D finite element analysis. Besides, the 6th and 7th layers are modeled with two elements in the thickness direction since accurate stress and displacement values are desired at this local region. The remaining layers (the first 5 and last 11 layers from the inner radius) are considered as an equivalent laminate with the 3D equivalent laminate properties calculated according to Sun and Li [44]. This “global-local” method is developed by Sun and Liao [45] and used to model thick laminates away from the regions where accurate results are desired. The load-displacement curve for this case is shown in Figure 4-18 as the black line. The stiffness and failure load of the “global-local” approach agrees well with the experiments.

Crack tip speeds as a function of crack extensions for the center, edge, and 2D cracks are presented in Figure 4-19.

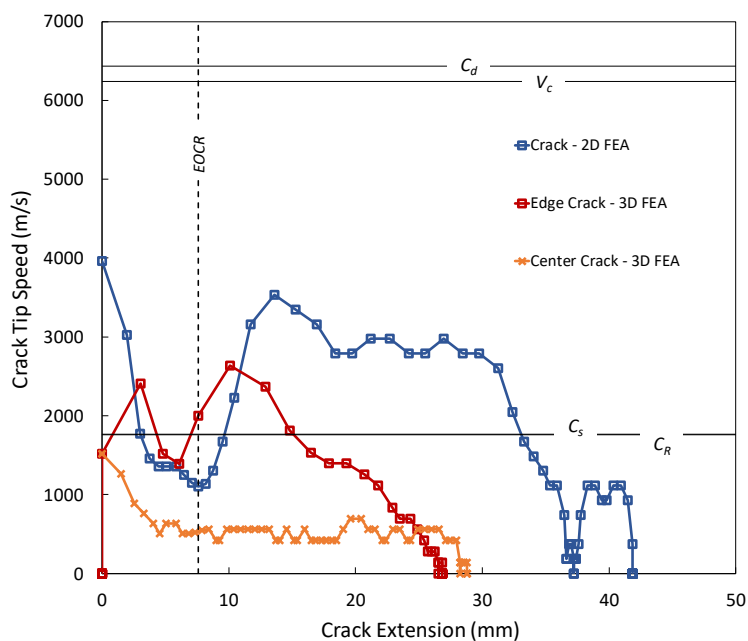


Figure 4-19. Crack tip speeds as a function of crack extensions for center, edge and 2D cracks.

In 2D FEA of the curved fabric laminate, the crack initiates intersonically and throughout all analysis it travels at intersonic speeds for 18 μ s. The 3D FEA results show that the center crack does not exceed the shear wave speed of the material during

all analysis. However, edge crack exceeds shear wave speed for only $5\mu\text{s}$ throughout the analysis.

The comparison of radial stresses at the mid-line of the center plane and free edge plane with the analytical solution [6] is given in Figure 4-20. Maximum radial stresses at the center and free edge plane are 52 MPa and 44 MPa, respectively. Both stresses are observed to occur at 37% of the thickness from the inner radius. The analytical solution calculated according to Ko and Jackson [6] predicts the maximum radial stress as 54 MPa which is also located at 37% of the thickness from the inner radius. The center plane and analytical solution show similar behavior in terms of radial stress distribution at the mid-line.

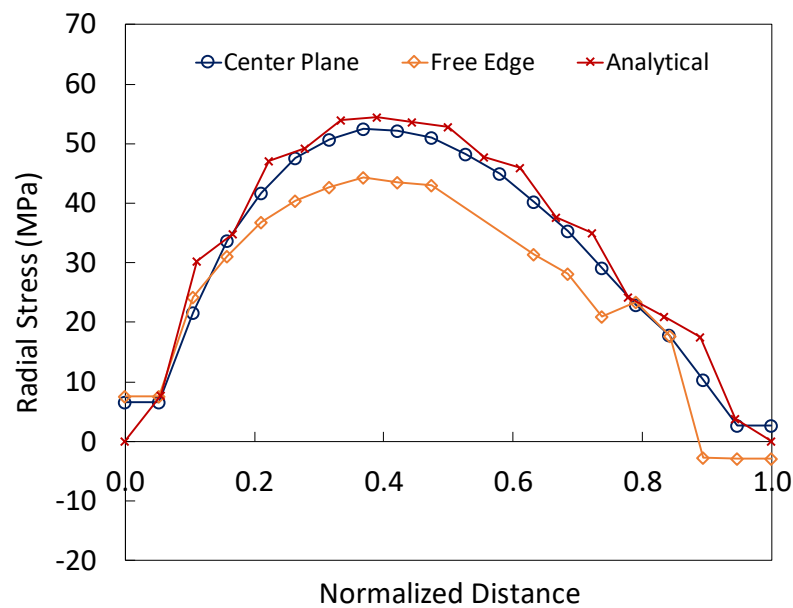


Figure 4-20. Radial stresses at the mid-line of center plane and free edge plane compared with the analytical solution.

Damage variables (SDEG) of the interface elements at the mid-line of the center plane and the free edge plane are presented in Figure 4-21 for eight μ s before the initiation of delamination. While the damage variable of the interface elements at the center plane attains a value of 0.714 at the 6th interface, the damage variable of the interface elements at the free edge plane attains a peak value of 0.89 at the 16th interface. This is due to the material mismatch between differently oriented layers at the free edge. The peak value of the damage variable is observed to attain at the center plane as the load increases. Finally, the delamination initiates at the center plane.

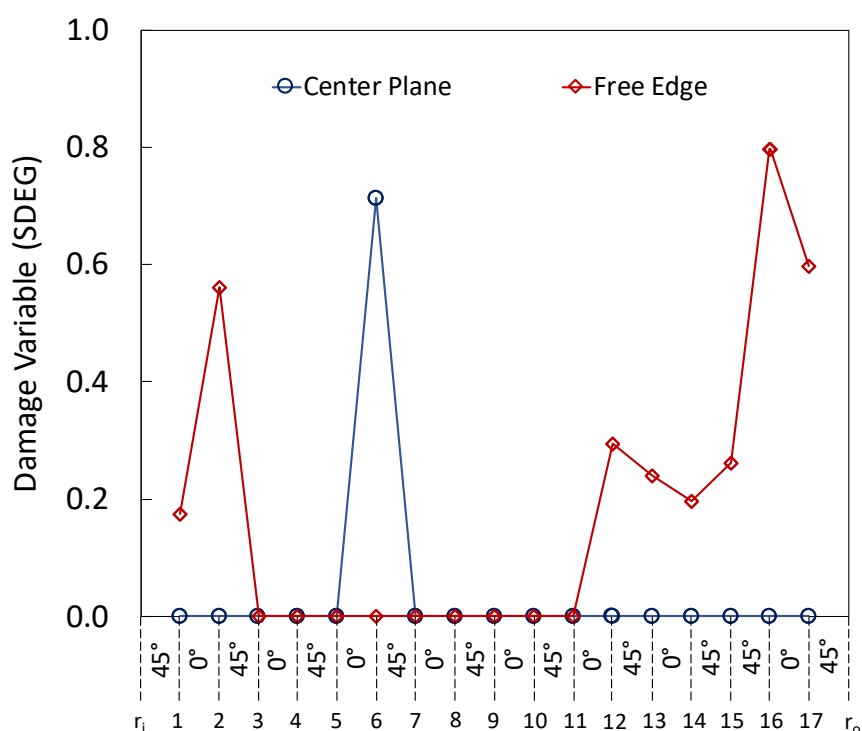


Figure 4-21. Damage variable (SDEG) of the interface elements at mid-line of center plane and free edge plane for 3D FEA of fabric laminate.

4.6. Conclusions

2D and 3D explicit finite element analyses of dynamic delamination in curved fabric CFRP laminate, [(45/0)₇,45/45/0/45], were carried out under moment/axial combined loading in conjunction with cohesive zone elements. The following conclusions are drawn as a result of the 2D and 3D FE analyses:

- Load-displacement curves of 2D FEA and 3D FEA of global/local approach show good correlations with experimental results [1].
- Delamination initiates at the center of the width of the fabric laminate. It is interesting to observe the delamination onset at center of the width instead of free-edge where the material mismatch exists between different layer orientations.
- For 2D FEA, the delamination initiates intersonically at the 7th interface which corresponds to 38% of the thickness from the inner radius. In the upper arm region of the fabric laminate, the delamination accelerates to a peak speed value of 3533 m/s in 2.8 μs.
- Shear Mach waves radiating from the crack front in the form of radial stresses are only observed in the 2D FEA of curved fabric laminate.
- For 3D FEA, the delamination initiates at the 6th interface with a speed value of 1700 m/s which is sub-Rayleigh. This critical interface corresponds to 33% of the thickness from inner radius.
- For 3D calculations, crack tip speeds are found to be different in the center and edge.
- Center crack never exceeds shear wave speed of the material throughout the analysis.
- The results of the 2D and 3D FEA show good correlation with the experimental results [1] in which the main delamination is also observed between 30% the 60% of the thickness from inner radius.

REFERENCES

- [1] Tasdemir, B. (2018). Fatigue and static behavior of curved composite laminates. MSc Thesis, Middle East Technical University.
- [2] Hu, Q., Zhang, Y., Mao, Y., Memon, H., Qiu, Y., Wei, Y., & Liu, W. (2019). A comparative study on interlaminar properties of L-shaped two-dimensional (2D) and three-dimensional (3D) woven composites. *Applied Composite Materials*, 26, 723 - 744.
- [3] Kedward, K. T., Wilson, R. S., & McLean, S. K. (1989). Flexure of simply curved composite shapes. *Composites*, 20 (6), 527 - 536.
- [4] González-Cantero, J. M., Graciani, E., López-Romano, B., París, F. (2018). Competing mechanisms in the unfolding failure in composite laminates. *Composites Science and Technology*, 156, 223-230.
- [5] Lekhnitskii, S. G. (1968). *Anisotropic plates*. NY: Gordon & Breach.
- [6] Ko, W. L., & Jackson, R. H. (1989). Multilayer theory for delamination analysis of a composite curved bar subjected to end forces and end moments. *Composite Structures*, 5, 173 - 198.
- [7] Chang, F., & Springer, G. S. (1986). The strength of fiber reinforced composite bends. *Journal of Composite Materials*, 20 (1), 30 - 45.
- [8] Sun, C. T., & Kelly, S. R. (1988). Failure in composite angle structures Part I: Initial failure. *Journal of Reinforced Plastics and Composites*, 7 (3), 220 - 232.
- [9] Sun, C. T., & Kelly, S. R. (1988). Failure in composite angle structures Part II: Onset of delamination. *Journal of Reinforced Plastics and Composites*, 7 (3), 233 - 244.
- [10] Rybicki, E. F., & Kanninen, M. F. (1977). A finite element calculation of stress intensity factors by a modified crack closure integral. *Engineering Fracture Mechanics*, 9 (4), 931 - 938.
- [11] Martin, R. H. (1992). Delamination failure in a unidirectional curved composite laminate. *Composite Materials Testing and Design*, 10, 365 - 383.
- [12] Martin, R. H., & Jackson, W. C. (1993). Damage prediction in cross-plyed curved composite laminates. *Composite materials: Fatigue and Fracture*, edited by Stinchcomb, W. and Ashbaugh, N. (West Conshohocken, PA: ASTM International), 4, 105 - 126.

- [13] Wisnom, M. R. (1996). 3-D finite element analysis of curved beams in bending. *Journal of Composite Materials*, 30 (11), 1178 - 1190.
- [14] Wimmer, G., Kitzmüller, W., Pinter, G., Wettemann, T., & Pettermann, H. E. (2009). Computational and experimental investigation of delamination in L-shaped laminated composite components. *Engineering Fracture Mechanics*, 76 (18), 2810 - 2820.
- [15] Li, S., Thouless, M. D., Waas, A. M., Schroeder, J. A., & Zavattieri, P. D. (2005). Use of a cohesive-zone model to analyze the fracture of a fiber-reinforced polymer-matrix composite. *Composites Science and Technology*, 65, 537 - 549.
- [16] Gözlüklü, B., & Coker, D. (2012). Modeling of the dynamic delamination of L - shaped unidirectional laminated composites. *Composite Structures*, 94 (4), 1430 - 1442.
- [17] Gözlüklü, B., Uyar, I., & Coker, D. (2015). Intersonic delamination in curved thick composite laminates under quasi - static loading. *Mechanics of Materials*, 80 (B), 163 - 182.
- [18] Coker, D., Rosakis, A. J., & Needleman, A. (2003). Dynamic crack growth along polymer composite - homalite interface. *Journal of the Mechanics and Physics of Solids*, 51 (3), 425 - 460.
- [19] Coker, D., Lykotrafitis, G., Needleman, A., & Rosakis, A. J. (2005). Frictional sliding modes along an interface between identical elastic plates subject to shear impact loading. *Journal of the Mechanics and Physics of Solids*, 53 (4), 884 - 922.
- [20] ABAQUS (2019). *Abaqus/Explicit: Advanced topics*. Dassault Systèmes, Providence, RI, USA.
- [21] ABAQUS (2019). *Getting started with Abaqus/CAE*. Dassault Systèmes, Providence, RI, USA.
- [22] Bathe, K. J. (2014). *Finite element procedures*. Englewood Cliffs, NJ: Prentice-Hall.
- [23] ABAQUS (2019). *Abaqus elements guide*. Dassault Systèmes, Providence, RI, USA.
- [24] Dugdale, D. S. (1960). Yielding of steel sheets containing slits. *Journal of the Mechanics and Physics of Solids*, 8 (2), 100 - 104.
- [25] Barenblatt, G. I. (1962). The mathematical theory of equilibrium cracks in brittle failure. *Advances in Applied Mechanics*, 7, 55 - 129.

- [26] Hillerborg, A., Modéer, M., & Petersson, P. E. (1976). Analysis of crack formation and crack growth in concrete by means of fracture and finite elements. *Cement and Concrete Research*, 6 (6), 773 - 781.
- [27] Needleman, A. (1999). An analysis of intersonic crack growth under shear loading. *Journal of Applied Mechanics*, 66 (4), 847 - 857.
- [28] Turon, A., Davila, C. G., Camanho, P. P., & Costa, J. (2007). An engineering solution for mesh size effects in the simulation of delamination using cohesive zone models. *Engineering Fracture Mechanics*, 74 (10), 1665 - 1682.
- [29] Camanho, P. P., & Dávila, C. G., (2002). Mixed-mode decohesion finite elements for the simulation of delamination in composite materials. NASA/TM-211737, 1 - 37.
- [30] Benzeggagh, M. L., & Kenane, M. (1996). Measurement of mixed-mode delamination fracture toughness of unidirectional glass/epoxy composites with mixed-mode bending apparatus. *Composites Science and Technology*, 56 (4), 439 - 449.
- [31] Raju, I. S., & O'Brien, T. K. (2008). Fracture mechanics concepts, stress fields, strain energy release rates, delamination initiation and growth criteria. *Delamination Behaviour of Composites*, 3 - 27.
- [32] Krueger, R. (2004). Virtual crack closure technique: History, approach and applications. ASME. *Applied Mechanics Reviews*, 57 (2), 109 - 143.
- [33] ABAQUS (2019). *Abaqus Analysis Guide*. Dassault Systèmes, Providence, RI, USA.
- [34] Lopes, C. S., Camanho, P. P., Gürdal, Z., Maimí, P., & González, E. V. (2009). Low-velocity impact damage on dispersed stacking sequence laminates. Part II: Numerical simulations. *Composites Science and Technology*, 69 (7 - 8), 937 - 947.
- [35] ASTM D6415/D6415M-06a. (2013). Standard test method for measuring the curved beam strength of a fiber-reinforced polymer-matrix composite. West Conshohocken, PA, United States: American Society for Testing and Materials.
- [36] ASTM D2344/D2344M-16. (2016). Standard test method for short-beam strength of polymer matrix composite materials. West Conshohocken, PA, United States: American Society for Testing and Materials.
- [37] Coker, D., & Rosakis, A. J. (2001). Experimental observations of intersonic crack growth in asymmetrically loaded unidirectional composite plates. *Philosophical Magazine A*, 81 (3), 571 - 595.

- [38] Huang, Y., Wang, W., Liu, C., & Rosakis, A. J. (1999). Analysis of intersonic crack growth in unidirectional fiber-reinforced composites. *Journal of the Mechanics and Physics of Solids*, 47 (9), 1893 - 1916.
- [39] Gözlüklü, B. (2014). Modelling of intersonic delamination in curved-thick composite laminates under quasi-static loading. PhD Thesis, Middle East Technical University.
- [40] Daniel, I. M., & Ishai, O. (2007). *Engineering mechanics of composite materials*. Delhi, India: Oxford University Press.
- [41] Marlett, K. (2011). Hexcel 8552S AS4 plain weave fabric prepreg 193 gsm & 38% RC qualification material property data report. National Institute for Aviation Research. Wichita State University, Wichita, KS.
- [42] Hexcel Corporation (2016). HexPly 8552 product data sheet.
- [43] Pinho, S. T., Iannucci, L., & Robinson, P. (2006). Formulation and implementation of decohesion elements in an explicit finite element code. *Composites Part A: Applied Science and Manufacturing* , 37 (5), 778 - 789.
- [44] Sun, C. T., & Li, S. (1988). Three-dimensional effective elastic constants for thick laminates. *Journal of Composite Materials*, 22(7), 629 - 639.
- [45] Sun, C. T., & Liao, W. C. (1989). *Analysis of thick laminates using effective moduli*. *Developments in the Science and Technology of Composite Materials*. Springer, Dordrecht.

APPENDICES

A. Beowolf Cluster Setup

A Beowolf cluster consists of 8 nodes is setup and used in the numerical calculations. Figure A.1 illustrates the schematic of the cluster setup. The head node, tata0, is connected to the internet and all other nodes are connected to Ethernet switch which provides communication between them. A KVM switch provides to monitor the display of the command window with only using one monitor, keyboard and mouse.

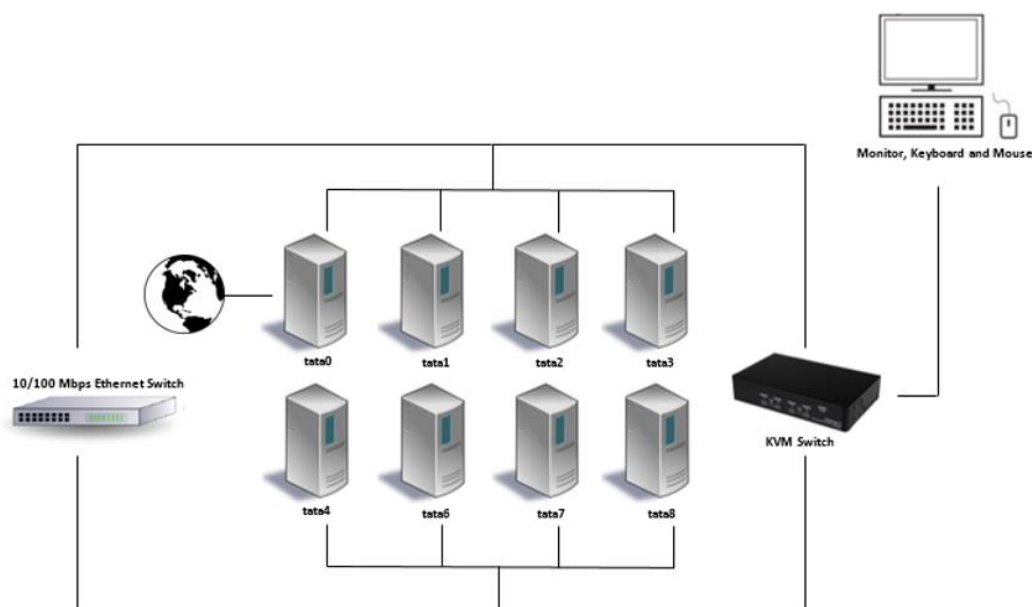


Figure A.1. Beowolf Cluster Setup Scheme.

The steps to setup a Beowolf cluster is as given below:

- Installation of the same operating system to all nodes.
- Introducing all nodes to each other with hostname lists and IP addresses
- Internet connection setup to head node (tata0)
- Installation of SSH server to all nodes

- Installation of NFS (Network File Sharing System) to all nodes
- Installation of MPI (Message Passing Interface) to all nodes
- Giving administrative privileges to all MPI users
- Installation of Fortran and other required compilers
- Installation of ABAQUS